9-2-2016

Autoignition Characteristics of Diesel Fuel and its Surrogates

Goutham Kukkadapu
University of Connecticut - Storrs, goutham.4238@gmail.com

Autoignition Characteristics of Diesel Fuel and its Surrogates

Goutham Kukkadapu, PHD

University of Connecticut, 2016

The design process for development of engines could be made faster and less expensive with the help of computations which help understanding the processes prevalent in internal combustion engines. Running engine simulations are challenging as they need to accurately capture the fluid dynamic and chemical kinetic processes that occur in an engine. A major challenge in simulating chemical kinetic processes is the complexity of the fuel chemistry: real fuels are complex mixtures whose composition determines their physical properties and reactivity. The behavior of these real fuels can be conveniently represented using simpler mixtures often called "surrogates mixtures" that match the key properties of the real fuels. Successful modeling of the ignition of real fuel first requires the formulation of an appropriate surrogate mixture whose compositions are carefully chosen in order to best emulate the combustion properties of the targeted real fuel. Then a comprehensive chemical kinetic model developed based on the surrogate fuel is used to simulate the combustion process of the real fuel. The work presented in the current dissertation intends to systematically study the surrogate modeling of diesel fuels. The study has been conducted to understand the ignition of surrogate fuel constituents and fully blended diesel fuels. Autoignition of tetralin, 1-methylnaphthalene, *iso*-cetane, and *n*-dodecane, the constituents of diesel surrogates, are investigated in the current dissertation. Besides, ignition of binary blends of the surrogate constituents has also been studied to investigate the effects of blending on ignition when neat components are blended to formulate a surrogate fuel. Furthermore, the ignition of two fully blended research grade diesel fuels has also been conducted inorder to provide high

Goutham Kukkadapu, PHD

University of Connecticut, 2016

quality ignition delay data for development and validation of chemical kinetic models of kinetic fuels.

Autoignition Characteristics of Diesel Fuel and its Surrogates

By

GOUTHAM KUKKADPU
B.Tech, Indian Institute of Technology, Madras, India
2009.

A Dissertation

Submitted in Partial Fulfillment of the

Requirements for the Degree of Doctor of Philosophy

at the

University of Connecticut.

2016

APPROVAL PAGE

Doctor of Philosophy Dissertation

Autoignition Characteristic of Diesel Fuel and its Surrogates

Presented By

Goutham Kukkadapu, B. Tech

Major Advisor_____

Chih-Jen Sung

Associate Advisor_____

Baki M. Cetegen

Associate Advisor_____

Tianfeng Lu

Associate Advisor_____

Bryan W. Weber

Associate Advisor_____

Xinyu Zhao

University of Connecticut

2016

Acknowledgements

This thesis summarizes my research over the past six years of my life and I couldn't have accomplished this without the help of many smart and generous people. Firstly, I would like to thank my adviser Prof. Jackie Sung for being an amazing mentor who supported and guided me throughout this journey. I would like to thank my thesis defense committee members Profs. Baki Cetegen, Tianfeng Lu, Xinyu Zhao and Bryan Weber. I would also like to thank Prof. Michael Renfro. I would like to thank my collaborators Dr. William J Pitz, Dr. Charles Westbrook, Dr. Marco Mehl and Dr. Mani Sarathy with whom I have had many interesting discussions. I would like to thank Mr. Jonathan VanScoyoc at Chevron Phillips and Dr. William J. Cannella at Chevron for providing us the samples of ULSD#2 and FD9A, respectively. I would like to thank Prof. Dhiman Chatterjee from Indian Institute of Technology Madras IITM, for his guidance during my undergraduate study.

I would like to thank the administrative staff at the department, Kelly Tyler, Laurie Hockla, Jacqueline Veronese, and Elizabeth Dracobly, who made sure all the paper work was taken care of and I get the pay checks and research supplies on time. Special thanks to the funding agencies, Combustion Energy Frontier Research Center, an Energy Frontier Research Center funded by the U.S. Department of Energy, National Science Foundation, and Lawrence Livermore National Laboratories, without their financial support this dissertation would not have been possible.

I would like to thank all the members of the Sung group, both past and present, Dr. Kamal Kumar, Dr. Apurba K. Das, Dr. Hui Xin, Dr. Yu Zhang, Dr. Bryan W. Weber, Dr. Kyle Brady, Dr. Kyle Nieyemer, Dr. Pradeep Singh, Dr. Xin Xue, Nick Curtis, Xiao Ren, Justin Bunnell and Mengyuan Wang.

I would like to thank many friends who were there for me the past few years including Ajay Babu, Deepak Balasubramaniam, Itti Bisht, Gopi Vinod Avvari, Sravanth Sanakavaram, Bikram Roychowdhury, Balakishore Nadella, Anwesha Chakraborthi, Manisha Mishra and Jyoti Nandi. I would like to thank my wife Laxmi for being there for me the past one year and especially for motivating me to finish my PhD and this thesis.

My biggest thanks go to my parents and my late grandfather. Ever since my childhood they made sure I got the best education. My father inspired me to dream big and without him I wouldn't be in one of the top universities in the world today. I would like to thank my brother Dr. Prithvi Kukkadapu who has been a great inspiration.

Contents:

Acknowledgements iv

Contents vi

List of Figures x

List of Tables xvi

CHAPTER 1 : INTRODUCTION 1

1.1 BACKGROUND 1

1.2 OBJECTIVES 4

1.3 STRUCTURE OF THE DISSERTATION 5

CHAPTER 2 : EXPERIMENTAL AND NUMERICAL SPECIFICATIONS 8

2.1 EXPERIMENTAL FACILITY 8

2.1.1 UCONN RCM 9

2.1.2 Mixing Chamber 11

2.1.3 Flow Control System 12

2.2 TEST PROCEDURE 12

2.2.1 Mixture Preparation 12

2.2.1 Operating Procedure 13

2.2.2 Data Processing 15

2.3 NUMERICAL SPECIFICATIONS 19

2.3.1 RCM Simulations 19

2.3.2 Reaction Path Analysis 22

2.3.3 Brute Force Sensitivity Analyses 22

CHAPTER 3 : TETRALIN 23

3.1 INTRODUCTION 23

3.2. EXPERIMENTAL SPECIFICATIONS 25

3.2.1 Test Conditions 25

3.2.2 Mixture Preparation 26

3.3 EXPERIMENTAL RESULTS 27

3.3.1 Pressure Measurements 27

3.3.2 Ignition Delay Measurements 28

3.3 COMPARISON OF IGNITION DELAYS OF TETRALIN AND N-BUTYLBENZENE 31

3.4. CHEMICAL KINETIC ANALYSES 34

3.4.1 Ignition Delay Simulations 34

3.4.2 Reaction Path Analysis 37

3.4.3 Brute Force Sensitivity Analyses 40

3.5 CONCLUSIONS 45

CHAPTER 4 : 1-METHYLNAPHTHALENE 47

4.1. INTRODUCTION 47

4.2. EXPERIMENTAL SPECIFICATIONS 49

4.2.1 Test Conditions 49

4.2.2 Mixture Preparation 50

4.3. EXPERIMENTAL RESULTS 50

4.4 SIMULATED RESULTS AND CHEMICAL KINETIC ANALYSES 54

4.4.1 Ignition Delay Simulations 54

4.4.2 Reaction Path Analysis 65

4.4.3 Brute Force Sensitivity Analyses 69

4.4.4 Possible Missing Reaction Paths 74
4.5. CONCLUSIONS 77
CHAPTER 5 : BINARY BLENDS 79
5.1. INTRODUCTION 79
5.2. EXPERIMENTAL SPECIFICATIONS 81
5.2.1 Test Mixtures 81
5.2.2 Test Conditions 82
5.2.3 Mixture Preparation 83
5.3. EXPERIMENTAL RESULTS 83
5.3.1 Experiments with Pure Components 83
5.3.2 Experiments with n-C12/1-MN Binary Blends 86
5.3.3 Experiments with i-C16/1-MN Binary Blends 89
5.4. IGNITION DELAY SIMULATIONS 92
5.5. CONCLUSIONS 98
CHAPTER 6 : ULSD#2 AND FD9A DIESEL BLENDS 100
6.1 INTRODUCTION 100
6.2 PROPERTIES AND COMPOSITIONS OF DIESEL BLENDS 103
6.3 EXPERIMENTAL SPECIFICATIONS 105
6.3.1 Estimation of Compressed Temperature (T_C) 105
6.3.2 Test Conditions 106
6.3.3 Vaporization Checks 107
6.4 EXPERIMENTAL RESULTS AND DISCUSSION 111
6.4.1 Ignition Characteristics of ULSD#2 and FD9A 111
6.4.2 Comparison of Ignition Delays of ULSD#2 and FD9A 117
6.4.3 Comparison of Current Total Ignition Delay Data and Literature Results 120

6.5 CONCLUSIONS 122

CHAPTER 7 : SUMMARY AND FUTURE DIRECTIONS 123

7.1 SUMMARY 123

7.2 FUTURE WORK 124

REFERENCES 126

List of Figures:

Figure 2.1 Schematic of the UCONN RCM Facility, picture taken from [12]..... 9

Figure 2.2 Schematic of the RCM, the end reaction chamber and the creviced piston head. Picture taken from [12]. 11

Figure 2.3 Plot showing the pressure history data obtained from each experimental run. 14

Figure 2.4 Plot showing the abridged raw and smoothed pressure traces. 15

Figure 2.5 Plot showing the definitions of first-stage ignition delay (τ_1) and total ignition delay (τ) used in the current study. Conditions: ULSD#2/air, ϕ=0.5, P_C=20 bar, and T_C=678 K. 18

Figure 2.6 Plot demonstrating the repeatability of the current ignition delay measurements. Conditions: Tetralin/air, ϕ=0.5, P_C=50 bar, and T_C=796 K. 19

Figure 2.7 Plot showing the (a) volume history and (b) pressure traces obtained from experiments and simulation. 21

Figure 3.1 Skeletal structure of tetralin. 23

Figure 3.2 Representative pressure traces at three of the experimental conditions from Table 3.1. It can be seen that no evidence of two-stage ignition is found in the pressure traces. 27

Figure 3.3: Pre-ignition heat release identified by comparison of pressure histories obtained from reactive and nonreactive experiments, for T_C=763 K and 802 K. The pressure trace for T_C=802 K is offset by +5 bar to clarify differences in the pressure traces. Conditions: ϕ=1.0 in air, Xtetralin=1.6%, and P_C=35 bar. 28

Figure 3.4 Arrhenius plots of ignition delays of tetralin/oxidizer mixtures at varying pressures and equivalence ratios. 29

Figure 3.5 Comparison of ignition delays of *n*-butylbenzene and tetralin. 32

Figure 3.6 Schematic of important reactions in tetralin and *n*-butylbenzene low-temperature ignition. Note that chain branching steps are possible from any carbon in the butyl chain for n-butylbenzene; for further discussion of the reaction pathways of *n*-butylbenzene, the interested reader is referred to the work of Husson et al. [35]. 33

Figure 3.7 Comparison of measured pressure traces and computed profiles using CONV and VPRO simulations. 34

Figure 3.8 Comparison of experimental and simulated ignition delays for the diluted experiments – tetralin/O_2/N_2 mixtures with X_{O2}=10.42%. 35

Figure 3.9 Arrhenius plots showing the complementary nature of ignition delays measured in this RCM study with the shock tube (ST) data taken from Wang et al. [25] at different pressures and equivalence ratios. All mixtures are tetralin/air. Computational results based on the CONV simulations are also plotted for comparison. 37

Figure 3.10 Integrated reaction path analysis up to 10% fuel conversion from an initial condition of 35 bar and 835 K for a ϕ=0.5 tetralin/air mixture in the CONV simulation. 38

Figure 3.11 Brute force sensitivity of the ignition delay for ϕ=0.5 tetralin/air mixtures at an initial pressure of 35 bar for three initial temperatures in the CONV simulations. 41

Figure 3.12 Brute force sensitivity of the ignition delay for ϕ=0.5 and ϕ=1.0 tetralin/air mixtures at an initial condition of 35 bar and 835 K in the CONV simulations. 44

Figure 4.1 Skeletal structure of 1-methylnaphthalene. 47

Figure 4.2 Plot showing the pressure traces at varying compressed pressures, compressed temperatures, and equivalence ratios. 51

Figure 4.3 Comparison of ignition delays of 1-MN/air mixtures at varying compressed pressures, compressed temperatures, and equivalence ratios, obtained from the current RCM experiments and the shock tube experiments of [47,48]. 53
Figure 4.4 Plot showing the effect of equivalence ratio on ignition delay. 54
Figure 4.5 Plot showing the different types of simulations conducted in the current study and their comparison with the experimental results. 56
Figure 4.6 Comparison of the ignition delays from experiments and simulations. Filled symbols: experiments. Broken lines: simulations using the model of Wang et al. [48]. Solid lines: simulations using the model of Narayanaswamy et al. [50]. 58
Figure 4.7 Plot showing the comparison of pressure traces from experiments and simulations. . 59
Figure 4.8 (a) Plot showing the evolution profiles of pressure and intermediate species predicted by the model of Wang et al. [48]. (b) Chemical structures of the intermediate species. Initial conditions are P_0=40 bar and T_0=900 K. 60
Figure 4.9 Reaction scheme showing the reactions channels leading to the formation of A1OC6H4Obis and A1OC6H4O in the model of Wang et al. [48]. "X" represents H, O, and OH. 60
Figure 4.10 Plot showing the performance of the model of Narayanaswamy et al. [50] at the conditions investigated by Wang et al. [48]. 64
Figure 4.11 Reaction path analysis conducted for equivalence ratio of ϕ=0.5 in air at 50% conversion of 1-MN starting at initial conditions of 40 bar and 870 K. The chemical formulae of the species are given in parentheses. "R" represents H, O, OH, and HO2. 65
Figure 4.12 Comparison of brute force sensitivity coefficients of selected reactions at varying equivalence ratios for initial conditions of 40 bar and 870 K. 71

Figure 4.13 Plot showing the effect of decreasing the rate of the reaction C9H6O + H = A1C2H3* + CO by a factor of two on pressure evolution. 71

Figure 4.14 Comparison of brute force sensitivity coefficients of selected reactions for stoichiometric 1-MN/air mixtures with initial pressure of 40 bar at varying initial temperatures. 72

Figure 4.15 Plot showing the rate comparison for the reaction of C6H6+O = C6H5O + H taken from Blanquart et al. [54] and Taatjes et al. [55]. 73

Figure 4.16 Important reactions of 1-MN + OH system. Reactions with broken arrows indicate the pathways which are missing in the model of Narayanaswamy et al. [50]. 75

Figure 4.17 Important reactions of 1-naphthylmethyl (A2CH2) + O_2 system taken from Oguchi and Murakami [52]. Reactions with broken arrows indicate the pathways which are missing in the model of Narayanaswamy et al. [50]. 77

Figure 5.1 Skeletal structure of constituents of the binary blends. 80

Figure 5.2 Comparison of ignition delays of (a) 1-MN, (b) *i*-C16, and (c) *n*-C8 and *n*-C12 from the current RCM experiments and the literature shock tube experiments [47,48,61,65,78]. 85

Figure 5.3 Plots showing (a) experimental pressure traces at compressed temperature of T_C=669±3 K, (b) total ignition delays, and (c) first stage ignition delays for *n*-C12/1-MN blends at varying blending ratios. 87

Figure 5.4 Plot showing the effect of % *n*-C12 in the *n*-C12/1-MN blends on total ignition delays at P_C=15 bar for two compressed temperatures of T_C~669 K and ~893 K. 88

Figure 5.5 Arrhenius plots of ignition delays of binary blends of *i*-C16/1-MN. The legends in the figure represent the amount of *i*-C16 in the binary blend. 90

Figure 5.6 Plot showing total ignition delay variation with % *i*-C16 in the *i*-C16/1-MN blend. . 91

Figure 5.7 Plot showing total ignition delay variations with % *n*-C12 and % *i*-C16 in the blends, conducted at P_C=15 bar and T_C=893±10 K. 91

Figure 5.8 Comparison of total ignition delays of two blends with a similar DCN value but different blend compositions. 92

Figure 5.9 Plot showing the comparison of pressure traces from experiments and simulations for (a) 10/90 *n*-C12/1-MN blend and (b) neat 1-MN. 93

Figure 5.10 Comparisons of total ignition delays of (a) neat *n*-C12, (b) neat 1-MN, and (c) *n*-C12/1-MN blends over a range of T_C, (d) total ignition delays of *n*-C12/1-MN blends at T_C~669 K, and (e) first stage ignition delays of *n*-C12/1-MN blends from experiments and simulations using the model of Narayanaswamy et al. [80]..... 95

Figure 5.11 Comparison of ignition delays from experiments and simulations for neat *i*-C16 at P_C=15 bar. Simulations were conducted using the model of Oehlschlaeger et al. [61]. 98

Figure 6.1 Plot showing the measured pressures in the mixing chamber after liquid fuel injection. The pressure expected from complete fuel vaporization calculated using the ideal gas law is also shown as a reference. 108

Figure 6.2 Comparison of measured pressure traces of ignition of FACE A gasoline and FD9A diesel at similar compressed conditions of P_C = 20 bar and $T_C \sim$ 700 K. 110

Figure 6.3 Plots showing the pressures traces of ULSD#2 and FD9A for ϕ = 0.5 in air at varying compressed temperatures and pressures..... 112

Figure 6.4 Arrhenius plots of ignition delays (τ_1 and τ) of ϕ = 0.5 diesel/air mixtures at P_C = 10 and 20 bar: (a) ULSD#2 and (b) FD9A. 113

Figure 6.5 Arrhenius plots of ignition delays (τ_1 and τ) of ULSD#2 and FD9A at varying compressed pressures and equivalence ratios (i.e. oxygen mole percentages). The fuel mole percentage is kept constant at 0.514%. 115

Figure 6.6 Compression of pressure traces at P_C = 20 bar and T_C = 678 K with ϕ = 0.5 and 1.02 by varying oxygen mole percentage: (a) ULSD#2 and (b) FD9A. The fuel mole percentage is kept constant at 0.514%. 116

Figure 6.7 Comparison of ignition delays (τ_1 and τ) of ULSD#2 and FD9A at varying compressed pressures and equivalence ratios (i.e., oxygen mole percentages). The fuel mole percentage is kept constant at 0.514%. 119

Figure 6.8 Comparison of total ignition delays of ULSD#2, FD9A, and literature diesel blends at (a) P_C = 10 bar and ϕ = 0.5 and (b) P_C = 20 bar and ϕ = 0.5. 121

List of Tables:

Table 3.1: Tetralin test conditions 26

Table 4.1: 1-MN experimental test conditions 50

Table 5.1: Compositions of test mixtures and DCN values of *n*-C12/1-MN blends. 82

Table 5.2: Compositions of test mixtures and DCN values of *i*-C16/1-MN blends. 82

Table 6.1: List of literature studies on autoignition of diesel blends**.** 101

Table 6.2: Comparison of properties and compositions of the diesel blends used in the current study and in Gowdagiri et al.[91]. 104

Table 6.3: Test conditions investigated in the study on diesel fuels. 107

Chapter 1 : Introduction

1.1 Background

As fuel costs rise and price increases percolate to other commodities, we are challenged with the pressing issues of efficient usage of the available fossil fuel reserves and the transition to non-petroleum based, carbon-neutral, bio-derived fuels. The ground transportation sector is the largest consumer of liquid petroleum fuels and although the transition to biofuels has been initiated, it might take decades to complete. Therefore, for the foreseeable future, fossil fuels will continue to be the prime mover of ground transportation. Furthermore, the EPA and Congress have instituted mandates to reduce our nation's CO_2 emissions by 80% by 2050 and petroleum usage by 25% by 2020. With this in mind, we need to develop next-generation combustion technology with a focus on higher efficiency, reduced emissions, and flexibility for use with alternative, non-petroleum-based fuels.

Current compression-ignition (CI) engine (i.e. diesel engine) technology is well suited for heavy-duty vehicle applications and is capable of delivering fuel economy considerably higher than spark-ignition (SI) engines. Key developments in combustion and emission controls, plus low-sulfur fuel, have enabled manufacturers to achieve the necessary emissions levels and introduce additional diesel-powered vehicles to the U.S. market. Furthermore, heavy-duty diesel engines are the primary engine for commercial vehicles because of their high efficiency and outstanding durability. However, the implementation of increasingly stringent heavy-duty engine emission standards over the last decade has held efficiency gains to a modest level.

As designers attempt to increase the fuel efficiency of engines and to reduce pollutant emissions, the in-cylinder thermodynamic conditions approach engines' operating limits (e.g., high pressure, lean fuel-oxidizer mixture, low temperature). For instance, one novel combustion regime is known as low-temperature combustion (LTC), where operating with extremely lean fuel-air or highly diluted mixtures and under high compression ratios results in high efficiency and low emissions. LTC conditions typically include temperatures between 650–1100 K, pressures between 10 and 60 bar, and equivalence ratios

between ϕ=0.3–2. Due to the dilute mixtures used in an LTC engine, the combustion temperature ranges from 1500–2000 K, about 500 K lower than traditional SI or CI engines. Several new types of advanced engines have been developed to take advantage of LTC. Among these are homogeneous charge compression ignition (HCCI), premixed charge compression ignition (PCCI), and reactivity controlled compressed ignition (RCCI). HCCI and PCCI in particular have been demonstrated to operate at efficiencies comparable to that of conventional diesel engines while substantially reducing emissions [cf. 1,2].

HCCI engines typically operate at fuel-lean conditions with homogeneous mixtures of fuel and oxidizer. Furthermore, exhaust gas recirculation (EGR) is used to control ignition phasing. The homogeneous fuel-lean conditions prevailing in the engine prevent formation of soot and the low post-ignition temperatures suppress formation of NO_X. In PCCI engines, fuel is injected into the engine cylinder early in the compression stroke, allowing the fuel to premix with the air in the cylinder. This premixing reduces the formation of soot as compared to traditional diesel engines. Low post-ignition temperatures are attained by using significant levels of EGR and further inhibit soot and NO_X formation. However, controlling the ignition phasing in HCCI and PCCI engines may be difficult because the ignition timing is entirely reliant on chemical kinetics. In traditional CI and SI engines, ignition timing is controlled by fuel injection and spark timing respectively, physical processes that can be more easily controlled than chemical kinetics [e.g., 3-5]. For this reason, alternate LTC engine approaches have been developed, including RCCI.

RCCI engines rely on the use of two fuels with different reactivity. First, the low reactivity fuel is injected during the compression stroke to create a premixed charge in the cylinder. Subsequently, the higher reactivity fuel is injected before the ignition of lower reactivity fuel. The higher reactivity fuel ignites shortly after injection, so that the physical process of its injection can help control the ignition timing. Meanwhile, the lower reactivity fuel present in the cylinder for much of the compression stroke allows operation at higher compression ratios (i.e. higher efficiencies) than could be achieved if only the high reactivity fuel were used. Therefore, chemical kinetics, and in particular the kinetic interaction of the two

fuels, plays an important role in the efficiency and emissions of RCCI engines. RCCI engines have the potential to operate at efficiencies higher than conventional engines, with an estimated increase in efficiency of about 20% over current on-road engines [6]. For instance, current heavy-duty diesel engines typically have efficiencies in the 42–43% range but heavy-duty vehicles using LTC may reach efficiencies as high as 55% [6], a 30% increase.

While the potential benefits of LTC combustion technologies are great, the current engine designs have several practical development issues that must be solved before they can be implemented on a large scale. As mentioned previously, controlling ignition phasing and extending the operating limits while maintaining high efficiencies and low pollutant emissions [6] are some of the important developmental issues associated with LTC technologies. Although substantial effort has been expended towards the development of practical LTC engines, further experimental and computational research work is still needed. Since predictive simulation plays an important role in reducing the design cycle, predictive capability for the fuel chemistry combined with computational fluid dynamics (CFD) simulations are expected to serve an important role towards the development of LTC engines. As the need for accurate chemical kinetic models has been recognized and grown, an accurate description of the finite-rate chemistry of the fuel oxidation is necessary.

One of the most commonly suggested fuels for use in advanced LTC engines is diesel fuel, due to its ubiquity at fueling stations and relatively high reactivity compared to gasoline. To utilize diesel-fueled LTC engines to the fullest, accurate modeling of chemical kinetics that control ignition is imperative. Unfortunately chemical kinetic models of diesel fuels are not well developed, primarily due to the complex chemical composition of the fuel. Diesel is made up of several hundred hydrocarbons from different classes, including paraffins, olefins, and aromatics. Developing a chemical kinetic model to account for every hydrocarbon species present in diesel is unrealizable. Instead, surrogate fuels made of mixtures of a limited number of neat components are used to represent real fuel. These surrogate fuels must reproduce the

physical and chemical properties of the real fuel, while simultaneously being amenable to modeling. Several such surrogate mixtures have been developed, for example, for gasoline [7] and jet fuels [8].

Due to the desire to use diesel fuel in advanced engines, and the difficulty inherent in modeling real diesel fuel, the development of a diesel fuel surrogate and its kinetic model holds the key to the development of advanced LTC engines. Unfortunately, the kinetic models for many typical diesel fuel surrogate components are still not well developed, as pointed out by Krishnasamy et al. [9] and Farrerll et al. [10]. If models for the individual components can be developed and validated, they can be integrated to form a model for the complete diesel surrogate mixture. Thus, it is necessary to develop a comprehensive database of high-fidelity experimental results at engine relevant conditions for diesel fuel and its surrogates.

1.2 Objectives

The key tasks of the current dissertation is obtaining extensive experimental data using rapid compression machines for autoignition characteristics of lean to rich (ϕ=0.5–1.5) fuel+oxidizer mixtures at engine relevant conditions, including elevated pressures (10–50 bar) and low-to-intermediate temperatures (600–1000 K), for the following fuels.

Neat Components

- *n*-Alkane: *n*-dodecane
- *iso*-Alkane: *iso*-cetane
- Aromatic: 1-methylnaphthalene
- Naphtheno aromatic: tetralin

Binary blends

- *n*-Alkane/Aromatic: *n*-dodecane/1-methylnaphthalene
- *iso*-Alkane / Aromatic: *iso*-cetane/1-methylnaphthalene

Research-Grade Diesel

- Certified ULSD #2 supplied by Chevron Phillips
- Certified FACE 9A supplied by Chevron Phillips

1.3 Structure of the Dissertation

The work presented in the current dissertation has either been published or been submitted for publication in archival literature. Chapter 2 covers the details about the experimental and numerical procedures conducted in the dissertation studies. Chapter 3 covers the study on autoignition of tetralin and has been published in Fuel. Chapter 4 covers the autoignition of 1-methylnaphthalene and has been submitted for consideration for publication in Energy and Fuels. Chapter 5 covers the autoignition of binary blends of *n*-dodecane/1-methylnaphthalene and *iso*-cetane/1-methylnaphthalene and will be submitted for consideration for publication in Combustion and Flame. Chapter 6 covers autoignition of two certified fully blended diesel fuels and has been published in Combustion and Flame.

The work conducted during my studies at UCONN has contributed the following published or under review journal communications.

1. G. Kukkadapu, C. J. Sung, "*Autoignition study of 1-methylnaphthalene in a rapid compression machine"*, Energy and Fuels, in review.
2. G. Kukkadapu, C. J. Sung, "*Autoignition of binary blends of n-dodecane/1-methylnaphthalene and iso-cetane/1-methylnaphthalene"*, Combustion and Flame, To be submitted.
3. N. Atef, G. Kukkadapu, S. Y. Mohamed, M. A. Rashidi, C. Banyon, M. Mehl, A. Heufer, E. F. Nasir, A. Alfazazi, A. K. Das, C. K. Westbrook, W. J. Pitz, A. Farooq, C.J. Sung, H. J.

Curran, S. M. Sarathy, "*Comprehensive chemical kinetic modeling of iso-octane combustion with improved thermochemistry and kinetics",* Combust. Flame, To be submitted.

4. G. Kukkadapu, C. J. Sung, "*Autoignition study of ULSD#2 and FD9A diesel blends"*, Combustion and Flame, 166 (2016), pp. 45-54.
5. S. M. Sarathy, G. Kukkadapu, M. Mehl, T. Javed, A. Ahmed, N. Naser, A. Tekawade, G. Kosiba, M. AlAbbad, E. Singh, S. Park, M.A. Rashidi, S.H. Chung, W.L. Roberts, M.A. Oehlschlaeger, C.-J. Sung, A. Farooq, "*Compositional effects on the ignition of FACE gasolines"*, Combust. Flame, 169 (2016), pp. 171–193.
6. C.-W. Zhou, Y. Li, E. O'Connor, K.P. Somers, S. Thion, C. Keesee, O. Mathieu, E.L. Petersen, T.A. DeVerter, M.A. Oehlschlaeger, G. Kukkadapu, C.-J. Sung, M. Alrefae, F. Khaled, A. Farooq, P. Dirrenberger, P.-A. Glaude, F. Battin-Leclerc, J. Santner, Y. Ju, T. Held, F.M. Haas, F.L. Dryer, H.J. Curran, "*A comprehensive experimental and modeling study of isobutene oxidation"*, Combust. Flame, 167 (2016), pp. 353-379.
7. G. Kukkadapu, B. W. Weber, C. J. Sung, "*Autoignition study of tetralin in a rapid compression machine at elevated pressures and low-to-intermediate temperatures"*, Fuel, 159 (2015), 436-445.
8. G. Kukkadapu, K. Kumar, C. J. Sung, M. Mehl, W. J. Pitz, "*Autoignition of gasoline surrogates at low temperature combustion conditions"*, Combust Flame, 162 (2015), pp. 2272-2285.
9. S. M. Sarathy, G. Kukkadapu, M. Mehl, W. Wang, T. Javed, S. Park, M. A. Oehlschlaeger, A. Farooq, W. J. Pitz, C. J. Sung, *"Ignition of alkane–rich FACE gasoline fuels and their surrogate mixtures"*, Proci. Combust. Inst., 35 (2015), pp. 249–257.

10. G. Kukkadapu, K. Kumar, C. J. Sung, M. Mehl, W. J. Pitz, "*Autoignition of gasoline and its surrogates in a rapid compression machine",* Proci. Combust. Inst., 34 (2013), pp.345-352.
11. G. Kukkadapu, K. Kumar, C. J. Sung, M. Mehl, W. J. Pitz, "*Experimental and surrogate modeling study of gasoline ignition in a rapid compression machine"*, Combust. Flame, 159 (2012), pp. 3066-3078.

Chapter 2 : Experimental and Numerical Specifications

Specifications of the experimental and numerical procedures used in the studies presented in this dissertation are described in this chapter. The experimental specifications describe the experimental facility and operating procedures while the numerical procedures describe the different types of numerical analyses conducted.

2.1 Experimental Facility

Rapid compression machines are used to compress gas mixtures to elevated pressures and temperatures using a fast moving piston which is brought to rest towards the end of compression. Post compression, the piston is held stationary thus providing a constant volume reactor. RCM's are typically designed to reduce bulk fluid motion and thermal in-homogeneities, thereby providing an ideal platform for studying chemical kinetics [11] and ignition characteristics of a fuels. The schematic of the RCM facility at UCONN can be seen in the Fig. 2.1. The major components of the facility include an RCM, a mixing chamber and a flow control/supply system. This chapter shall cover the details of the aforementioned components of the RCM facility and the specifications of the methods used to model the data acquired from RCM.

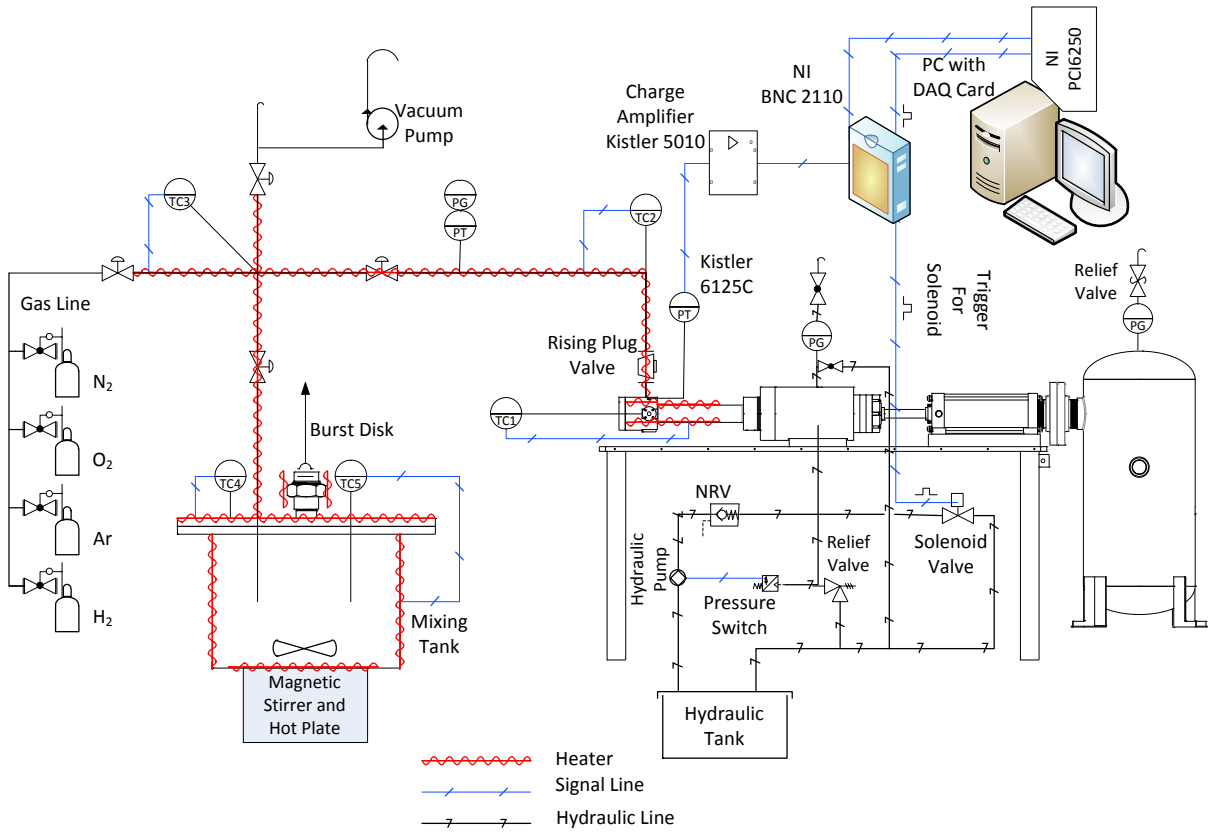

Figure 2.1 Schematic of the UCONN RCM Facility, picture taken from [12].

2.1.1 UCONN RCM

Figure 2.2 shows the schematic of the RCM used in the current studies. The main components of the RCM are reaction chamber, piston assembly, hydraulic chamber, pneumatic chamber, and high pressure gas tank. The piston assembly consists of three pistons, one each in the pneumatic, hydraulic, and reaction chambers, which are connected rigidly. One end of the piston in reaction chamber is connected to the hydraulic piston while the other end is connected to a creviced piston. The test gases are compressed by the creviced piston which is driven pneumatically and the piston assembly is brought to rest towards the end of the compression using a hydraulic-pin groove

mechanism. The compression time is around 30-45 ms depending on the operating conditions. The creviced piston used in the current facility has been designed to reduce the formation of the roll-up vortex and improve the homogeneity of the mixture at the compressed condition [13,14]. The UCONN RCM is versatile in its design offering optical accessibility, an ability to conduct rapid gas sampling measurements and a wide range of geometric compression ratios. The optical accessibility is enabled by use of calcium Floride (CAF_2) window plugs which can be fitted to the reaction chamber. Gas sampling experiments can be conducted using the specially designed end plug inconjuction with a gas sampling apparatus. The geometric compression ratio can be varied by changing either the stroke length or the clearance length at the end of compression. The geometric compression ratio (CR) can be estimated as

$$CR = 1 + \frac{Stroke\ length}{Clearance\ length} \qquad (eqn.2.1)$$

The stroke length in the current design can be varied between 7 and 10 inches in increments of 0.25 inches while the clearance length can be varied between 14 and 56 mm in increments of 1 mm. By changing the clearance length and stoke length the operating geometric compression ratio can be varied from 4 to 25. The change in compression ratio helps in scanning across a wide range of compressed temperatures. In addition to scanning the compressed temperature, the compressed pressure can also be varied between 7 and 70 bar at a fixed compression ratio by changing the intake pressure. The intake pressure is measured using a static pressure transducer obtained from OMEGA Engineering Inc. The wide range of compressed pressures and temperatures attainable in the current design makes it viable to study fuels with wide range of ignition propensities. The primary data obtained from the RCM experiments is the dynamic pressure in the reaction cylinder measured using a Kistler 6125 C transducer inconjunction with a Kistler 501B charge amplifier.

The compressed temperature and ignition delay are the kinetic information needed for understanding the oxidation chemistry and validation of chemical kinetic models are deduced from pressure history. The pressure from the reaction chamber is sampled for 2 seconds and at a sampling rate of 50 kHz. Further details of the current RCM design can be found [12].

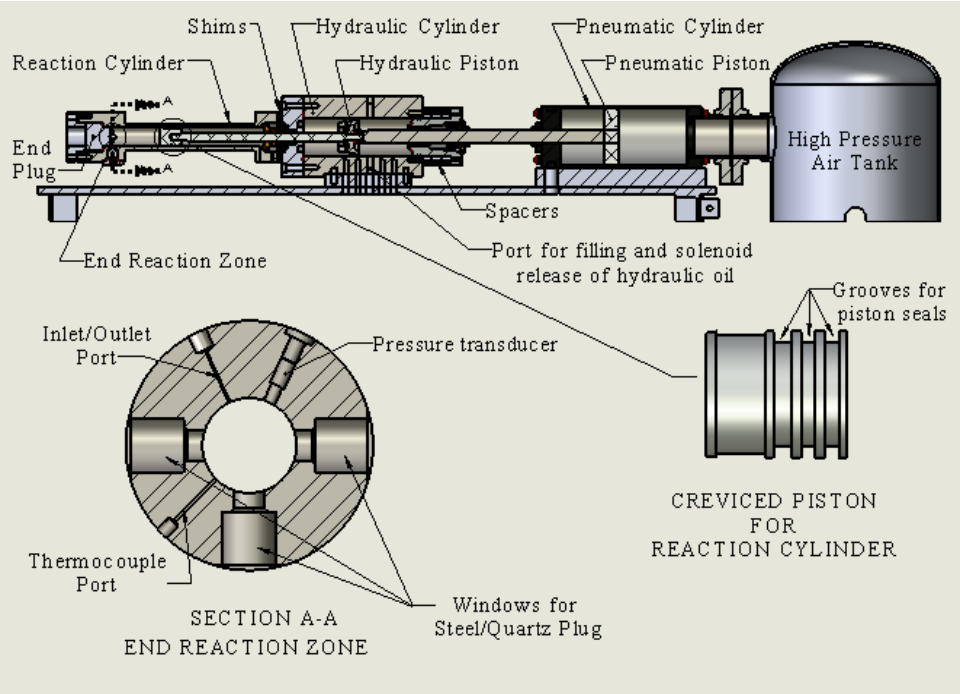

Figure 2.2 Schematic of the RCM, the end reaction chamber and the creviced piston head. Picture taken from [12].

2.1.2 Mixing Chamber

The mixing chamber show in Fig. 2.1 is used to prepare homogenous fuel+oxidizer mixtures. The mixing chamber used in the facility is a 17.47 lit stainless steel tank equipped with heating tapes, magnetic stirrer and pressure relief disc. The heating tapes are used to pre-heat the mixtures to the desired intake temperature while the magnetic stirrer placed at the bottom of the tank aids in proper

mixing. The pressure relief disc obtained from LaMOT® acts as a safety measure against accidental overpressure within the mixing tank. The pressure relief discs are rated to ~ 4.83 bar at temperature of 200 ^{o}C.

2.1.3 Flow Control System

The flow control system includes a vacuum pump and intake manifolds. The intake pressure in the whole RCM facility can be reduced to low pressures (< 2 Torr) using the vacuum pump. The intake manifolds are made up of Swagelok® fittings that are used to connect the RCM and the mixing chamber. The intake pressures for an experimental run can be controlled to about ±0.1 Torr using the vacuum pump and the intake manifolds. Furthermore, the intake manifolds are wrapped with heaters. The intake system, the mixing chamber and the RCM are always heated to identical pre-heat temperatures which can go upto 420 K (147^{o}C).

2.2 Test Procedure

This section provides details about the test protocol which involves preparation of homogenous test mixtures, operating the RCM to acquire data and data processing.

2.2.1 Mixture Preparation

The homogenous fuel/oxidizer mixtures are prepared in the mixing chamber, prior to which the pressure in the mixing chamber is brought down to a pressure below 5 Torr using the vacuum pump. The constituents of the fuel+oxidizer mixtures are filled into the chamber at room temperature. In all the studies reported here, the mixing chamber was filled with fuel, followed by the oxidizer gases. The fuels investigated in the current study are all in the liquid phase at room temperature and are injected directly into the mixing chamber using hypodermic glass syringes. The mass of the fuel injected into the chamber is measured using a mass balance which has a least count of 0.01 gm. The mass of fuel injected into the mixing chamber is determined from the

mixture composition and the pressure of the of test mixture. The oxidizer gases are then filled into the mixing chamber after injection of the liquid fuel. The oxidizer gases used in the current study are mixtures of oxygen and nitrogen in varying proportions. Ultra high purity (>99.99 %) grade oxygen and nitrogen obtained from Airgas® were used in the current experiments. Oxidizer mixtures are prepared by filling oxygen and nitrogen into the mixing chamber on a barometric measure. Once the mixing chamber is filled with fuel and oxidizer, the heaters and the magnetic stirrer are activated. The mixing chamber and the whole RCM facility is heated to desired pre-heat temperatures for about 4 hours before the start of experiments to attain homogeneity. This mixture preparation procedure has earlier been demonstrated to be adequate without fuel condensation [12,15,16]

2.2.1 Operating Procedure

At the beginning of each experimental run, the piston is retracted to bottom dead center by filling the front of the pneumatic chamber with high pressure air. At the fully retracted position the piston seats at the rear end of the hydraulic chamber and engages a seal. The piston is acted upon by the pressures in the pneumatic chamber and the driving tank. The pneumatic chamber is filled to pressures higher than the driving tank pressure to prevent the motion of the piston assembly. After locking the piston at bottom dead center, the hydraulic chamber is filled with oil to a pressure of 800 psi using a hydraulic pump which can be seen in Fig. 2.1. At this instant, the hydraulic oil and the air in the pneumatic chamber both push the piston assembly rearwards against the high pressure air in the driving tank. The air in the driving tank is generally at a pressure (<150 psi) lower than the pressure in the hydraulic chamber which makes pressurizing the pneumatic chamber redundant and thus the pneumatic chamber is depressurized to atmospheric conditions. Now the position of the piston is locked and the piston is acted upon by counter acting forces exerted by pressures in

the hydraulic chamber and the air in the driving tank. The reaction chamber is now filled with test gases drawn from the mixture chamber to the desired intake pressure condition. After filling and sealing the reaction chamber, the pressure in the hydraulic chamber is released suddenly using a solenoid valve. The pressure differential across the piston assembly accelerates the piston resulting in a rapid compression event. The operation of the solenoid value is controlled by a trigger sent from LabView® which also initiates the data acquisition.

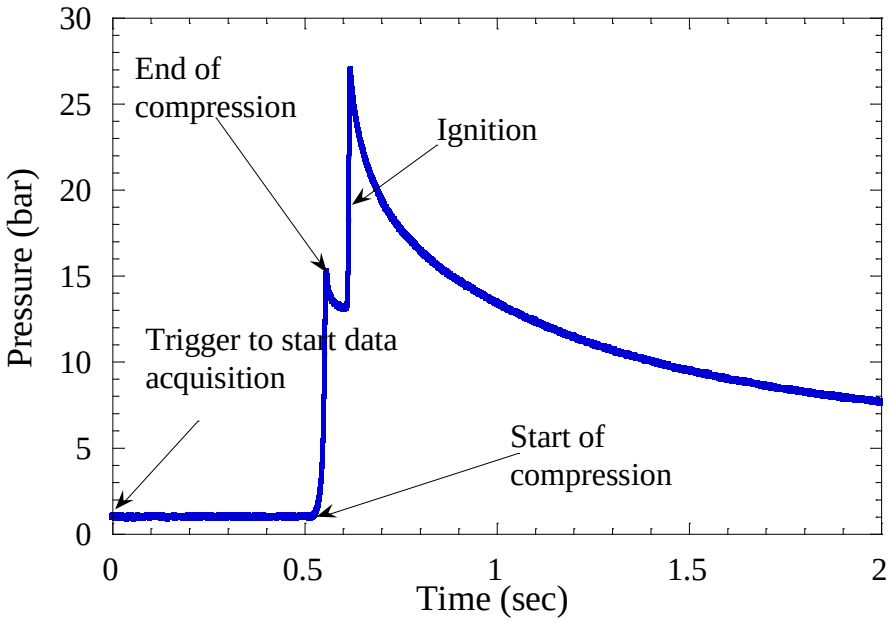

Figure 2.3 Plot showing the pressure history data obtained from each experimental run.

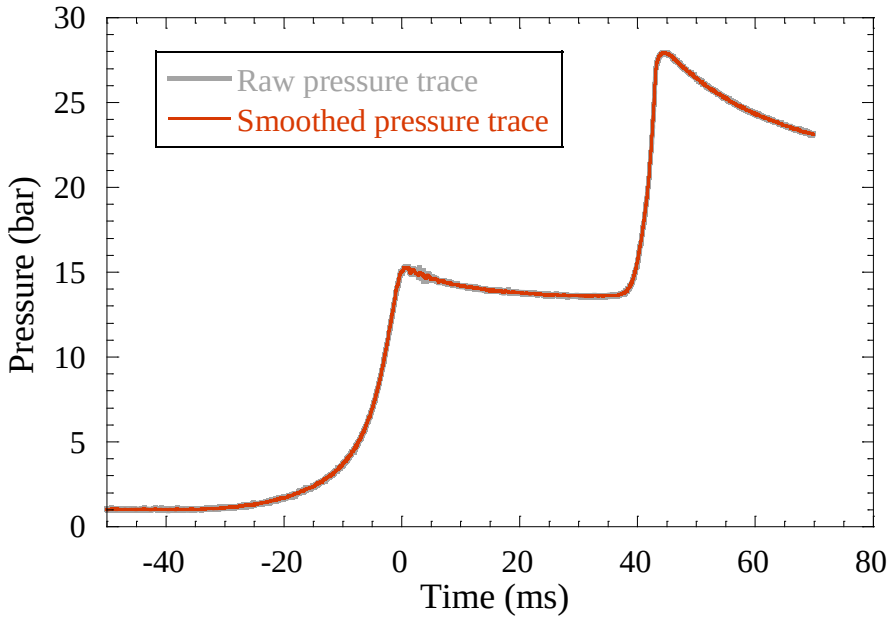

Figure 2.4 Plot showing the abridged raw and smoothed pressure traces.

2.2.2 Data Processing

Figure 2.3 shows an example of the raw pressure data obtained from RCM experiments. The time t=0 in Fig. 2.3 corresponds to the instant at which the trigger from LabView® is generated and data acquisition is initiated. A delay of about ~ 0.5 sec is always observed between start of data acquisition and activation of the solenoid valve in all the current RCM experiments. The trigger sent from LabView® activates the solenoid valve which reduces the pressure in the hydraulic chamber and results in start of compression as indicated by the change in the pressure in the reaction cylinder. The increase in pressure in the reaction chamber continues till the end of compression which is indicated by the first local maxima around 0.55 s. Post compression, the pressure in the cylinder drops due to heat transfer between the hot compressed gas and the cold boundary walls of the machine. The drop in pressure continues for a certain duration (called the chemical induction phase) and a sudden rise in pressure is observed due to onset of ignition. The

pressure in the chamber post ignition drops down as heat is transferred from the hot combustion products to the chamber walls. The pressure data of importance from the experiments is from start of compression to the ignition event which is extracted from the pressure history. Figure 2.4 shows the abridged pressure history extracted from the pressure history shown in Fig. 2.3. The abridged pressure history is used as the representative of the pressure trace. For the abridged traces, the time axis is off-set to represent the end of compression at t=0. The abridged pressure history is further smoothed using a moving average over 11 sampling points. The comparison of the raw and smoothed pressure traces is also shown in Fig 2.4. The smoothed pressure trace is used to determine the compressed pressure (P_C), compressed temperature (T_C), and ignition delays using the methods discussed in the following sections.

2.2.2.1 Compressed Temperature

The temperature of the reactant gases is seldom measured in RCM experiments. The direct measurement of temperature of the core gas using intrusive methods such as thermocouples could affect the homogeneity of the core and hence is not usually conducted. In addition, the use of thermocouples is also limited by characteristic time constants of the thermocouples. Non-intrusive absorption techniques may be used to measure temperature but the high pressure conditions prevalent in the reaction cylinder limit their applicability. For these reasons, the temperature of the reactive gases is estimated using "adiabatic core" hypothesis [17]. Recent work [18,19] from our lab has demonstrated that the compressed temperature estimated using this hypothesis was found to closely match with temperatures measured using IR absorption technique. The differences in compressed temperature obtained from IR measurements and from the hypothesis were found to be within ±5 K. According to this hypothesis, the core of the reactant gas in compressed

adiabatically and the temperature of the reactant gases at end of compression (T_C) can be deduced from

$$\int_{T_0}^{T_c} \frac{\gamma}{\gamma - 1} \frac{dT}{T} = \ln\left(\frac{P_c}{P_0}\right),$$

where P_C, P_0, and T_0 are measured values and γ is the ratio of specific heats, which is temperature dependent. As such, estimation of compressed temperature requires prior knowledge of the thermodynamic properties of the test fuel+oxidizer mixture.

2.2.2.2 Definition of Ignition Delays

The ignition delays reported in the current works are measured relative to the end of compression (EOC) which is set at t=0 ms. The ignition events and thereby the ignition delays are identified using the local maxima of the time derivative of the pressure. The definition used in the current study is best illustrated by the Fig. 2.5. The first stage (when observed) and total ignition delays are deduced using the definition shown in Fig. 2.5.

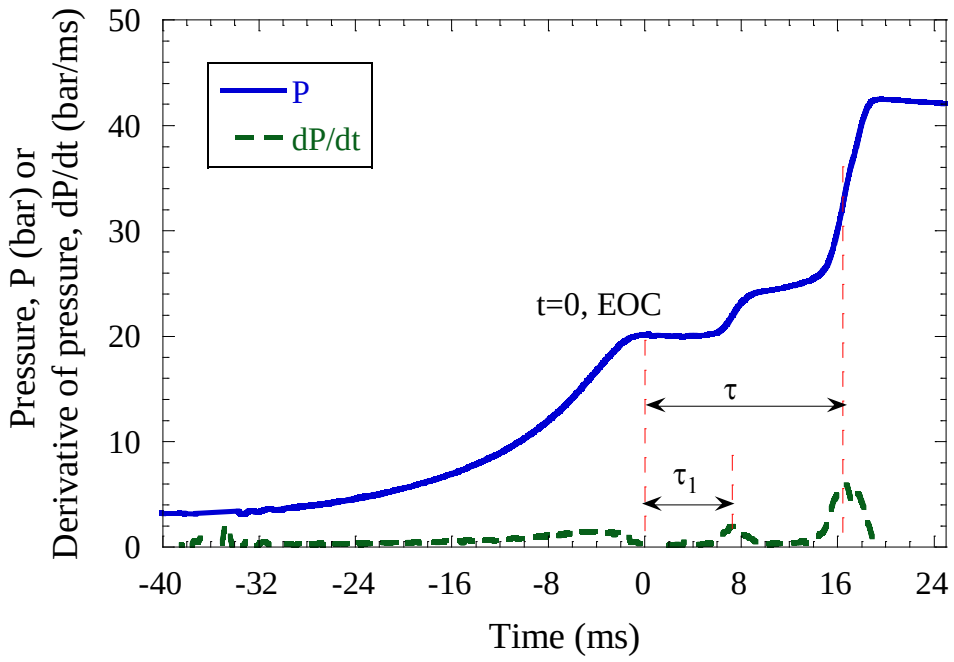

Figure 2.5 Plot showing the definitions of first-stage ignition delay (τ_1) and total ignition delay (τ) used in the current study. Conditions: ULSD#2/air, ϕ=0.5, P_C=20 bar, and T_C=678 K.

2.2.2.3 Repeatability of the experimental data:

A minimum of four consecutive runs are conducted at each condition and the value closest to the mean of the measured ignition delays is reported as the representative value. Figure 2.5 shows the comparison of the pressure trace records obtained using the tetralin+air mixtures of equivalence ratio of ϕ=0.5. The scatter in τ is less than 15% of the representative value for all the cases investigated here.

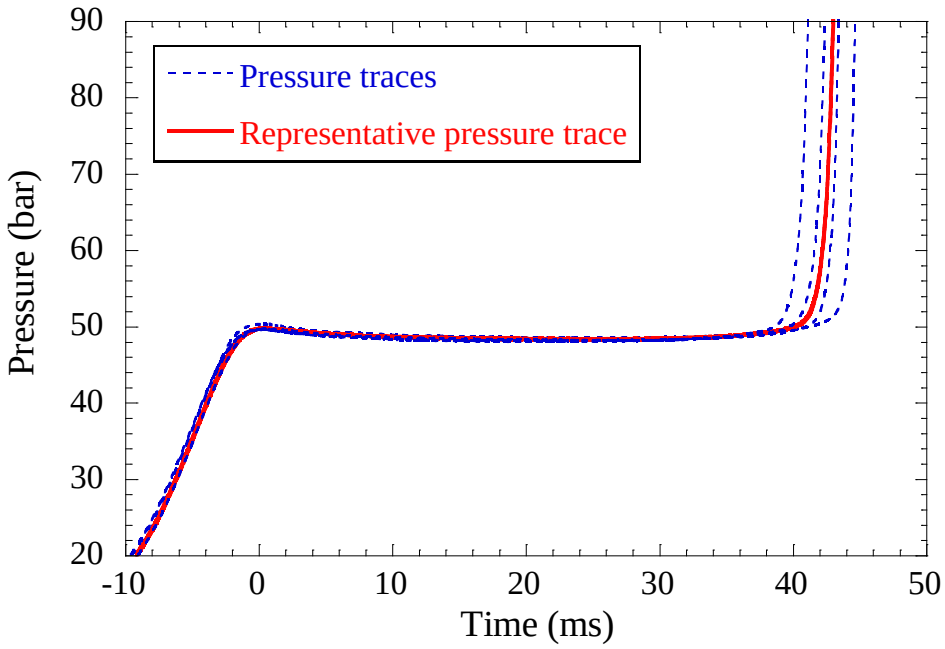

Figure 2.6 Plot demonstrating the repeatability of the current ignition delay measurements. Conditions: Tetralin/air, ϕ=0.5, P_C=50 bar, and T_C=796 K.

2.3 Numerical Specifications

2.3.1 RCM Simulations

The experimental pressure traces shown in Figs. 2.3-2.6 demonstrate that the instantaneous pressure in the reaction chamber drops right after the end of compression stroke due to the heat transfer between the hot compressed gas and the colder reaction chamber walls. The heat transfer results in change in both the pressure and temperature of the core gas mixture which inturn affects the resulting ignition delay. Furthermore, the test mixture during the compression phase, even without exhibiting any significant heat release, can still lead to the buildup of radical pool which can affect the simulated ignition delay [20]. The simulations conducted in the current studies capture the effect of the thermodynamic and chemical processes by conducting a "full RCM simulation". In a "full RCM simulation" or a "VPRO simulation" a volume history is specified to

replicate the thermodynamic states experienced by the test gas during the RCM experiment. This volume history includes both the compression phase and the post compression period, and is modeled using the adiabatic core hypothesis along with the corresponding nonreactive pressure trace. The nonreactive experiment is conducted by replacing O_2 with N_2 in the corresponding reactive mixture while maintaining the same fuel concentration such that a similar specific heat ratio of the mixture is maintained and similar heat transfer characteristics exist between the reactive case and the nonreactive counterpart. The measured pressure traces from the nonreactive experiments were thus used to generate volume time histories during and after compression in conjunction with the adiabatic core hypothesis. Further details about the generation of the volume histories can be found in [12].

Figure 2.7a shows an example of the volume history which is specified to conduct an RCM simulation. Both the compression stroke and the volume expansion post compression can be seen in the Fig 2.7a. The decrease in volume from t=0 to t≅0.038 sec models the compression stroke while the increase in volume post compression t>0.038 ms models the pressure drop observed in the experiments. Figure 2.7b shows the comparison of the pressure traces from RCM simulations and experiments. The nonreactive simulation shown in Fig2.7b corresponds to an RCM simulation in which O_2 is replaced with N_2. As seen in the fig 2.7b, the pressure traces from experiments and nonreactive simulations overlap during the compression stroke and the chemical induction times post compression thus ensuring that the thermodynamic states experienced by the mixtures during the experiments are reproduced faithfully while conducting the simulations. The pressure traces from a RCM reactive simulation is also shown in Fig. 2.7b. The RCM simulations are used to determine the ignition delays and the pressure history predicted by the chemical kinetic models and compared with their experimental counterparts to assess the performance of the models.

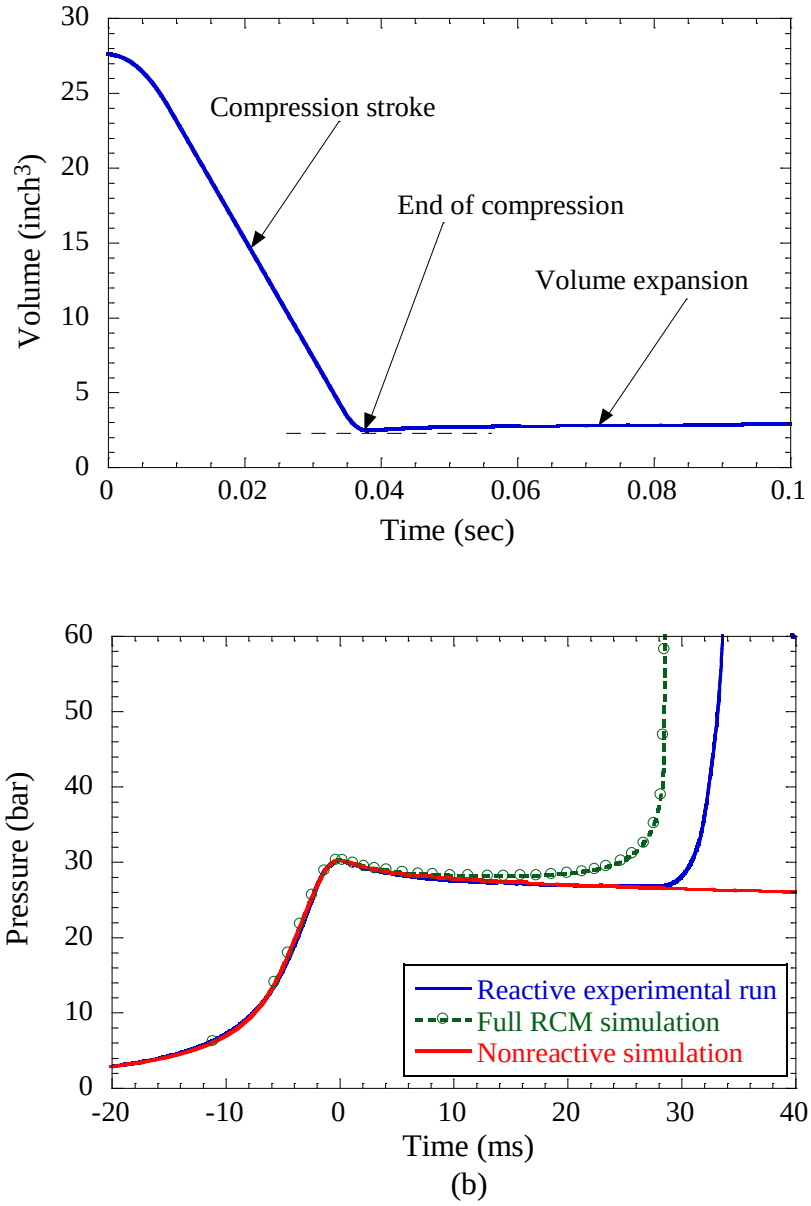

Figure 2.7 Plot showing the (a) volume history and (b) pressure traces obtained from experiments and simulation.

For some cases, a constant volume, adiabatic reactor initialized to the pressure and temperature conditions at the EOC (i.e., P_C and T_C), referred to as CONV simulations is conducted. All the VPRO and CONV simulations were conducted using CHEMKIN-Pro package [21].

2.3.2 Reaction Path Analysis

Reaction pathway analyses help in understanding the important oxidation reactions of fuels predicted by the chemical kinetic model. The relative contributions of various reactions in production or consumption of parent fuel and intermediate species are identified in this analysis.

2.3.3 Brute Force Sensitivity Analyses

In brute force sensitivity analysis, the pre-exponential factors of the reactions are separately multiplied by a factor of 5.0 and 0.2 one at a time and ignition delays with the modified reactions were computed from CONV simulations. The sensitivity index representing the effect of change of the reaction rate coefficient on ignition delay (hence on reactivity) is defined as $\left(\ln\frac{\tau_{5.0}}{\tau_{0.2}}\right) / \left(\ln\frac{5.0}{0.2}\right)$, where $\tau_{0.2}$ and $\tau_{5.0}$ are the simulated ignition delays using the reaction rate multiplied by 0.2 and 5.0, respectively. A negative (positive) sensitivity index implies that increasing the reaction rate accelerates (decelerates) ignition resulting in a shorter (longer) ignition delay. The sensitivity coefficients help in identifying the controlling chemistry at varying pressures, temperatures, and equivalence ratios. The brute force sensitivity analyses were conducted using the sensitivity program from [22].

Chapter 3 : Tetralin

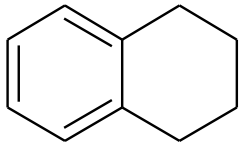

Figure 3.1 Skeletal structure of tetralin.

3.1 Introduction

1,2,3,4-tetrahydronapthalene, commonly known as tetralin, is a naphtheno-aromatic hydrocarbon found in diesel fuels. As such, tetralin has been proposed as a constituent in surrogate fuels [9,23]. The structure of tetralin is shown in Fig. 3.1. To date, very few studies [24–26] have focused on studying the fundamental combustion characteristics of tetralin. Yang and Boehman [24] studied ignition characteristics of tetralin in a CFR engine and compared the ignition propensity of tetralin with those of methylcyclopentane and decalin. Yang and Boehman [24] also conducted a detailed product analysis to understand the important reaction pathways of tetralin oxidation. From the product analysis, Yang and Boehman [24] concluded that tetralin does not exhibit low temperature chemistry and that the oxidation of tetralin is dominated by dehydrogenation reactions leading to the formation of dialin and naphthalene. Wang et al. [25] measured ignition delays of tetralin/air mixtures using a shock tube at equivalence ratios of ϕ=0.5 and 1, and at pressures of 13 bar and near 38 bar for temperatures between 978 K and 1277 K. Dagaut et al. [26] studied the oxidation characteristics of diluted tetralin/oxidizer mixtures in a JSR, with the initial concentration of tetralin at 1000 ppm, in the temperature range of 800 K to 1400 K, at varying pressures between 1 atm and 10 atm, and over a range of equivalence ratios between 0.5 and 1.5.

In addition to the oxidation studies, the pyrolysis of tetralin has been studied by several researchers [27–31]. Tsang and Cui [27] studied pyrolysis of tetralin in a shock tube in the temperature range of 1000 K to 1400 K by measuring concentrations of products formed due to unimolecular decomposition and hydrogen atom induced decomposition. Using the concentrations of the pyrolysis products, Tsang and Cui [27] determined rate constants of several decomposition reactions and reactions of tetralin with hydrogen radical. Yu and Eser [28] studied the pyrolysis chemistry of tetralin and decalin at near-critical and supercritical conditions. For the conditions investigated in their study, Yu and Eser [28] found 1-methylindan and naphthalene to be the dominant products with the yield of the former being always greater than the latter. Stewart et al. [29] studied supercritical pyrolysis of tetralin in a specially constructed flow reactor at varying pressures between 0.2 MPa and 10 MPa and varying temperatures between 700 K and 810 K. Stewart et al. [29] observed 1-methylindan, naphthalene, and *n*-butylbenzene to be the major products of supercritical pyrolysis of tetralin. Li et al. [30] studied pyrolysis of tetralin using a flow reactor at low pressures of 30 Torr and at varying temperatures from 850 K to 1500 K. Pyrolysis products were identified using synchrotron vacuum ultraviolet photoionization mass spectrometry, and Li et al. [30] concluded that tetralin pyrolysis is dominated by unimolecular decomposition and H-abstraction reactions at low pressures. Li et al. [30] also developed a kinetic model consisting of 149 species and 554 reactions that describes the pyrolysis chemistry of tetralin. Zámostný et al. [31] studied pyrolysis of tetralin along with fifty-five other hydrocarbon molecules at a temperature of 810 ^{o}C, pressure of 400 kPa, and residence times of 0.2 s to 0.4 s. Naphthalene was found to be the major product from pyrolysis of tetralin for the conditions investigated by Zámostný et al. [31].

Only one model describing the oxidation kinetics of tetralin has been presented in the literature to our knowledge. In the work of Dagaut et al. [26], their chemical kinetic model was found to predict the ignition delays from the shock tube work of Wang et al. [25], the speciation measurements from the JSR work of Dagaut et al. [26], and the pyrolysis data of Li et al. [30] and Zámostný et al. [31] to a reasonable agreement.

The objective of the current study is to investigate the autoignition characteristics of tetralin at low-to-intermediate temperatures and elevated pressures using an RCM. These engine-relevant conditions have not been extensively studied in the literature. Further, the high quality experimental data from the RCM will be compared with the simulated results using the chemical kinetic model from the work of Dagaut et al. [26]. In addition, several chemical kinetic analyses of the model will be conducted to elucidate the underlying mechanics of the autoignition delay predictions under the conditions of the present experiments. In the following, we will sequentially detail the experimental specification, test conditions, experimental results, model performance assessment, and chemical kinetic analyses and discussion.

3.2. Experimental Specifications

3.2.1 Test Conditions

Table 3.1 summarizes the test conditions investigated in the current study, including equivalence ratio (ϕ), mole percentage of tetralin ($X_{tetralin}$), mole percentage of N_2 (X_{N2}), mole percentage of O_2 (X_{O2}), and P_C, investigated in the current study. The test conditions were designed to study the effects of pressure, equivalence ratio, fuel loading, and dilution on the autoignition of tetralin. In addition, experiments conducted in "air" (O_2:N_2=1:3.76 by mole) were designed to provide ignition delay data that will complement the existing shock tube data of Wang et al. [25].

Table 3.1: Tetralin test conditions

ϕ	Oxidizer	$X_{tetralin}$ (%)	X_{O2} (%)	X_{N2} (%)	P_C (bar)
0.5	Diluted	0.40	10.42	89.18	35, 50
1.0	Diluted	0.80	10.42	88.78	35, 50
0.5	Air	0.80	20.84	78.36	15, 35, 50
1.0	Air	1.60	20.67	77.73	15, 35

Further, the initial temperatures used to conduct experiments were chosen to ensure that the fuel injected into the mixture preparation chamber is completely vaporized. The saturated vapor pressures of tetralin at preheat temperatures of T_0=380 K, 400 K, and 420 K are 35 Torr, 73 Torr, and 145 Torr, respectively. As such, the maximum partial pressures of vaporized tetralin in the mixtures were kept at 22 Torr for T_0=380 K and 400 K and 45 Torr for T_0=420 K. The margin of safety between the partial pressure of tetralin and its saturation pressure ensures that no fuel condensation occurs in any of the experiments.

3.2.2 Mixture Preparation

The homogenous test mixtures are prepared according to the procedure described in Section 2.2.1 and the tetralin used in the experiments was 99% purity supplied by Sigma Aldrich®.

3.3 Experimental Results

3.3.1 Pressure Measurements

Examination of the pressure traces from the experiments shows that tetralin does not exhibit two-stage ignition behavior for any of the conditions investigated in this study. This is depicted for three representative conditions in Fig. 3.2. In addition, Fig. 3.3 shows a comparison between selected cases from Fig. 3.2a, and includes the nonreactive pressure traces corresponding to the two reactive experiments shown. Note that the pressure trace corresponding to the compressed temperature T_C=802 K (the red lines) has been offset by +5 bar for clarity in Fig. 3.3. Comparison of the reactive and nonreactive pressure traces illustrates some evidence of pre-ignition heat release. Since tetralin does not undergo two-stage ignition under the conditions investigated in this study, the term "pre-ignition heat release" is used. It can also be seen from Fig. 3.3 that the extent of pre-ignition heat release is higher at lower temperature, as indicated by the larger deviation of the reactive pressure trace from the nonreactive pressure trace at T_C=763 K.

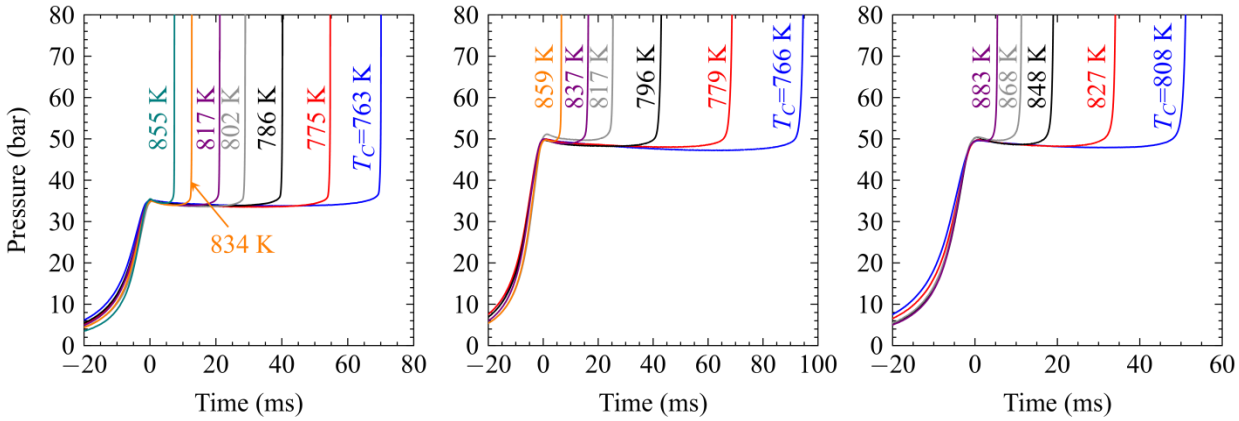

Figure 3.2 Representative pressure traces at three of the experimental conditions from Table 3.1. It can be seen that no evidence of two-stage ignition is found in the pressure traces.

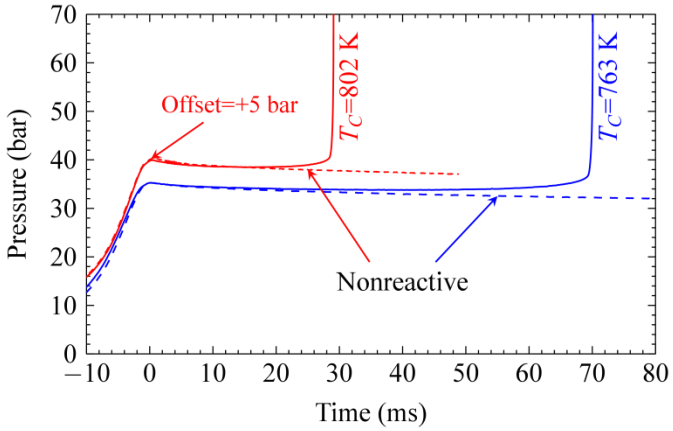

Figure 3.3: Pre-ignition heat release identified by comparison of pressure histories obtained from reactive and nonreactive experiments, for T_C=763 K and 802 K. The pressure trace for T_C=802 K is offset by +5 bar to clarify differences in the pressure traces. Conditions: ϕ=1.0 in air, Xtetralin=1.6%, and P_C=35 bar.

The larger extent of pre-ignition heat release at low temperatures as shown in Fig.3.3 could be because of weak low temperature reactivity of tetralin. Earlier experiments in a CFR engine conducted by Yang and Boehman [24] found that tetralin did not exhibit any pre-ignition heat release in the temperature range of 800−1000 K. In addition to different temperature ranges, this discrepancy in observations could be because the equivalence ratios, compressed pressures, and chemical induction times investigated in the current study are considerably higher than those from Yang and Boehman [24]. It is noted that Yang and Boehman [24] used lean tetralin/air mixtures at a fixed equivalence ratio of ϕ=0.25 for their investigation and the compressed pressures tested therein were less than 25 bar. On the other hand, the current study considers conditions up to 50 bar and the stoichiometric equivalence ratio (c.f., Table 3.1), as well as temperatures lower than 800 K.

3.3.2 Ignition Delay Measurements

Figure 3.4 shows Arrhenius plots of the ignition delays measured in this study. Also shown on Fig. 3.4 are error bars for the ignition delay and the compressed temperature. The error bars for the

ignition delay represent an uncertainty of ±10% of the ignition delay, corresponding to the maximum variation in the various experiments at a given condition. The error bars for the compressed temperature were estimated using the detailed uncertainty analysis method of Weber et al. [32]. In this study, we used the Monte Carlo method detailed by Weber et al. [32] and considered the uncertainty in measurements of the initial pressure, compressed pressure, initial temperature, ambient temperature, mixing tank volume, injected fuel mass, and proportions of oxygen and nitrogen. From this analysis, the error in T_C was estimated to be less than ±0.5% of the deduced compressed temperature of a given experiment, and hence error bars of ±0.5% are drawn for the inverse temperatures ($1000/T_C$) in Fig. 3.4. For clarity, only the first and last points have error bars; error bars for the other points have substantially similar sizes.

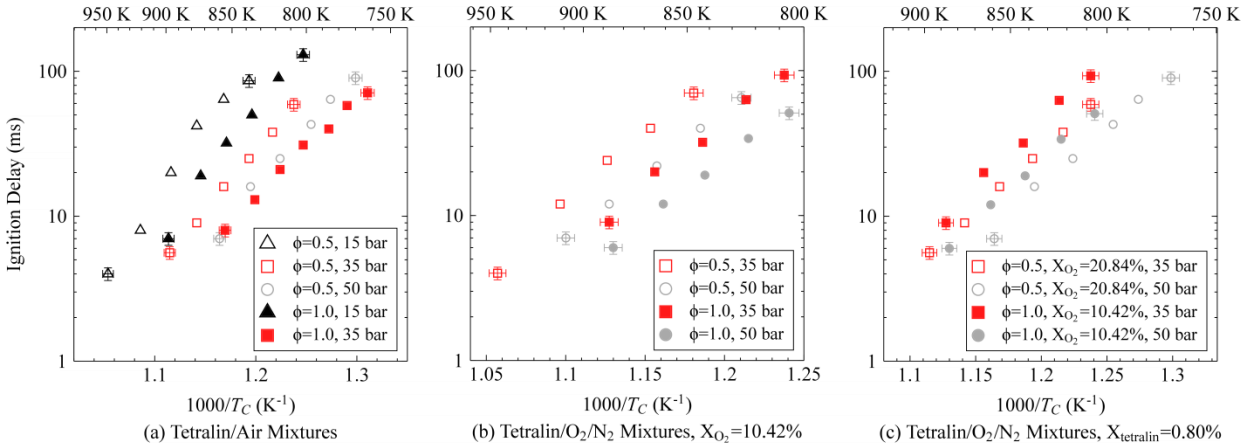

Figure 3.4 Arrhenius plots of ignition delays of tetralin/oxidizer mixtures at varying pressures and equivalence ratios.

In Fig. 3.4, it can be observed that the ignition delays decrease monotonically with compressed temperature and compressed pressure for all of the conditions in this study. The monotonic decrease of ignition delay with compressed temperature indicates that there is no negative temperature coefficient (NTC) region of the ignition delays in the present experiments. This is another reason why we prefer the term "pre-ignition heat release" for the behavior discussed in conjunction with Fig. 3.3. It appears that the low temperature chemistry of tetralin is not strong

enough to generate a two-stage ignition response or an NTC behavior, although it does generate noticeable heat release prior to hot ignition. The weak low temperature reactivity of tetralin could be because of its structural characteristics, particularly the presence of an alkyl ring and an aromatic ring. The chain initiation reactions on the cycloalkyl ring lead to the formation of conjugated alkenes, reducing the importance of the typical low temperature pathways [24,26]. However, it should be noted that the dominant reactions leading to the formation of conjugated alkenes does not necessarily eliminate the propagation of the reactants through the low temperature pathways during the oxidation of tetralin. In particular, at high pressures and low temperatures, such as those investigated in the current study, the low temperature pathways may compete with reactions generating conjugated olefins, leading to the weak low temperature reactivity observed in the present experiments. Thus, the radical pool generated by the low temperature pathways can accelerate ignition, even for conditions at which only weak exothermicity is observed.

In addition, in Figs. 3.4a and 3.4b it can be observed that the ignition delay decreases monotonically with increase in equivalence ratio for tetralin/oxidizer mixtures under the conditions studied in the present work. Figure 3.4a shows mixtures of tetralin in air, for which the initial fuel mole fraction changes by −50% from ϕ=1.0 to ϕ=0.5, while the initial oxygen mole fraction changes by only +1% for the same conditions. In Fig. 3.4b, the initial oxygen molar percentage is fixed at 10.42%, while the initial fuel mole fraction changes by −50% from ϕ=1.0 to ϕ=0.5. Thus, Figs. 3.4a and 3.4b indicate the effect of changing initial fuel mole fraction on the ignition delay and in both cases, increasing the initial fuel concentration (i.e., increasing the equivalence ratio) decreases the ignition delay. Figure 3.4c shows the effect of varying initial oxygen mole fraction at a fixed initial fuel mole fraction. In this case, lower equivalence ratios with higher initial oxygen mole fraction by keeping initial fuel mole fraction constant result in shorter ignition delays. This

result is consistent with other works in the RCM, including studies on *n*-decane [16], jet fuels [33], and *n*-butanol [15].

3.3 Comparison of Ignition Delays of Tetralin and *n*-Butylbenzene

Figure 3.5 shows the comparison of ignition delays of tetralin obtained from the current study and *n*-butylbenzene available in the literature [34,35]. This comparison of the ignition delays provides insights into the understanding of fuel structure effect on ignition propensities and fuel chemistry, as tetralin and *n*-butylbenzene have the same number of carbon atoms. *n*-Butylbenzene has an aliphatic C_4 chain attached to a phenyl ring while the C_4 chain in tetralin forms the bulk of the second ring attached to the phenyl. The structures of *n*-butylbenzene and tetralin are shown and compared in Fig. 3.6.

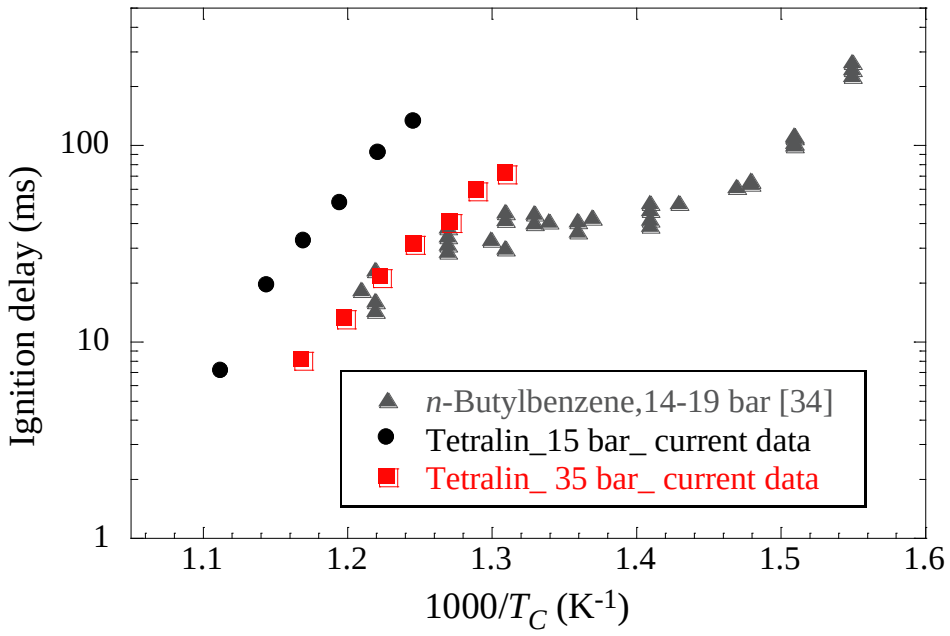

(a) ϕ=1, fuel+oxidizer mixtures

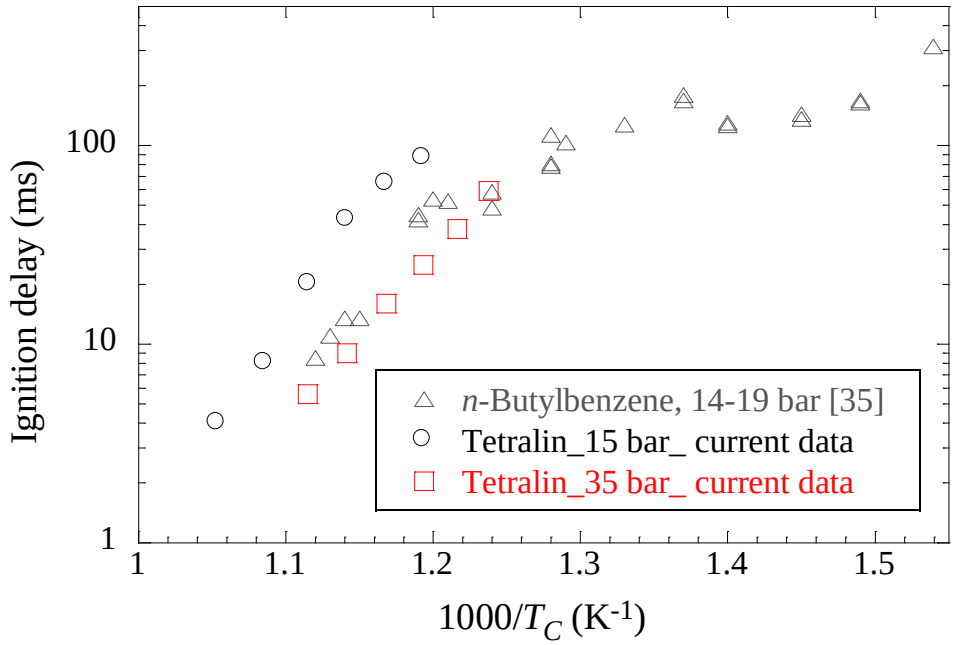

(b) ϕ= 0.5, fuel+oxidizer mixtures

Figure 3.5 Comparison of ignition delays of *n*-butylbenzene and tetralin.

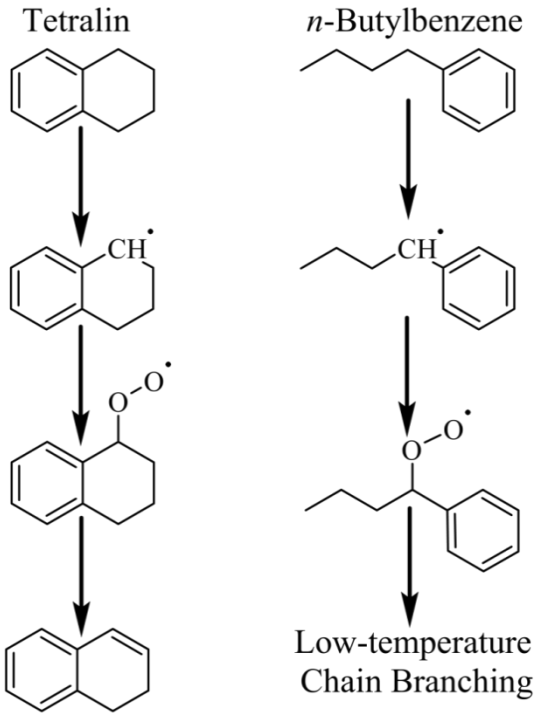

Figure 3.6 Schematic of important reactions in tetralin and *n*-butylbenzene low-temperature ignition. Note that chain branching steps are possible from any carbon in the butyl chain for n-butylbenzene; for further discussion of the reaction pathways of *n*-butylbenzene, the interested reader is referred to the work of Husson et al. [35].

It is observed in Fig. 3.5 that tetralin is less reactive than *n*-butylbenzene. The differences in reactivity could be explained by the relative importance of low-temperature chain-branching reactions over the chain-propagating or chain-terminating reactions. In particular, the C_4 aliphatic chain in *n*-butylbenzene facilitates low-temperature chain-branching reactions while the cyclic structure in tetralin favors formation of conjugated alkenes. These reactions are shown schematically in Fig. 3.6 for each of the two fuels. The conjugated olefin producing pathways dominate for tetralin, and hence the low-temperature reactivity of tetralin is reduced as compared to that of *n*-butylbenzene. As further evidence of this point, Husson et al. [35] noted first-stage ignition in their ϕ=0.5 experiments for *n*-butylbenze, while no first-stage ignition occurred for

tetralin in the present experiments. Regarding the reaction pathways of *n*-butylbenzene, the interested reader is referred to the study of Husson et al.[35].

3.4. Chemical Kinetic Analyses

3.4.1 Ignition Delay Simulations

To the best of our knowledge, the semi-detailed chemical kinetic model developed by Dagaut et al. [26] is the only reaction mechanism which describes the oxidation of tetralin. This reaction mechanism has been made on a hierarchical model and the oxidation of tetralin involves 30 major reaction types [26]. As mentioned previously, this mechanism has been shown to have good performance in predicting the speciation data from a JSR [26] and ignition delays from a shock tube [25].

Two types of simulations were conducted using the mechanism of Dagaut et al. [26]. The first is a "VPRO simulation" or "Full RCM simulation" that reproduces the compression stroke and post compression heat transfer processes inherent to RCM experiments. The second is CONV simulation. Details of these two procedures can be found in Section 2.2.1.

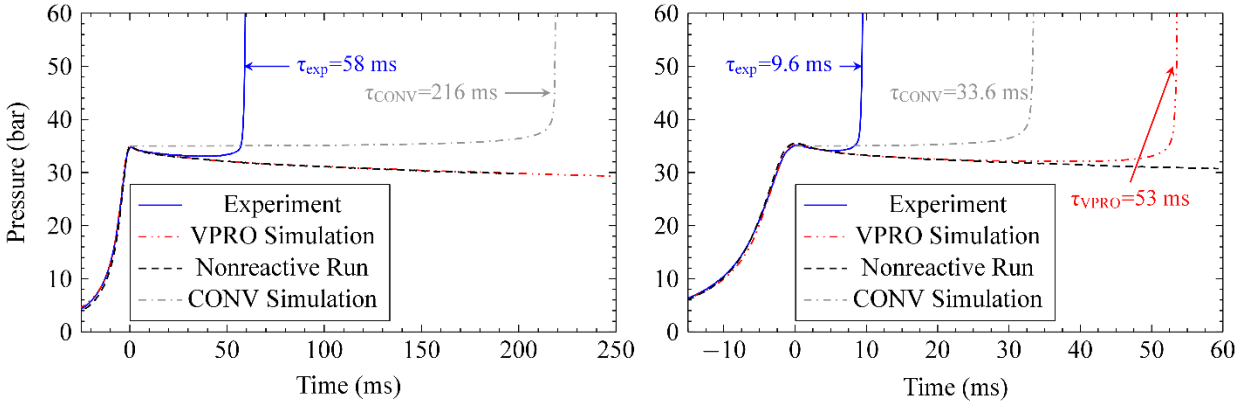

(a) ϕ=0.5, Tetralin/Air Mixture, P_C=35 bar, T_C=808 K

(b) ϕ=0.5, Tetralin/Air Mixture, P_C=35 bar, T_C=876 K

Figure 3.7 Comparison of measured pressure traces and computed profiles using CONV and VPRO simulations.

A comparison of these two simulation methods is shown in Fig. 3.7. For the case shown in Fig. 3.7a, ignition was not observed in the VPRO simulation during the experimental duration and the ignition delay from the CONV simulation was about a factor of four greater than that from the experiment. For the case shown in Fig. 3.7b, the ignition delay for the VPRO simulation was about a factor of five higher than the experimental value while the value from the CONV simulation was about a factor of four times greater than the experimental value.

Figure 3.8 shows the comparison of the ignition delays from experiments and VPRO simulations for the diluted conditions. It is noted that some of the VPRO simulations did not ignite within the computational duration (300 ms); simulated results for these cases are not shown on Figure 3.8. The simulated ignition delays are seen to be consistently greater than those from experiments showing that this mechanism is significantly less reactive than experiments.

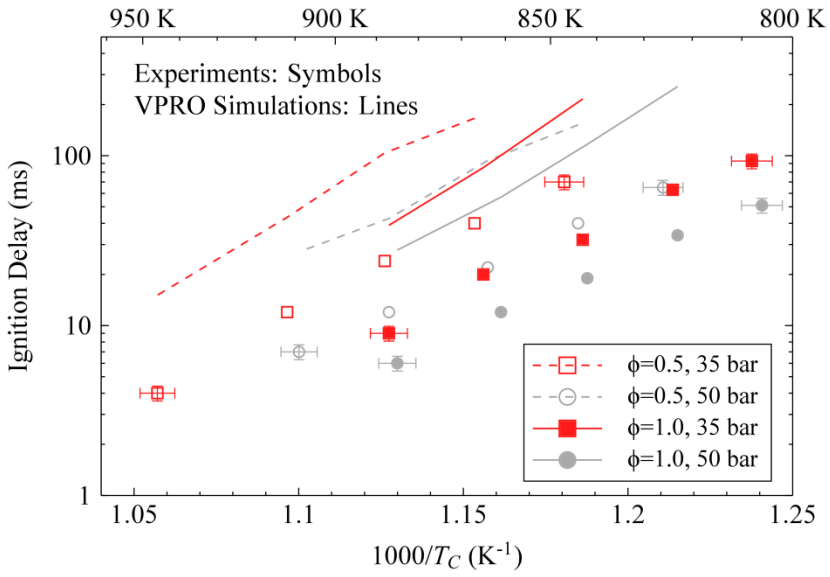

Figure 3.8 Comparison of experimental and simulated ignition delays for the diluted experiments – tetralin/O_2/N_2 mixtures with X_{O2}=10.42%.

Figure 3.9 shows a comparison of the ignition delays measured in this study with the ignition delays from the study of Wang et al. [25] in a shock tube, as well as a comparison of both

experiments with the predictions from the CONV simulations. CONV simulations are used for this comparison to have a consistent simulation method across the entire temperature range. Wang et al. [25] conducted their experiments at nominal pressures of 13 bar and near 38 bar. For the experimental data comparison shown in Fig. 3.9, the ignition delays from Wang et al. [25] were scaled to the current compressed pressures using the scaling factors suggested therein. It can be seen that the current RCM measurements at low-to-intermediate temperatures complement well with the literature shock tube data at high temperatures.

By comparing the model with the RCM experiments on the right of Figs. 3.9a and 3.9b, it is seen that the model over-predicts the ignition delay uniformly at both the equivalence ratios investigated in the current study, and the pressure dependence of the ignition delays at low temperatures is not well captured by the model. It is also noted that the mechanism performs relatively better at low pressures and low equivalence ratios. The discrepancy between experiments and simulations is likely due to the lack of detailed description of the low-to-intermediate temperature chemistry, which is known to be promoted by increase in equivalence ratio and pressure. Hence, the differences in experimental and simulated ignition delays are expected to be more severe at higher pressures and higher equivalence ratios, and less severe at lower pressures and lower equivalence ratios.

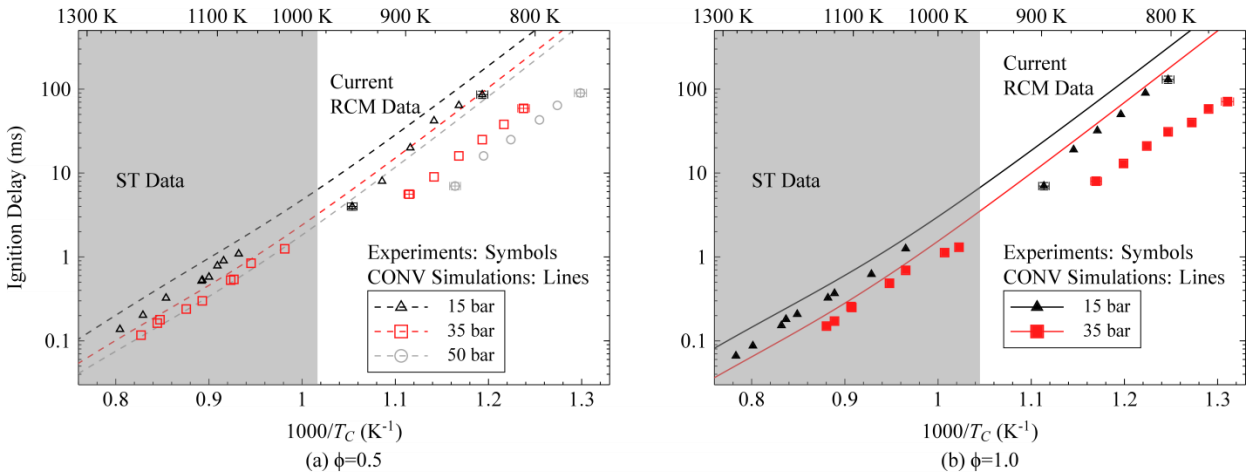

Figure 3.9 Arrhenius plots showing the complementary nature of ignition delays measured in this RCM study with the shock tube (ST) data taken from Wang et al. [25] at different pressures and equivalence ratios. All mixtures are tetralin/air. Computational results based on the CONV simulations are also plotted for comparison.

Figures 3.9a and 3.9b also show the performance of the mechanism in estimating the ignition delays at conditions investigated by Wang et al. [25]. As noted by Wang et al. [25], for the conditions investigated in their study the mechanism of Dagaut et al. [26] performed relatively better at high pressures, in opposition to the findings of the present study targeting at low-to-intermediate temperatures. The reason for this characteristic difference in the performance of the mechanism with pressure is currently unclear.

3.4.2 Reaction Path Analysis

Integrated reaction pathway analysis was conducted to understand the important oxidation reactions of tetralin predicted by the reaction mechanism of Dagaut et al. [26]. Analysis was conducted using CONV simulation with an initial pressure of 35 bar and an initial temperature of 835 K, at an equivalence of ϕ=0.5 in air. Moreover, analysis was conducted from the initial condition to the point of 10% fuel conversion. The 10% fuel conversion point was chosen to

identify controlling chemistry during the chemical induction time and also because the point of 10% fuel conversion is isolated from thermal runaway.

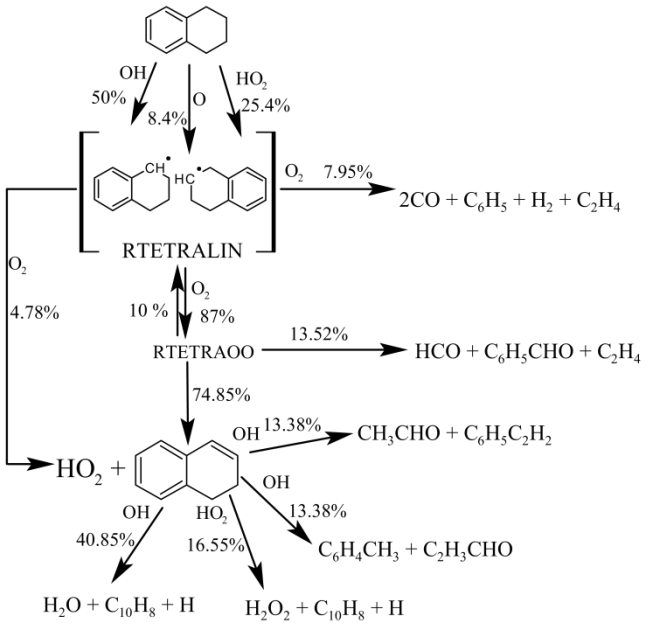

Figure 3.10 Integrated reaction path analysis up to 10% fuel conversion from an initial condition of 35 bar and 835 K for a ϕ=0.5 tetralin/air mixture in the CONV simulation.

Figure 3.10 shows the results of the integrated reaction path analysis. H-abstraction reactions from the alkyl ring of tetralin by O, OH, and HO_2 lead to the formation of tetralyl radical. It should be noted that the mechanism of Dagaut et al. [26] lumps the two possible tetralyl radicals into a single molecule called RTETRALIN. Reactions of RTETRALIN with oxygen (O_2) consume nearly all (>99.7%) of the tetralyl radicals. About 8% of tetralyl radical reacts with O_2 leading to the formation of carbon monoxide (CO), phenyl radical (C_6H_5), hydrogen (H_2), and ethylene (C_2H_4) as shown in (R1): $RTETRALIN+O_2 \rightarrow 2CO+C_6H_5+H_2+C_2H_4$.

The phenyl radical produced from (R1) is consumed entirely by reactions with oxygen (O_2). Reactions of phenyl radical with oxygen result in formation of highly reactive O radical as shown by (R2): $C_6H_5+O_2 \rightarrow C_6H_5O+O$. About 87% of tetralyl radical reacts with oxygen to form tetralyl

peroxy (denoted as RTETRAOO) as shown in (R3): RTETRALIN+O_2→RTETRAOO, which subsequently undergoes several dissociation reactions. The majority of the tetralyl peroxy, about 75%, dissociates to form dialin ($C_{10}H_{10}$) and hydroperoxyl radical (HO_2) as shown in (R4): RTETRAOO→$C_{10}H_{10}$+HO_2. The next important consumption reaction path way of tetralyl peroxy is the dissociation reaction which leads to formation of formyl radical (HCO), benzaldehyde (C_6H_5CHO), and ethylene (C_2H_4) as shown in (R5): RTETRAOO→C_2H_4+HCO+C_6H_5CHO. A small amount (<1%, not shown in Fig. 3.10) of tetralyl peroxy dissociates to form benzofuran (denoted as BZFUR), ethylene (C_2H_4), and OH radical by (R6): RTETRAOO→C_2H_4+OH+BZFUR.

As discussed previously, most of the tetralyl peroxy reacts to form dialin by (R4). Dialin is highly unreactive at the current conditions and only small amounts of it are consumed by the following reactions, (R7): $C_{10}H_{10}$+OH→H_2O+$C_{10}H_8$+H, (R8): $C_{10}H_{10}$+OH→$C_6H_4CH_3$+C_2H_3CHO, and (R9): $C_{10}H_{10}$+OH→CH_3CHO+$C_6H_5C_2H_2$. Reaction path analysis shows that dialin is predominantly consumed by (R7). Reactions of dialin with hydroxyl (OH) radical, including (R7)–(R9), consume highly reactive OH radicals and produce relatively lesser reactive species. In addition, more than 16% of dialin consumption is via its reaction with HO_2, (R10): $C_{10}H_{10}$+HO_2→H_2O_2+$C_{10}H_8$+H, resulting in the formation of napthalene ($C_{10}H_8$), H_2O_2, and H radical. While (R10) leads to the formation of H_2O_2, this reaction is not the most important contributor to H_2O_2 build-up.

For the temperatures currently investigated, the H radical produced from (R7) does not facilitate chain-branching reaction (R11): H+O_2→OH+O, but instead undergoes (R12): H+O_2(+M)→HO_2(+M) followed by (R13): HO_2+HO_2→H_2O_2+O_2 and (R14): H_2O_2(+M)→OH+OH(+M) [3]. Thus, (R7) can be classified as chain propagating for the current

conditions. As a consequence, the reactions of dialin tend to reduce the availability of OH for other reactions, such as H-abstraction from the fuel.

3.4.3 Brute Force Sensitivity Analyses

Brute force sensitivity analyses have been carried out to identify the controlling chemistry at varying pressures, temperatures, and equivalence ratios. Brute force sensitivity indices were calculated for the 129 core reactions which describe the oxidation of tetralin in the mechanism of Dagaut et al. [26]. These reactions represent all of the reactions of tetralin, tetralyl radical, tetralyl peroxy, and dialin, and are outlined as 30 reaction types in Table 1 in the work of Dagaut et al. [26]. We consider only these reactions because we are interested in investigating the effect of changes in the fuel chemistry; the chemistry of small radicals (e.g., H, OH, etc.) is known to be important to the low-to-intermediate temperature of hydrocarbons [3], so we do not consider it in this analysis.

The first set of sensitivity analyses was conducted to identify the controlling chemistry at several initial temperatures. Figure 3.11 shows the sensitivity indices for three initial temperatures (835 K, 1100 K, and 1500 K) at an initial pressure of 35 bar for ϕ=0.5 mixtures of tetralin in air. The first two temperatures (835 K and 1100 K) are chosen because they are representative of the temperatures investigated in the current study and those from Wang et al. [23]; the final temperature of 1500 K is chosen as in the range where high-temperature reaction paths take over from the low-to-intermediate temperature pathways. Similar analysis was conducted at 15 bar and largely similar results were found.

Figure 3.11 shows the sensitivity indices of the 10 reactions with the highest sensitivity at 835 K. H-abstraction from tetralin by hydroperoxyl radical (HO_2) exhibits the highest sensitivity and has a negative sign, as it leads to build-up of hydrogen peroxide that controls ignition through

(R13) and (R14). It is interesting that the competing reactions concerning oxygen reaction with RTETRALIN, (R1) and (R3), exhibit opposite sensitivity indices. Specifically, the breakdown of RTETRALIN, (R1), exhibits high negative sensitivity index (accelerating ignition) while the oxygen addition pathway, (R3), exhibits positive sensitivity index (decelerating ignition).

The integrated reaction path analysis shown in Fig. 3.10 helps in understanding the chemical kinetic reason for the observed results. The phenyl (C_6H_5) radical formed from (R1) participates in an exothermic reaction with oxygen molecule via (R2), leading to production of highly reactive oxygen atom (O). The O radical formed from (R2) abstracts hydrogen from the tetralin molecule leading to the formation of OH and tetralyl radicals. As such, the phenyl (C_6H_5) radical formed from (R1) initiates a chain-branching cycle and hence exhibits negative sensitivity (enhancing ignition).

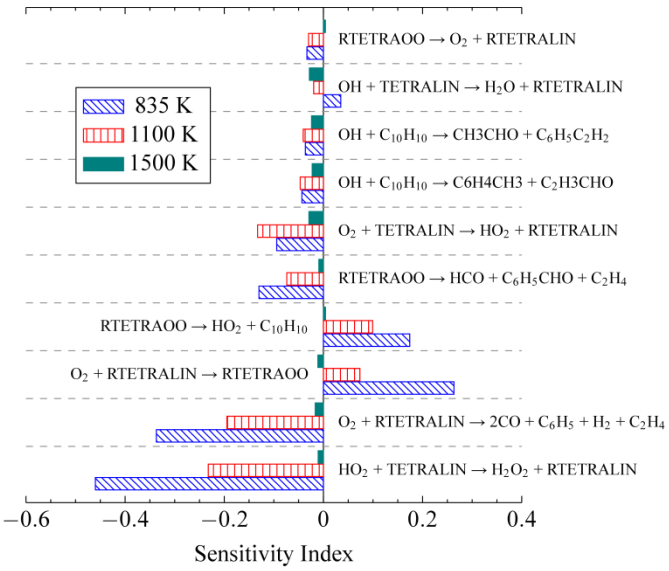

Figure 3.11 Brute force sensitivity of the ignition delay for ϕ=0.5 tetralin/air mixtures at an initial pressure of 35 bar for three initial temperatures in the CONV simulations.

On the other hand, the tetralyl peroxy produced from (R3), which competes with the reaction (R1), is predominantly consumed by the elimination reaction (R4) resulting in the formation of less reactive dialin and HO_2 radical. It should be noted that the dissociation reaction of tetralyl peroxy through (R4) exhibits a positive sensitivity index. The differences in reactivities of the products formed from (R1) and (R3) explain their contrasting sensitivity index signs. All the reactions of tetralyl peroxy which compete with the elimination reaction to form dialin, (R4), exhibit negative sensitivity. This can be explained on the basis that dialin, one of the products of (R4), acts as a radical scavenger (as discussed earlier) and products of the other competing dissociation reactions do not exhibit similar radical scavenging effect.

It is also of interest to note that, at 835 K and 1100 K, the reaction leading to formation of the tetralyl peroxy adduct, (R3), exhibits a positive sensitivity index while its reverse reaction (dissociation to tetralyl radical and O_2) exhibits a negative sensitivity index. These results are interesting as the reactions between fuel radicals and oxygen (O_2) leading to formation of the peroxy adduct are thought to accelerate the oxidation of hydrocarbons in the low-to-intermediate temperature range, including normal and branched alkanes [36,37], cycloalkanes [38,39], and unsaturated species [40]. This surprising result may be an artifact of the mechanism employed herein, arising due to the lack of comprehensive treatment of the low temperature reactions of tetralin oxidation. In particular, the mechanism considered here does not include any isomerization reactions of the tetralyl peroxy that are the typical entry point to the low-temperature chain branching processes. In addition, reaction (R3) has a small negative sensitivity at 1500 K and its reverse reaction has a small positive sensitivity. This is most likely because, at the higher temperature, only 5% of the tetralyl radical is directed into the oxygen addition pathway. This reduces the importance of the dialin formation pathways from tetralyl peroxy as shown by the

small value of the sensitivity index for the formation of dialin from tetralyl peroxy, (R4), at 1500 K.

Furthermore, it is interesting to note that the reaction of OH with tetralin to form water and tetralyl radical has a positive sensitivity at 835 K, but a negative sensitivity at the other two higher temperatures. This indicates that consuming OH radicals to form the primary fuel radical causes a decrease in the reactivity of the system at 835 K. This is most likely because the highly reactive OH consumed in this reaction is primarily turned into a dialin molecule through the reaction pathways discussed previously. The sensitivity of this reaction to form tetralyl radical is in contrast to the reaction of HO_2 with the fuel to form H_2O_2 and tetralyl radical. Although this reaction consumes one radical (HO_2) and the reaction pathways of tetralyl radical primarily form dialin, it also forms hydrogen peroxide, which is the primary source of hydroxyl in the system. Therefore, at low temperatures this reaction functions as a chain-branching reaction, whereas the reaction of hydroxyl with the fuel is effectively chain-terminating.

Finally, the sensitivity indices at 835 K shown in Fig. 3.11 do not change significantly with change in pressure (although not shown here). This weak change in sensitivity indices implies that the controlling chemistry does not change with pressure and indicates that the performance of the mechanism in predicting the ignition delays should not change with pressure. This is consistent with the observation in the current study that the mechanism is consistently less reactive than experiments at all pressures for temperatures investigated in the current work. Comparison of sensitivity indices at 1100 K for the two pressures also shows that the sensitivity indices do not change significantly with change in pressure. From this analysis, it is not clear why this mechanism performs relatively better at high pressures for the high temperature conditions investigated in the shock tube study of Wang et al. [25].

As mentioned previously, the simulated ignition delays were about a factor of four longer than the experimental values for the temperatures investigated in the current work. The factor of five change in the reaction rate for the reaction of HO_2 with the fuel to form H_2O_2 and tetralyl radical considered in this analysis causes approximately a 60% decrease in ignition delay at 835 K. Since a 400% improvement is required, changing the reaction rate of H-abstraction by HO_2 from the fuel to improve the result would require a change well outside the uncertainty range of this reaction rate. Furthermore, it is unclear how the uncertainty of the reaction (R1) may be estimated from the work of Dagaut et al. [26] because it is not an elementary reaction and thus the uncertainty of this reaction rate is not known explicitly.

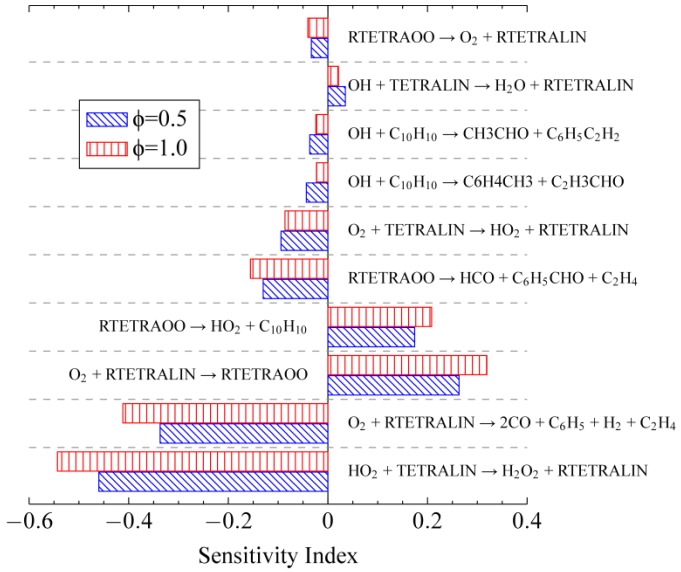

Figure 3.12 Brute force sensitivity of the ignition delay for ϕ=0.5 and ϕ=1.0 tetralin/air mixtures at an initial condition of 35 bar and 835 K in the CONV simulations.

A second set of sensitivity analyses was conducted to study the change in controlling chemistry with change in equivalence ratio, as it was found that the mechanism performs better at lower equivalence ratios. To identify the change in controlling chemistry, brute force sensitivity analysis based on the CONV simulations was conducted at an initial pressure and temperature of

35 bar and 835 K, respectively, at two equivalence ratios of ϕ=0.5 and 1.0 for tetralin/air mixtures. Comparison of brute force sensitivity indices with change in equivalence ratio is shown in Fig. 3.12. Figure 3.12 demonstrates that the controlling chemistry is similar to the results discussed in Fig. 3.11 and does not change with change in equivalence ratio.

From the sensitivity analyses it appears that simple modification of reaction rate coefficients is not enough to increase the fidelity of the mechanism and a more comprehensive description of the oxidation of tetralin, especially at low temperatures, is needed. The need for a more comprehensive description of oxidation at low-to-intermediate temperatures is supported by the evidence of pre-ignition heat release at low temperatures observed in the current study. The mechanism of Dagaut *et al.* [26] was developed on the premise that low temperature oxidation of tetralin is not effective as reported by Yang and Boehman [24]. This premise has been found to be inappropriate for the conditions in the current study. Furthermore, earlier studies have shown that the inclusion of low temperature reactions may be necessary for developing a high fidelity chemical kinetic model even for fuels that do not exhibit exothermicity in a CFR engine [41].

3.5 Conclusions

Ignition delays of tetralin/O_2/N_2 mixtures were measured using a heated rapid compression machine at varying pressures from 15 bar to 50 bar, temperatures between 763 K and 950 K, and equivalence ratios of ϕ=0.5 and 1.0. The effect of dilution was also studied by varying the initial concentrations of tetralin and oxygen independently. Pre-ignition heat release has been observed in the current study at the low end of the temperature range investigated; however, no evidence of NTC behavior of the ignition delays was found. Comparison of the ignition delays of tetralin and *n*-butylbenzene was also conducted to understand the effect of molecular structure on ignition propensity. In addition, comparison of experimental and simulated ignition delays showed the

available chemical kinetic model to be significantly less reactive than experiments. Reaction path analyses and brute force sensitivity analyses were conducted to understand the controlling chemistry of low-temperature tetralin autoignition. Brute force sensitivity analyses showed that simple modifications of reaction rate coefficients are not sufficient to improve the fidelity of the mechanism and a comprehensive model describing the low temperature reactions is needed to generate a high fidelity chemical kinetic model to predict the ignition delays and pre-ignition heat release observed in the present experiments.

Chapter 4 : 1-Methylnaphthalene

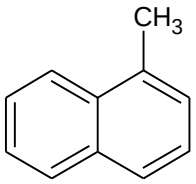

Figure 4.1 Skeletal structure of 1-methylnaphthalene.

4.1. Introduction

Since aromatic hydrocarbons constitute to about 30% (by weight) in diesel fuels [23,42], understanding their chemical kinetics is necessary for developing comprehensive oxidation models to describe ignition and combustion of surrogate fuels of diesel. 1-Methylnaphthalene (1-MN), also known as α-methylnaphthalene, is a substituted diaromatic hydrocarbon and has been used as a surrogate component, representative of aromatic hydrocarbons, for diesel in several studies [9,10,23,43]. The structure of 1-MN is shown in Fig 4.1. 1-MN is popularly used in diesel surrogate formulations as it was earlier used as a reference fuel for determining the cetane rating of a fuel. Recognizing the importance of understanding the autoignition characteristics of 1-MN, we aim to investigate its ignition delay times at engine-relevant conditions. In the following, the chemical kinetic studies on 1-MN reported in the literature are reviewed, including those conducted in a flow reactor [44,45], a jet stirred reactor [46], and shock tubes [47,48].

Shaddix et al. [44] studied the oxidation of 1-MN at atmospheric pressure in a flow reactor over initial temperatures of 1170–1200 K and at varying equivalence ratios of ϕ=0.6–1.5. Based on the analysis of their measured speciation profiles, Shaddix et al. [44] postulated that the oxidation of 1-MN is dominated by reactions of the 1-naphthylmethyl radical and the reactions of 1-MN with oxygen atom may also be significant. In their subsequent study, Shaddix et al. [45]

showed through the computed fuel decay path fluxes that under flow reactor conditions abstraction of a "benzylic" hydrogen from the methyl side chain dominates consumption of 1-MN, and oxygen atom addition to the aromatic ring, displacement of the side chain by hydrogen atom, and homolytic decay also contribute significantly. In addition, changes in the 1-MN decay mechanism under higher temperature combustion environments and the oxidation mechanisms of even larger polycyclic aromatic hydrocarbons were postulated in [45]. Mati et al. [46] studied the oxidation of diluted 1-MN+O_2+N_2 mixtures in a jet stirred reactor for pressures of 1–10 atm, temperatures of 800–1421 K, and equivalence ratios of ϕ=0.5–1.5. The authors also developed a chemical kinetic model to describe the oxidation of 1-MN [46], which was found to reproduce the experimental results to a good degree of agreement. Pfahl et al. [47] studied the autoignition of stoichiometric 1-MN+air mixtures behind reflected shock waves at a nominal pressure of 13 bar and temperatures of 840–1300 K. Wang et al. [48] studied the autoignition of 1-MN behind reflected shock waves at pressures of 8–45 atm, varying equivalence ratios of ϕ=0.5–1.5, and temperatures in the range of 1032–1445 K. A chemical kinetic model of 1-MN was also proposed in [48] that was found to predict the ignition delays and speciation measurements to good agreement. Further, Bounaceur et al. [49] proposed a chemical kinetic model of 1-MN and validated their model against the literature data. Narayanaswamy et al. [50] proposed a 1-MN model as well and validated their model against the flow reactor data of Shaddix et al. [44] and the ignition delay data from Pfahl et al. [47].

Review of the literature studies shows that the oxidation of 1-MN has not been investigated in detail at low-to-intermediate temperatures and the performance of the available chemical kinetic models at low-to-intermediate temperatures is not known. Realizing this, the autoignition characteristics of 1-MN has been studied in a rapid compression machine (RCM) herein. The current study provides ignition delay information of 1-MN at low-to-intermediate temperatures

with varying pressures and equivalence ratios. In addition, the ignition delays measured in the current study were used to assess the performance of the available models and such a comparison would help understand the areas where the improvements to the literature models can be made.

In the following sections, the experimental facility and the test conditions will be first described. Next, the experimental results will be presented and compared with the literature data. Subsequently, the simulated results using two chemical kinetic models taken from the literature will be shown and compared with the current experimental datasets. Based on the comparison, the results of reaction path analyses and brute force sensitivity analyses conducted at selected conditions will be discussed to identify the controlling chemistry and the potential areas required further studies to improve the comprehensiveness of the literature models.

4.2. Experimental Specifications

4.2.1 Test Conditions

Table 4.1 summarizes the test conditions, including equivalence ratio (ϕ), mole percentage of 1-MN ($X_{1\text{-MN}}$), mole percentage of O_2 (X_{O2}), and P_C, investigated in the current study. The test conditions were designed to study the effects of pressure and equivalence ratio on the autoignition of 1-MN over a range of compressed temperatures for T_C=837–980 K. The pressure and equivalence ratios were also chosen in order to provide ignition delay data at lower temperatures that will complement the existing shock tube data of Pfahl et al. [47] and Wang et al.[48]. Further, all the experiments were conducted at a preheat temperature of T_0=420.15 K.

Table 4.1: 1-MN experimental test conditions

ϕ	$X_{1\text{-}MN}$ (%)	X_{O2} (%)	P_C (bar)
0.5	0.77	20.85	15, 40
1.0	1.53	20.68	15, 30, 40
1.5	2.28	20.52	30

4.2.2 Mixture Preparation

The homogenous test mixtures are prepared according to the procedure described in Section 2.2.1 and the 1-MN used in the experiments was 95% purity supplied by Sigma Aldrich®.

4.3. Experimental Results

Figure 4.2 shows the experimental pressure traces recorded at varying compressed temperatures and equivalence ratios for P_C=30 and 40 bar. Observation of the pressure traces shows no evidence of two-stage ignition behavior. In addition, no evidence of strong pre-ignition heat release was found for the conditions tested in the current study. This is consistent with the shock tube experiments of Wang et al. [48], who reported that they did not observe any pre-ignition heat release in their experiments. It is also to be noted that since the conditions shown in Fig. 4.2 cover those with equivalence ratios ranging from fuel lean (ϕ=0.5) to fuel rich (ϕ=1.5) and elevated pressures of P_C=30 and 40 bar, it can be stated with confidence that 1-MN does not exhibit any significant pre-ignition heat release across wide range of pressures and temperatures.

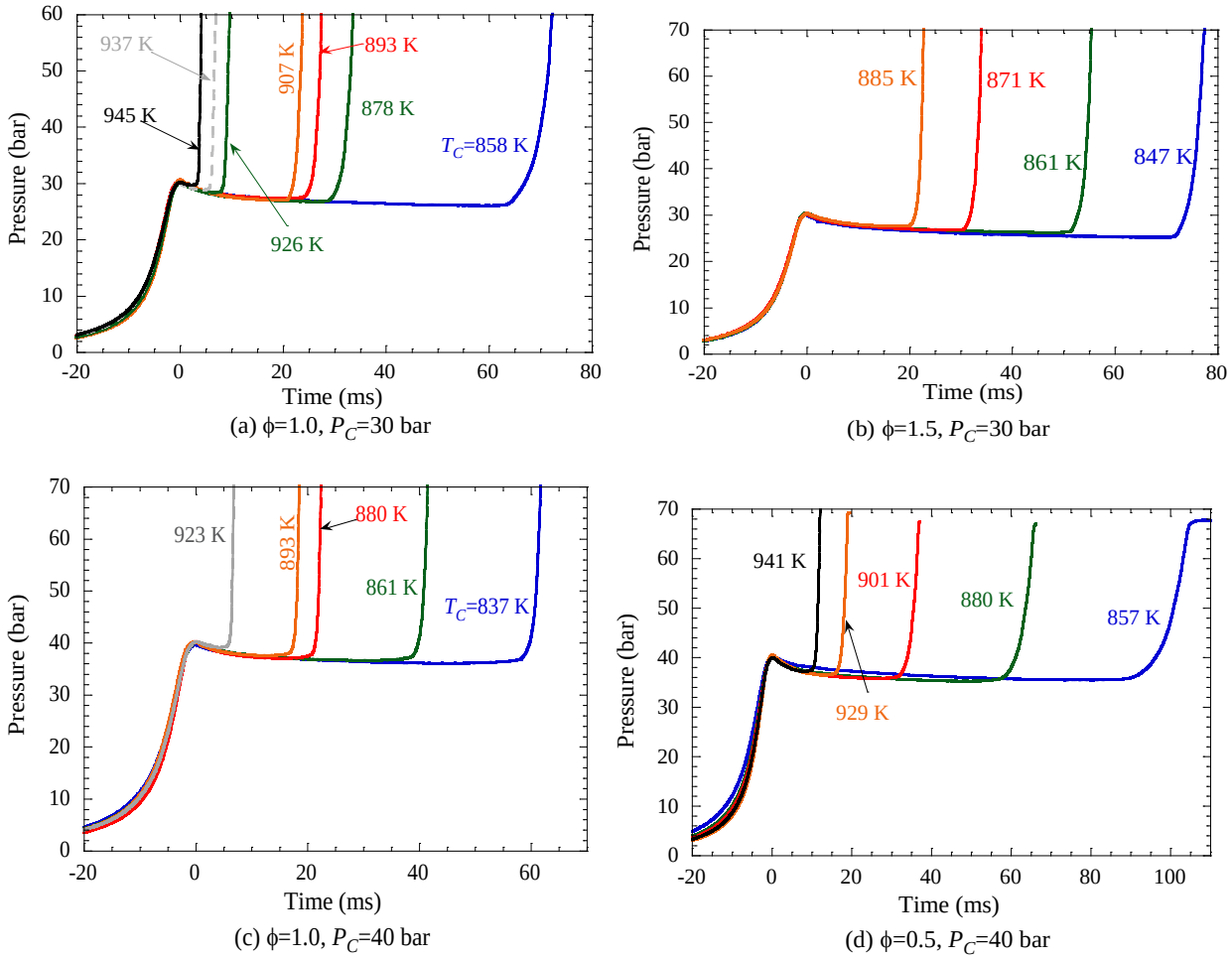

Figure 4.2 Plot showing the pressure traces at varying compressed pressures, compressed temperatures, and equivalence ratios.

Figure 4.3 shows the Arrhenius plots of the ignition delays obtained in this study. As mentioned earlier in section 2.2.2.3, the uncertainty in the reported ignition delay is about 15%. The ignition delays shown in Fig. 4.3 are seen to decrease monotonically with increasing temperature. Also shown in Fig. 4.3 are the ignition delay data from the shock tube experiments of Pfahl et al. [47] and Wang et al. [48]. It is noted that the shock tube ignition delay data have been scaled to the current experimental conditions using the pressure exponent (~$P^{-0.9}$) suggested by Wang et al. [48]. As seen from Fig. 4.3, the current ignition delay measurements complement and compare well with the shock tube data in the literature. Figure 4.3 also elucidates the

importance of the current RCM study in providing the ignition delay measurements at low-to-intermediate temperatures needed for chemical kinetic model validation.

The effect of equivalence ratio on ignition delay is shown in Fig. 4.5. The ignition delays are shown to decrease monotonically with an increase in equivalence ratio. Moreover, the change in ignition delays is larger when the equivalence ratio is increased from ϕ=0.5 to ϕ=1.0 at P_C=15 bar as opposed to the change when equivalence ratio is increased from ϕ=1.0 to ϕ=1.5 at P_C=30 bar. In the current study, the equivalence ratio was varied by changing the fuel concentration while maintaining the oxygen concentration nearly similar (c.f., Table 4.1). Therefore, the change in equivalence ratio is mainly due to the change in concentration of fuel. As such, the fuel concentration increases approximately by a factor of two when increasing equivalence ratio from ϕ=0.5 to ϕ=1.0 whereas the fuel concentration changes by about factor of 1.5 when increasing the equivalence ratio from ϕ=1.0 to ϕ=1.5. The difference in the amount of increase in fuel concentration coupled with the non-linear dependence of ignition delay on fuel concentration could be the reason for the larger change (decrease) in ignition delays when equivalence ratio is raised from ϕ=0.5 to ϕ=1.0 than that when increasing the equivalence ratio from ϕ=1.0 to ϕ=1.5, although the effect of pressure is expected to play a role as well.

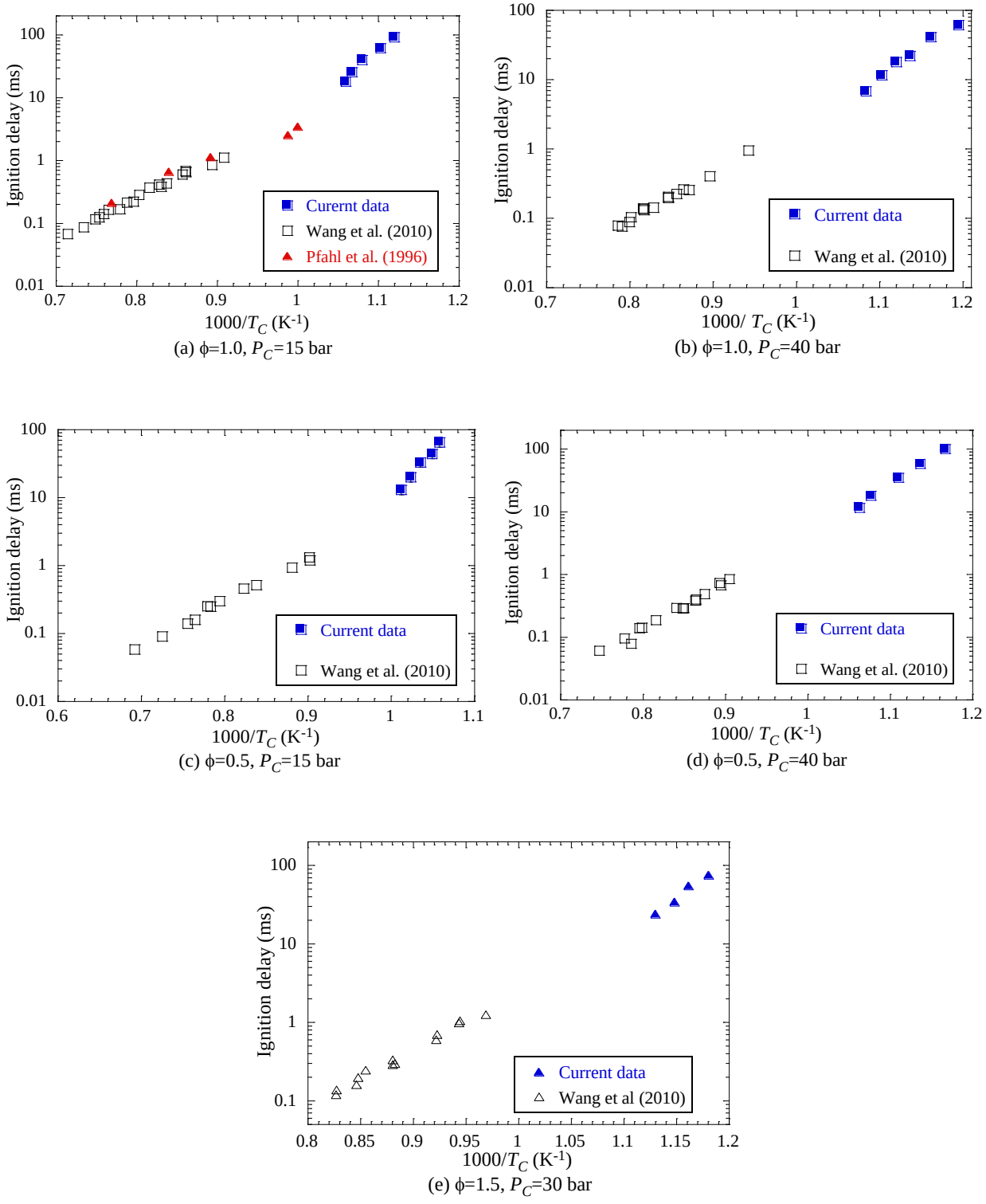

Figure 4.3 Comparison of ignition delays of 1-MN/air mixtures at varying compressed pressures, compressed temperatures, and equivalence ratios, obtained from the current RCM experiments and the shock tube experiments of [47,48].

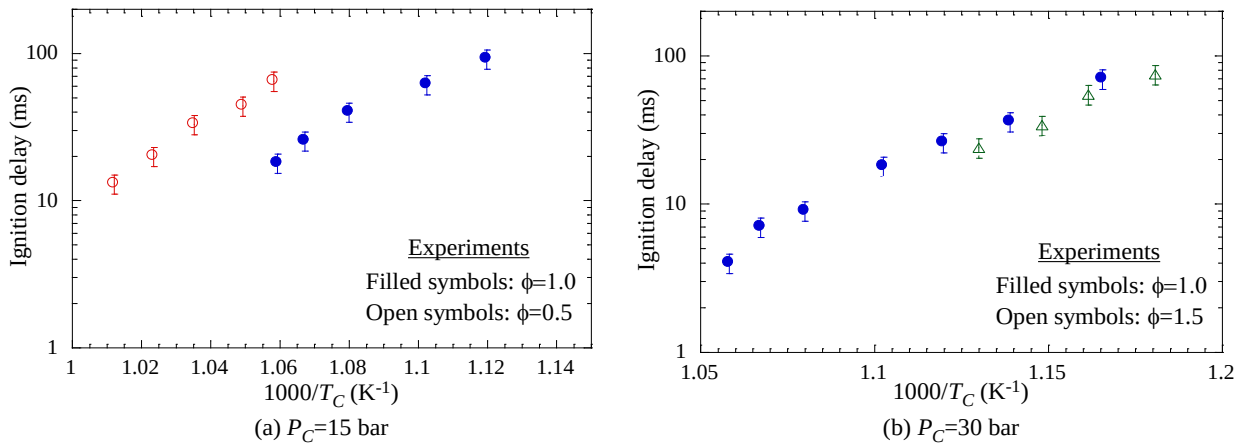

Figure 4.4 Plot showing the effect of equivalence ratio on ignition delay.

4.4 Simulated Results and Chemical Kinetic Analyses

As discussed earlier, there are several chemical kinetic models of 1-MN available in the literature [47,49-51]. In the current study, the model of Wang et al. [48] and Narayanaswamy et al. [50] were employed for simulating the experimental data and conducting the subsequent chemical kinetic analyses, as they are the latest models in the literature. It is further noted that the model of Wang et al. [48] was developed based on the works of Mati et al. [46] and Bounaceur et al. [49]. The model of Mati et al. [46] did not include the H-abstraction and H-replacement reactions on the aromatic rings whereas that of Bounaceur et al. [49] included these channels. Since the model of Wang et al. [48] considered all the possible abstraction reactions and the subsequent reactions in [46,49], the models of Mati et al. [46] and Bounaceur et al. [49] were not considered herein.

4.4.1 Ignition Delay Simulations

The ignition delay simulations were carried out using the Chemkin-Pro package [21] with the volume histories and the intake conditions from experiments. Unfortunately, there were issues with convergence of the solution when full RCM simulations were attempted with the model of Wang

et al. [48], while no such problem was encountered when using the model of Narayanaswamy et al. [50]. However, the convergence problem with the Wang et al. [48] model was not encountered in "post compression simulation", in which the simulation excludes the compression stroke and only the post compression period is modeled with P_C and T_C as the initial pressure and temperature, respectively. While the radical pool developed during the compression stroke is not captured in the post compression simulation, the comparison of the simulated results with and without modeling the compression stroke can be used to assess the importance of the compression stroke in RCM simulations.

Figure 4.5 shows the comparison of pressure traces from experiments and simulations using the chemical kinetic model of Narayanaswamy et al. [50]. The conditions shown in Figs. 4.5(a) and 4.5(b) correspond to relatively long (τ>30 ms) and short (τ<5 ms) experimental ignition delays, respectively. It can be seen that the ignition delays from simulations with and without modeling the compression stroke differ by about 17% for the condition corresponding to short test time while the difference is about 11% for the long test time condition. Based on Fig. 4.5, it is conservatively assumed that the difference in simulated ignition delays between "full RCM simulation" and "post compression simulation" is generally about 15% for the conditions investigated here.

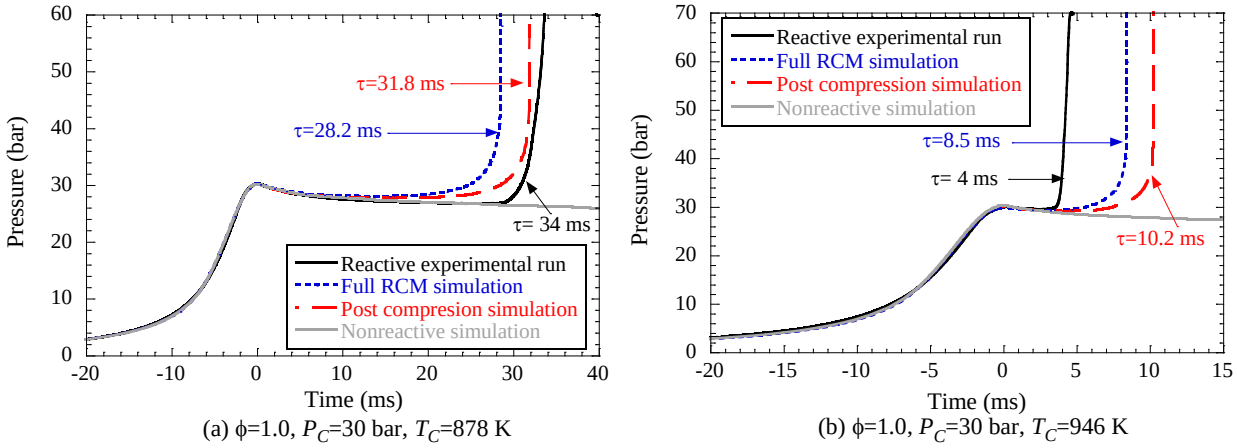

(a) ϕ=1.0, P_C=30 bar, T_C=878 K (b) ϕ=1.0, P_C=30 bar, T_C=946 K

Figure 4.5 Plot showing the different types of simulations conducted in the current study and their comparison with the experimental results.

In the next sections, the experimental and simulated ignition delay results will be compared. For clarity, it is noted that the full RCM simulations were conducted when using the model of Narayanaswamy et al. [50], while the post compression simulations were used when employing the model of Wang et al. [48].

4.4.1.1 Simulations with Wang et al. Model

Figure 4.6 shows the comparison of the experimental and simulated ignition delays obtained using the chemical kinetic model of Wang et al. [48] at various test conditions. For the stoichiometric and fuel rich conditions investigated, the model of Wang et al. [48] is consistently more reactive than the current experiments conducted at lower temperatures. In particular, the simulated ignition delays are approximately a factor of two lower than the experimental values for the conditions of ϕ=1.0 and ϕ=1.5. Additionally, the difference in simulated and experimental ignition delays of stoichiometric mixtures gradually increases with decreasing temperature. For the fuel lean condition (ϕ=0.5), on the other hand, the simulated ignition delays compare reasonably well with the experiments at P_C=15 bar while the model is significantly less reactive than the experiments at P_C=40 bar.

For P_C=40 bar at a similar T_C value, Fig. 4.7 compares the experimental and simulated pressure traces at stoichiometric and fuel lean conditions. For the stoichiometric condition, Fig. 4.7(a) shows that the simulated pressure trace using the model of Wang et al. [48] displays significant pre-ignition heat release, while the experimental profile indicates otherwise. It is seen from Fig. 4.7(b) for the fuel lean condition that the simulated pressure history using the model of Wang et al. [48] exhibits a two-stage ignition like behavior. This is somewhat surprising and unexpected for 1-MN. As shown in Figs. 4.2 and 4.5, no evidence of such distinct pressure profile was noticed in the current RCM experiments.

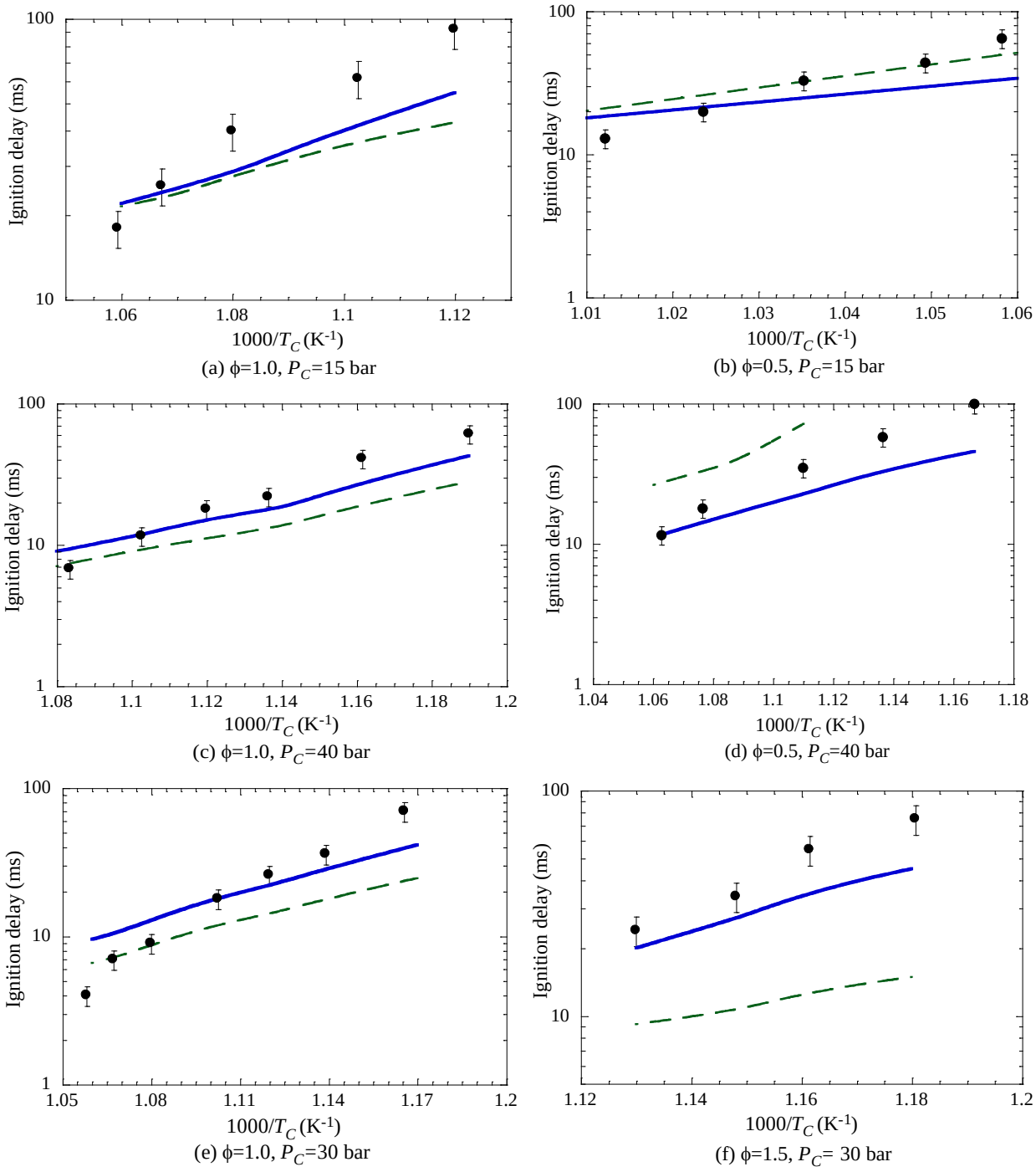

Figure 4.6 Comparison of the ignition delays from experiments and simulations. Filled symbols: experiments. Broken lines: simulations using the model of Wang et al. [48]. Solid lines: simulations using the model of Narayanaswamy et al. [50].

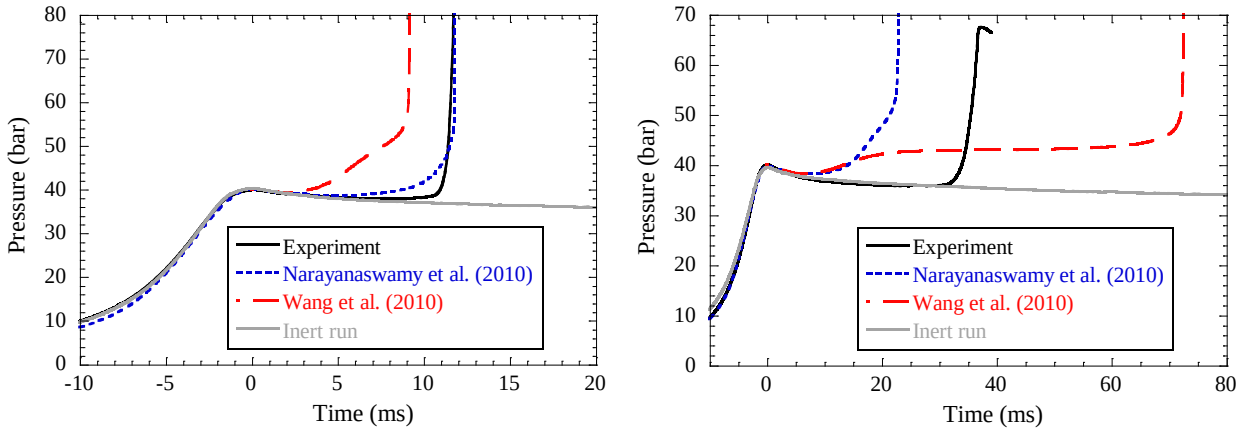

(a) ϕ=1.0, P_C= 40 bar, T_C = 907 K (b) ϕ= 0.5, P_C= 40 bar, T_C = 901 K

Figure 4.7 Plot showing the comparison of pressure traces from experiments and simulations.

One possible reason for this model to predict such a distinct pressure profile could be that the intermediates which are formed during the chemical induction period are not consumed, thereby delaying the hot ignition event. In order to check this hypothesis, a simple adiabatic constant volume simulation was conducted to examine the intermediate species concentration profiles. Figure 4.8 shows such results for ϕ=0.5 with initial conditions of 40 bar and 900 K. This simulation demonstrates that more than 90% of the parent fuel, 1-MN (A2CH3), is consumed by the end of the first-stage like pressure rise and 1-MN gets converted to several intermediates. The major intermediates formed are A1OC6H4Obis, A1OC6H4O, 1-naphthanol (C10H7OH), 1-napthaldehyde (C10H7HCO), and C18H14. The chemical structures of these intermediate species are shown in Fig. 4.8(b). From Fig. 4.8 such high concentrations of the intermediates support our hypothesis that the pressure history observed from the simulation is because of the slow oxidation of these intermediates.

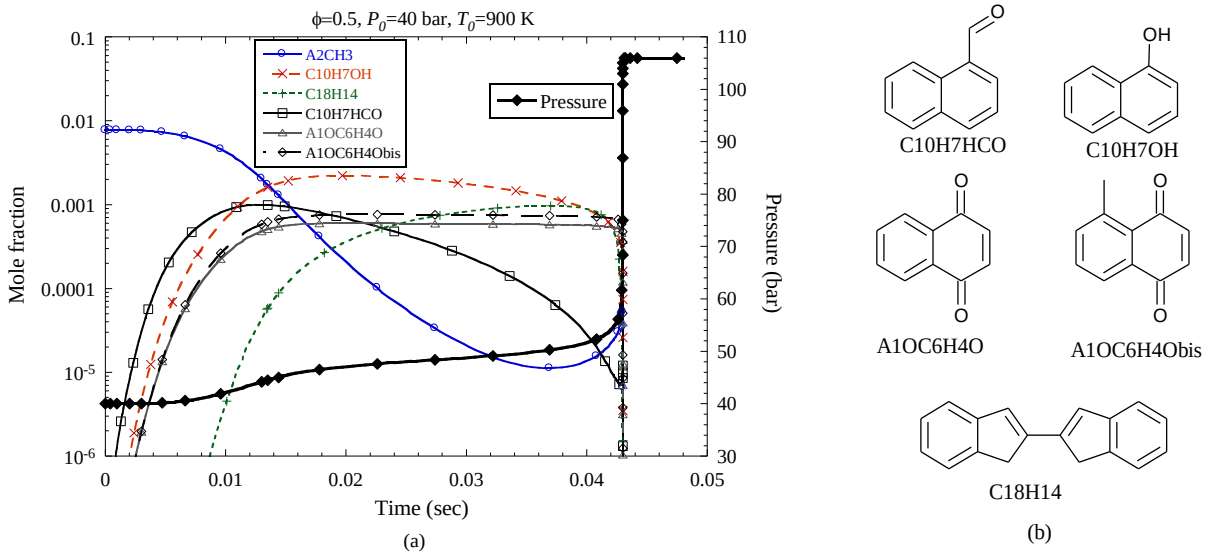

Figure 4.8 (a) Plot showing the evolution profiles of pressure and intermediate species predicted by the model of Wang et al. [48]. (b) Chemical structures of the intermediate species. Initial conditions are P_0=40 bar and T_0=900 K.

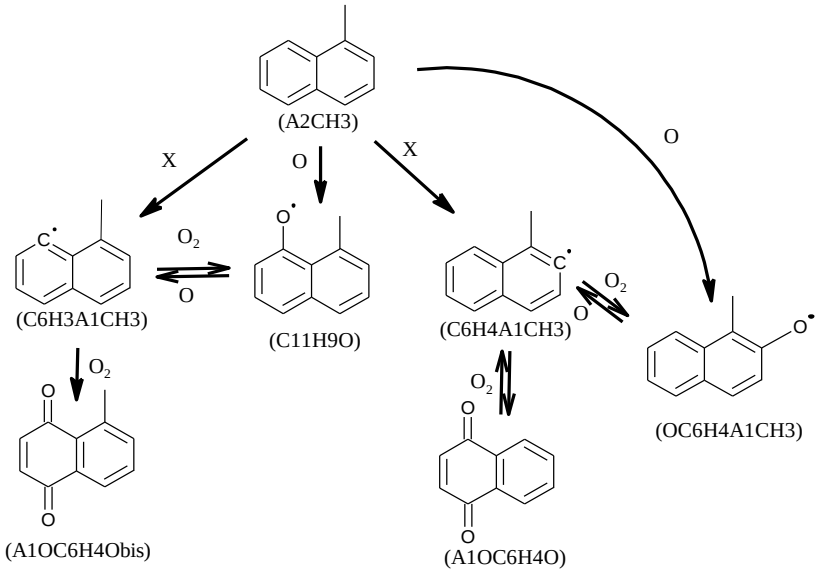

Figure 4.9 Reaction scheme showing the reactions channels leading to the formation of A1OC6H4Obis and A1OC6H4O in the model of Wang et al. [48]. "X" represents H, O, and OH.

Further analysis was conducted to identify the reactions pathways leading to the production and consumption of the intermediates species. Reaction path analysis showed that A1OC6H4Obis and A1OC6H4O are formed via the following two reactions of the parent fuel radicals.

$C6H3A1CH3 + O_2 = A1OC6H4Obis + H$ (R1)

$C6H4A1CH3 + O_2 = A1OC6H4O + CH_3$ (R2)

The reactions competing to the formation of A1OC6H4Obis and A1OC6H4O are as follows.

$C6H3A1CH3 + O_2 = C11H9O + O$ (R3)

$C6H4A1CH3 + O_2 = OC6H4A1CH3 + O$ (R4)

Figure 4.9 summaries the reaction channels of (R1)–(R4). Interestingly, (R3) and (R4) are also observed to proceed in the reverse direction, resulting in the fuel radicals of C6H3A1CH3 and C6H4A1CH3 that are predominantly consumed by (R1) and (R2). Moreover, (R3) and (R4) written in the reverse direction are the association reactions of two radicals leading to the formation of a stable species (O_2 in this case) and a radical. However, reactions of such nature are not expected to proceed in the reverse direction. One possible scenario for such reactions to proceed in the reverse direction is when the equilibrium constants are inaccurate due to the issues with the thermodynamic properties of the species involved. As such, the thermodynamic properties of the species involved in the reactions of (R1)–(R4) were examined. Recent quantum chemistry studies have shown that the energetics of the analogous reactions of toluene, benzene, and 1-MN derived radical species are nearly identical [51,52]. Therefore, the heats of reaction for the 1-MN related reactions were compared with those from the benzene and toluene sub-mechanisms present in the model of Wang et al. [48]. The choice for comparing with the reactions of benzene and toluene is because the associated chemical kinetics have been long studied and are considered to be well developed.

In the following analysis, the heats of reaction (ΔH_{rxn}) for (R1)–(R4) are examined. First, the heats of reaction of (R5) and (R6), which involve H abstraction from 1-MN (A_2CH3) leading to the formation of C6H3A1CH3, C6H4A1CH3, and hydrogen molecule (H_2) are compared.

$A2CH3 + H = C6H3A1CH3 + H_2$ (R5) $\Delta H_{rxn} = -1.8$ kcal/mole

$A2CH3 + H = C6H4A1CH3 + H_2$ (R6) $\Delta H_{rxn} = -1.8$ kcal/mole

The ΔH_{rxn} values of (R5) and (R6) are the same as they are analogous reactions that involve H abstraction from the benzene ring. Second, the heats of reactions for the H abstraction reactions from benzene (C6H6) and toluene (C6H5CH3) are as follows.

$C6H6 + H = C6H5 + H_2$ (R7) $\Delta H_{rxn} = 6.67$ kcal/mole

$C6H5CH3 + H = C6H4CH3 + H_2$ (R8) $\Delta H_{rxn} = 6.67$ kcal/mole

Based on analogy, it is expected that the heats of reactions for (R5)–(R8) should be similar. However, the ΔH_{rxn} comparison for (R5)–(R6) and (R7)–(R8) shows that they differ by about 8.5 kcal/mole. Further checks of the heats of reaction for the analogous reaction pairs (R1, R9) and (R2, R10) also exhibit significant differences, as shown below.

$C6H3A1CH3 + O_2 = A1OC6H4Obis + H$ (R1) $\Delta H_{rxn} = -86.00$ kcal/mole

$C6H5 + O_2 = OC6H4O + H$ (R9) $\Delta H_{rxn} = -51.32$ kcal/mole

$C6H4A1CH3 + O_2 = A1OC6H4O + CH_3$ (R2) $\Delta H_{rxn} = -103.82$ kcal/mole

$C6H4CH3 + O_2 = OC6H4O + CH_3$ (R10) $\Delta H_{rxn} = -61.25$ kcal/mole

The difference in ΔH_{rxn} for (R1) and (R9) is 34.68 kcal/mole, while the ΔH_{rxn} values of (R2) and (R10) differ by 42.57 kcal/mole. Such large differences are startling. Upon further checks on the thermodynamic properties of A1OC6H4Obis ($C_{11}H_8O_2$) and A1OC6H4O ($C_{10}H_6O_2$) in the model of Wang et al. [48], it was found that both species are assigned to have the same heat of formation as -61.06 kcal/mole. Using RMG [53], the heats of formation of the A1OC6H4Obis ($C_{11}H_8O_2$)

and A1OC6H4O ($C_{10}H_6O_2$) are estimated to be -40.57 and -24.52 kcal/mole, respectively. From these checks, we are suspicious that the thermodynamic properties of some of the species in the model of Wang et al. [48] might have errors. The errors in the thermodynamic properties might be affecting the equilibrium constants and the rates of the reverse reactions, thereby leading to the strange behavior observed in Fig. 4.7.

4.4.1.2 Simulations with Narayanaswamy et al. Model

The performance of the model of Narayanaswamy et al. [50] in predicting the ignition delays of 1-MN is also shown in Fig. 4.6. The model of Narayanaswamy et al. [50], like that of Wang et al. [48], appears to be more reactive than experiments at lower end of the compressed temperatures investigated in the current study. In addition, the model of Narayanaswamy et al. [50] is seen to predict the ignition delays at the stoichiometric (ϕ=1.0) condition to better accuracy than at the fuel lean (ϕ=0.5) and fuel rich (ϕ=1.5) conditions. It is further noticed that the difference between experimental and simulated ignition delays decreases gradually with increasing temperature up to a compressed temperature where a crossover in reactivity is observed. Beyond the crossover point, the model of Narayanaswamy et al. [50] becomes less reactive than the current RCM experiments. Comparison of the model of Narayanaswamy et al. [50] against the shock tube data of Wang et al. [48] shown in Fig .4.10 also demonstrates that this model is consistently less reactive than the high temperature experiments. Therefore, the differences in reactivity between the RCM experiments and the model predictions at higher compressed temperatures accessed in the current study are consistent with that shown in Fig. 4.10. Furthermore, the overall performance of the model of Narayanaswamy et al. [50] indicates that this model does not accurately predict the global activation energy, and hence model refinements are needed.

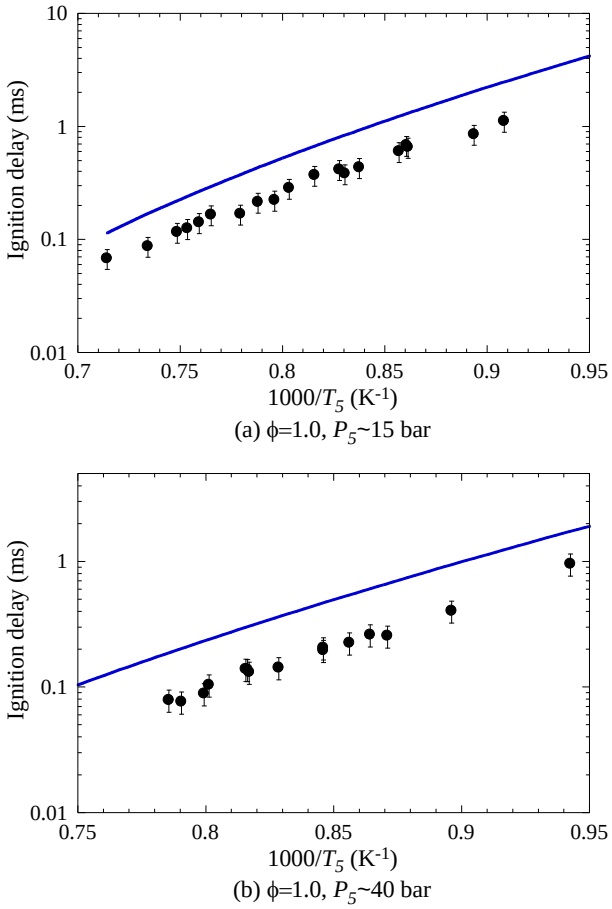

Figure 4.10 Plot showing the performance of the model of Narayanaswamy et al. [50] at the conditions investigated by Wang et al. [48].

The pressure traces from experiments and simulations compared in Fig. 4.5 shows that the model of Narayanaswamy et al. [50] also exhibits a strong pre-ignition heat release for the fuel lean condition while such a strong pre-ignition heat release is not displayed at the stoichiometric condition. Nevertheless, the pressure history simulated using the model of Narayanaswamy et al. [50] is not as peculiar as seen in that predicted by the model of Wang et al. [48]. Based on the comparative results of Figs. 4.6 and 4.7, it is clear that the model of Narayanaswamy et al. [50] performs better than that of Wang et al. [48] in predicting the autoignition behavior of 1-MN.

Hence, the subsequent reaction path analyses and brute force sensitivity analyses were conducted using the model of Narayanaswamy et al. [50].

4.4.2 Reaction Path Analysis

Reaction path analyses were conducted to study the oxidation pathways of 1-MN based on the model of Narayanaswamy et al. [50]. Using a constant volume, adiabatic simulation for the ϕ=0.5 mixture with initial conditions of 40 bar and 870 K, Fig. 4.11 shows the important oxidation pathways of 1-MN described by the model. This analysis was conducted at the time instant corresponding to the conversion of 50% 1-MN (A2CH3).

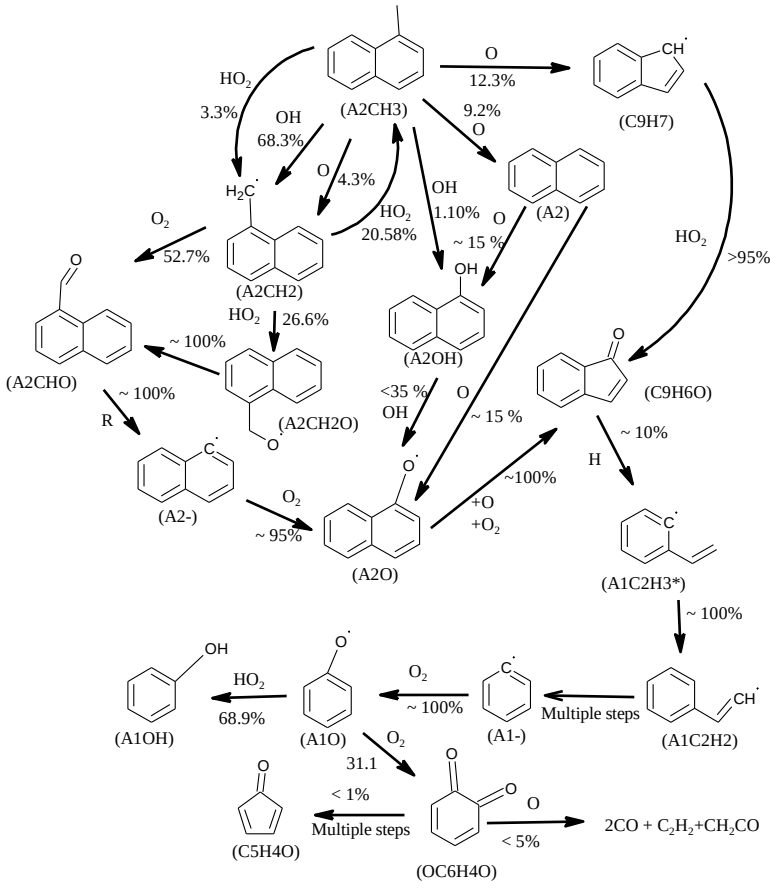

Figure 4.11 Reaction path analysis conducted for equivalence ratio of ϕ=0.5 in air at 50% conversion of 1-MN starting at initial conditions of 40 bar and 870 K. The chemical formulae of the species are given in parentheses. “R” represents H, O, OH, and HO2.

It is seen from Fig. 4.11 that 1-MN is predominantly consumed by oxygen atom (O), hydroperoxyl radical (HO_2), and hydroxyl radical (OH). Oxygen atom primarily attacks the carbon atoms of the benzene ring via (R11) and (R12), contributing 9.2% and 12.3% towards the consumption of 1-MN, respectively.

1-MN + O = A2 + CO + 2H (R11)

1-MN + O = C9H7 + CH_3 + CO (R12)

(R11) and (R12) are lumped reaction schemes which start with the replacement of H atom with O atom leading to the formation of methyl substituted naphthoxy radicals. The methyl substituted naphthoxy radicals undergo several dissociation reactions leading to the formation of naphthalene and indenyl radical along with methyl radical, carbon monoxide, and H atom. The lumped reaction schemes of (R11) and (R12) have been described in Narayanaswamy et al. [50].

The most important consumption channel of 1-MN is its reaction with OH that leads to the production of 1-naphthylmethyl (A2CH2) radical. This H abstraction from the methyl site contributes to about 68.3% of the consumption flux of 1-MN. The A2CH2 radical formed is consumed by reactions with oxygen molecule (O_2) and HO_2 radical. About 52.7% of the A2CH2 reacts with O_2 via (R13), in which A2CH2 is converted to 1-naphthaldehyde (A2CHO) and OH.

A2CH2 + O_2 = A2CHO + OH (R13)

This reaction acts a chain branching reaction and thus accelerates the ignition of 1-MN.

The other important consumption channel of A2CH2 is its reaction with HO_2. Flux analysis showed two possible reactions of A2CH2 with HO_2. In the first reaction channel, (R14), A2CH2 reacts with HO_2 leading to the formation of 1-MN and O_2, with about 20.58% of A2CH2 being consumed by this channel.

A2CH3 + O_2 = A2CH2 + HO_2 (R14)

Although this reaction in the current model is written as an initiation reaction with O_2, which produces A2CH2 and HO_2, the flux analysis showed that this reaction proceeds in the reverse direction consuming HO_2 and acts as a chain terminating reaction. The second important consumption channel of A2CH2 with HO_2 is the association reaction (R15), which leads to the formation of 1-methylnapthoxyl radical (A2CH2O) and OH radical, accounting for about 26.6% of A2CH2 consumption.

$A2CH2 + HO_2 = A2CH2O + OH$ (R15)

A2CH2O produced from (R15) undergoes the decomposition reaction, (R16), leading to A2CHO and H radical.

$A2CH2O = A2CHO + H$ (R16)

Rate of production analysis showed that (R16) is the most important source of production of H in the system.

The combination of (R15) and (R16) consumes HO_2 radical and produces OH and H radicals in return, thus acting as a chain branching sequence. A2CHO produced from the consumption of A2CH2O is consumed by the abstraction reactions of the weak benzaldehydic hydrogen leading to the formation of naphthyl radical (A2-) and carbon monoxide (CO).

$A2CHO + R = A2- + CO + RH$ (R17) R=OH, H, O, HO_2

The naphthyl radical (A2-) produced from the abstraction reactions of A2CHO is consumed by reactions with O_2 through (R18) and (R19).

$A2- + O_2 = C9H6O + CO + H$ (R18)

$A2- + O_2 = A2O + O$ (R19)

R18 is a minor consumption channel of A2- radical leading to the formation of indenone (C9H6O), CO, and H radical, while R19 consumes more than 95% of the naphthyl radical in the system.

(R19) results in the formation of naphthoxy (A2O) and O radicals. Flux analysis also showed that (R19) is the major source of O radical in the system contributing to about 93% of the total production of O radical. Further, naphthoxy radical (A2O) produced from (R19) is consumed by reactions with O and O_2 via (R20) and (R21), respectively.

A2O + O = C9H6O + CO + H (R20)

A2O + O_2 = C9H6O + CO + OH (R21)

Both reactions convert A2O to indenone (C9H6O), with (R20) and (R21) consuming about 58.5% and 41% of A2O, respectively. Another important channel for the production of indenone is (R22), involving HO_2 radical and indenyl radical (C9H7) produced from (R12).

C9H7 + HO_2 = C9H6O + H_2O (R22)

It was found that 1-MN is primarily (>70%) converted to indenone (C9H6O). Flux analysis also showed that only about 10% of the indenone produced from (R20)–(R22) is slowly consumed by the reaction with H atom leading to the formation of 1-vinyl-2-phenyl radical (A1C2H3*), as shown by (R23).

C9H6O + H = A1C2H3* + CO (R23)

Through (R24), A1C2H3* quickly isomerizes to phenyl vinyl radical (A1C2H2), which is quickly consumed by the reactions with O_2 via (R25)–(R27).

A1C2H3* = A1C2H2 (R24)

A1C2H2 + O_2 = A1CH2 + CO + O (R25)

A1C2H2 + O_2 = A1CHO + HCO (R26)

A1C2H2 + O_2 = A1C2H + HO_2 (R27)

Benzyl radical (A1CH2) formed from (R25) is then consumed by the reactions with O_2 and HO_2 which are analogous to (R13) and (R15), leading to the production of benzaldehyde (A1CHO).

Benzaldehyde is consumed by the reactions analogous to the reactions of 1-naphthaldehyde (A2CHO) converting A1CHO to phenyl radical (A1-). Phenyl radical is eventually converted to phenol (A1OH) and benzoquinone (OC6H4O), both of which are stable and are consumed at the hot ignition.

4.4.3 Brute Force Sensitivity Analyses

The brute force sensitivity coefficients were computed for 450 reactions in the model of Narayanaswamy et al. [50]. Specifically, the reactions whose sensitivity coefficients were computed include the total aromatic chemistry described in the model, and the sensitivity coefficients of the C_0–C_4 reactions were not computed.

The first set of brute force sensitivity analyses was conducted to study the effect of equivalence ratio at initial conditions of P_0=40 bar and T_0=870 K. As demonstrated earlier, the simulated ignition delays using the base model appear to match better at the stoichiometric condition of ϕ=1.0 than at the fuel lean condition of ϕ=0.5. This analysis could help in identifying the reactions whose effects on ignition delay change with change in equivalence ratio. Figure 4.12 shows and compares the sensitivity coefficients at two different equivalence ratios, for the top 5 reactions that promote ignition and the top 5 reactions that retard ignition. The sensitivity coefficients of the reactions of 1-naphthylmethyl (A2CH2) radical with O_2 and HO_2, (R13) and (R15), respectively, are negative as these reactions are chain branching in nature and hence accelerate the ignition event. The H-abstraction reaction from 1-MN (A2CH3) by HO_2 also exhibits a negative sensitivity coefficient as this reaction results in the buildup of hydrogen peroxide (H_2O_2) which is known to control ignition at low temperatures. It is noted that the reactions of 1-napththoxy radical (A2O) with O and O_2, (R20) and (R21), respectively, exhibit opposite sensitivity coefficients due to the contrasting nature of the two competing reactions.

Reaction of A2O with O_2 would produce OH radical at expense of O_2, while the reaction of A2O with O radical produces an H atom. H atom at the current temperature of 870 K gets converted to HO_2 radical, which is less reactive than OH radical. This difference in reactivities of the resulting OH and HO_2 is the reason why the reactions of A2O with O_2 and O exhibit contrasting sensitivity on ignition delay. In addition, the chain initiation reaction between 1-MN (A2CH3) and O_2 leading to the formation of 1-naphthylmethyl (A2CH2) radical and HO_2 radical retards ignition, because this reaction, as discussed earlier, proceeds in the reverse direction scavenging HO_2 radical which otherwise can participate in (R15) that is chain branching in nature. The substitution reaction of OH with 1-MN leading to the formation of 1-napththanol (A2OH) and CH_3 exhibits a positive sensitivity coefficient as Fig. 4.11 shows that this reaction competes with the reaction of OH with 1-MN leading to the formation of A2CH2, scavenges OH radical, and produces A2OH which is less reactive.

Furthermore, Fig. 4.12 shows that the sensitivity coefficients of most of the reactions do not change significantly with equivalence ratio. One exception is the reaction between indenone (C9H6O) and H, (R23), leading to the formation of 1-vinyl-2-phenyl (A1C2H3*) radical and CO. Since the sensitivity coefficient of (R23) is negative, reducing the rate of this reaction could help in slowing down the reactivity of the base model. A computational experiment was then conducted by reducing the reaction rate of (R23) by a factor of two to illustrate how the pressure trace is affected. Figure 4.13 shows the comparison of the pressure traces obtained from simulations using the base and modified models. Reducing the reaction rate of (R23) is seen to cause the pressure profile to exhibit a two-stage like behavior, thereby indicating that reducing the rate of (R23) might not be an appropriate way to improve the base model. The reason for (R23) to lead to such a distinct effect on pressure history is that in the model of Narayanaswamy et al. [50] indenone acts a

bottleneck for reactivity. As discussed in Section 4.4.2, indenone is a relatively stable, nonreactive species limiting the breakdown of the parent fuel (1-MN) into small fragments and thus hindering ignition.

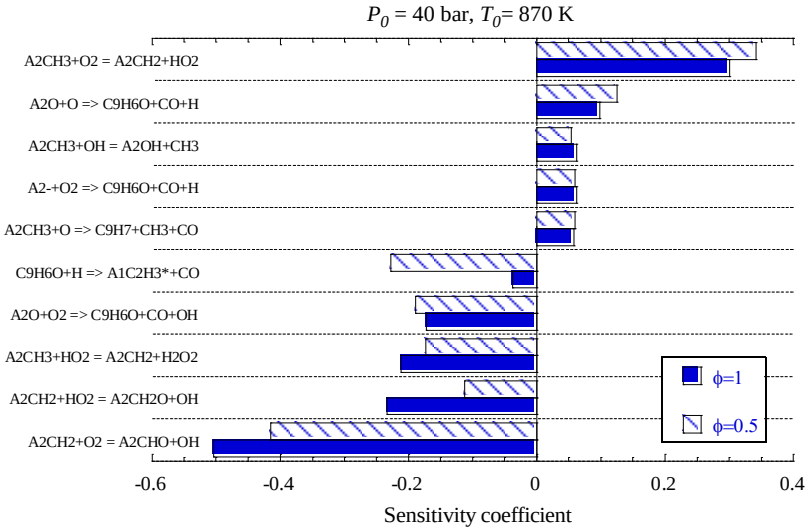

Figure 4.12 Comparison of brute force sensitivity coefficients of selected reactions at varying equivalence ratios for initial conditions of 40 bar and 870 K.

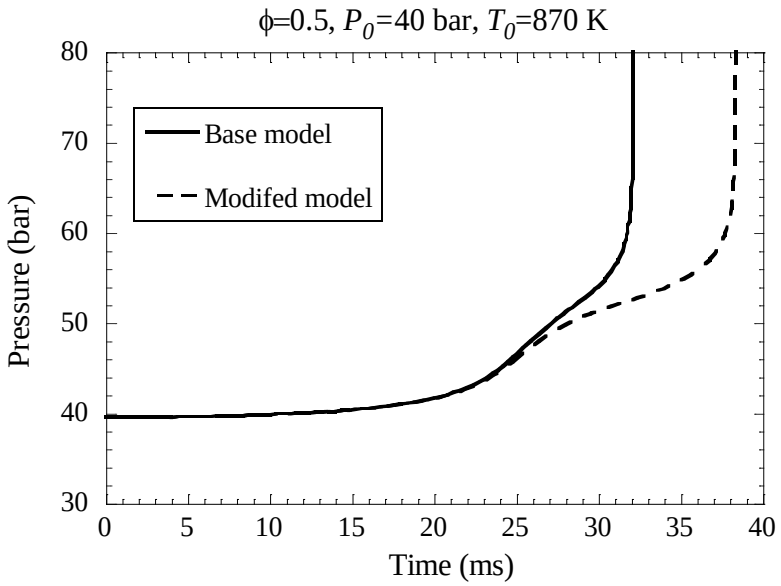

Figure 4.13 Plot showing the effect of decreasing the rate of the reaction C9H6O + H = A1C2H3* + CO by a factor of two on pressure evolution.

The second set of brute force sensitivity analyses was conducted to study the change in sensitive reactions with change in initial temperature, for stoichiometric mixtures with an initial pressure of 40 bar. The sensitivity coefficients were computed and compared at initial temperatures of 870 K and 1200 K, as they are the typical conditions investigated in the current RCM experiments and the shock tube study of Wang et al. [48], respectively. This analysis aims to identify if there exists any reaction(s) whose effect on ignition delay changes characteristically from promoting to retarding or vice-versa upon change in temperature. The comparison of sensitivity coefficients computed at the two initial temperatures for those selected, important reactions is shown in Fig. 4.14.

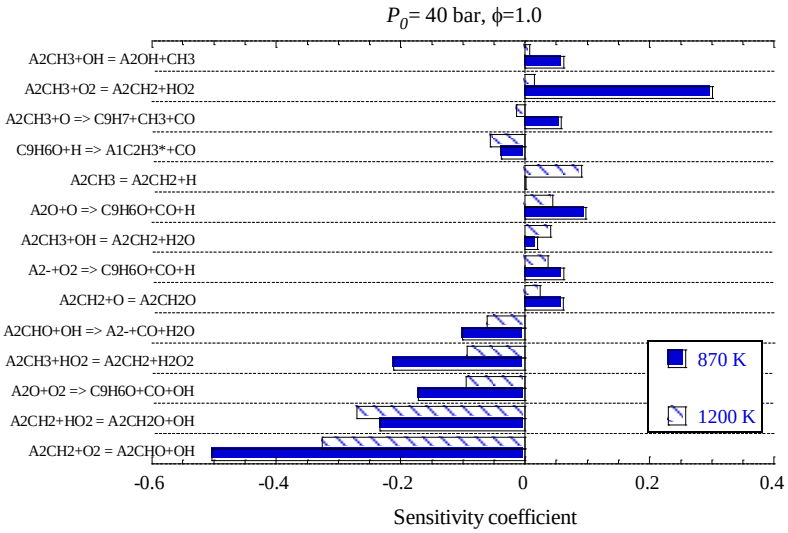

Figure 4.14 Comparison of brute force sensitivity coefficients of selected reactions for stoichiometric 1-MN/air mixtures with initial pressure of 40 bar at varying initial temperatures.

From Fig. 4.14, the only reaction whose sensitivity coefficients change sign with different initial temperatures is the reaction between 1-MN and O radical, (R12). This reaction is a lumped reaction scheme, which has earlier been described in Section 4.4.2. The reaction rate of this lumped scheme used in the base model is analogous to the rate of the reaction between benzene and O

radical leading to the formation of phenoxy and H radicals that was taken from the benzene sub-model of Blanquart et al. [54]. Taatjes et al. [55] have recently conducted a study focusing on the reaction channels of benzene with O radical and proposed the rates of all the possible reaction channels. Figure 4.15 shows the comparison of the reaction rates used in the model of Narayanaswamy et al. [50] and the high pressure limit rate taken from Taatjes et al. [55]. It is seen that the reaction rate proposed by Taatjes et al. [55] is about a factor of 5 lower than the rate used in the model of Narayanaswamy et al. [50] at 830 K and the difference in rates drops to a factor of two at 1200 K. As this particular reaction exhibits a positive (negative) sensitivity coefficient at 870 K (1200 K), using the rate from Taatjes et al. [55] would make the model relatively more (less) reactive at low (high) temperatures and hence may not be a solution to resolve the current discrepancy between experiments and simulations.

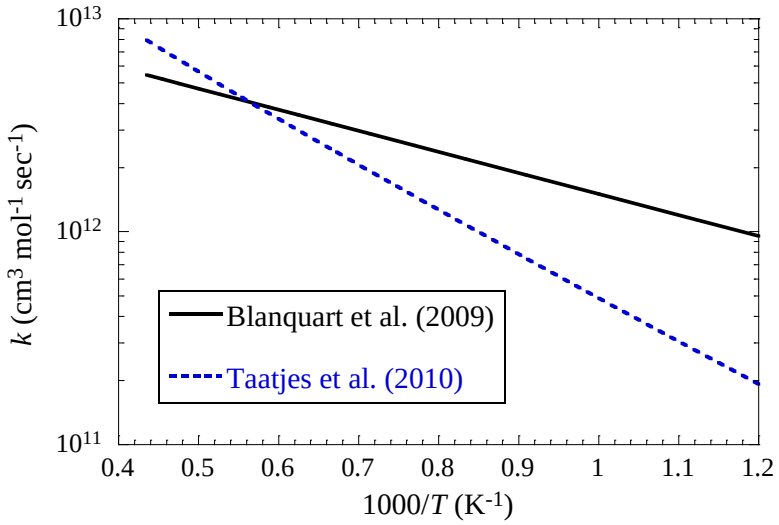

Figure 4.15 Plot showing the rate comparison for the reaction of C6H6+O = C6H5O + H taken from Blanquart et al. [54] and Taatjes et al. [55].

Unfortunately, the sensitivity analyses conducted here were not able to identify the reactions whose rates can be modified to improve the performance of the base model. One possible reason

for the differences observed in the experimental and simulated ignition delays can be due to the absence of some important reaction paths in the current model.

4.4.4 Possible Missing Reaction Paths

The literature studies of [52,55-58] were surveyed to help identify some of the possible missing reaction pathways. In the study of Taatjes et al. [55] on the addition reaction channels of benzene (C6H6) and O radical, three major reaction pathways, R28–R30, were noted.

$$C_6H_6 + O = C_6H_5O + H \quad \text{(R28)}$$

$$C_6H_6 + O = C_5H_6 + CO \quad \text{(R29)}$$

$$C_6H_6 + O = C_6H_5OH \quad \text{(R30)}$$

R28–R30 lead to the formation of phenoxy (C6H5O), cyclopentadienyl radical (C5H6), and phenol (C6H5OH). Ngyuen et al. [56] also stated that (R28) and (R30) are the important channels for the addition reaction system of C6H6 + O. Both the studies of Taatjes et al. [55] and Ngyuen et al. [56] suggested that R30 is important at low temperatures. The model of Narayanaswamy et al. [50] included the lumped reaction scheme R12, which is analogous to R28 but does not include the reactions analogous to (R29) and (R30). One reason that Narayanaswamy et al. [50] did not add the reactions analogous to (R30) is because Shaddix et al. [44,45] did not observe any methyl substituted naphthanols in their flow reactor experiments at 1170 K. As stated by Narayanaswamy et al. [50], there could be a possibility that products formed from the reactions analogous to (R30) could be short lived species at conditions relevant to the experiments of Shaddix et al. [44,45]. However, for the low-to-intermediate conditions investigated in the current RCM study, the methyl substituted naphthanols might not be short lived species and potentially could also act as a radical sink. Therefore, it might be necessary to include the reaction channels analogous to (R30).

In addition, the H-abstraction reactions from the aromatic ring were not included in the model of Narayanaswamy et al. [50]. The different types of H-abstraction reactions are shown in Fig. 4.16, using the 1-MN + OH system as an example. As shown in Fig. 4.12 for T_0=870 K, the reactions of 1-MN and OH account for the major consumption of 1-MN, while the H-abstraction from the methyl site by OH radical is the only type of H-abstraction reactions modelled in the base model. In [50], the rate for H-abstraction by OH radical from the methyl site was taken from Seta et al. [57]. The abstraction rates from Seta et al. [57] suggested that at a temperature of 870 K, about 68.6% of the flux of the H-abstraction reactions is from the abstraction from the methyl site, while 31.4% of the flux is through the H abstractions from the aromatic ring. As such, the inclusion of the H abstraction from the aromatic ring is expected to reduce the amount of 1-naphthylmethyl (A2CH2) radical produced from 1-MN. The sensitivity analyses and reaction path analyses conducted in the current study showed that the reactions of 1-naphthylmethyl radical with O_2 and HO_2, (R13) and (R15), respectively, are the two major reactions that control the reactivity of 1-MN. In addition, the subsequent reactions for the species formed from the H abstraction from the aromatic ring are not chain branching at low temperatures. Hence, the inclusion of all possible H-abstraction channels shown in Fig. 4.16 can potentially lower the reactivity of 1-MN at low temperatures.

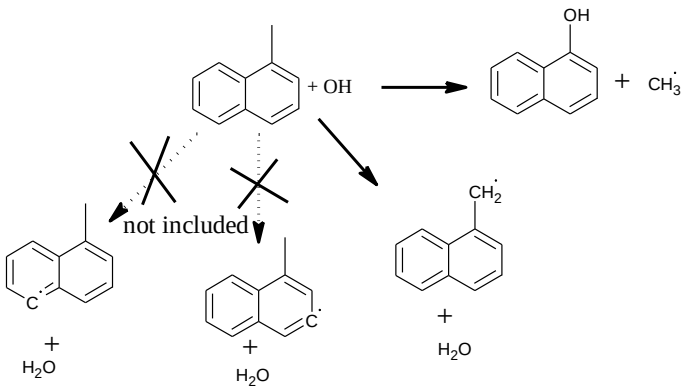

Figure 4.16 Important reactions of 1-MN + OH system. Reactions with broken arrows indicate the pathways which are missing in the model of Narayanaswamy et al. [50].

Another important reaction pathway that is missing in the base model is a channel unique to the reactions between A2CH2 and O_2 recently observed by Oguchi and Murakami [52], as shown in Fig. 4.17. Oguchi and Murakami [52] found that the reactions between A2CH2 and O_2 could lead to the formation of cyc-NaphCH2O (see Fig.4.17 for its chemical structure) in addition to the channels leading to the formation of 1-naphthadehyde (A2CHO) + OH and 1-naphthoxy (A2O) + formaldehyde (CH_2O). It is noted that the pathway leading to A2CHO + OH accounts for the major consumption of A2CH2 in Fig. 4.11, while the channel forming A2O + CH_2O is insignificant therein. Further, since the channels leading to the formation of 1-naphthadehyde and 1-naphthoxy radicals are identical to those observed in the benzyl + O_2 system [58], their reaction rates in the base model were taken from [58]. Oguchi and Murakami [52] estimated that at 10 atm and in the temperature range of 200−1600 K, the branching ratio of the channel leading to the formation of cyc-NaphCH2O is about 0.7 while the branching ratio leading to the formation of 1-naphthadehyde and 1-naphthoxy is around 0.15, indicating that the missing channel could be dominant. As the reaction between A2CH2 and O_2 leading to A2CHO + OH was found to the most sensitive reaction in the present brute force sensitivity results, addition of the channel leading to the formation of cyc-NaphCH2O might be important.

Finally, the other missing channel is the addition reaction between A2CH2 and HO_2 radical leading to the formation of 1-naphthylmethyl hydroperoxide (A2CH2OOH), in addition to that leading to A2CH2O + OH, (R15). This reaction channel is expected to be important at temperatures below 700 K and compete with (R15) based on the work of da Silva and Bozzelli [59]. Furthermore, da Silva and Bozzelli [59] noticed that the reaction rate of (R15) shows a complex temperature dependence and proposed two sets of rate parameters for the temperature ranges of 300−800 K and 800−2000 K, respectively. However, the model of Narayanaswamy et

al. [50] only used the rate corresponding to the temperature range of 800−2000 K. As a consequence, the model of Narayanaswamy et al. [50] overestimated the reaction rate of (R15) by factors of 13 and 4 at 600 K and 700 K, respectively.

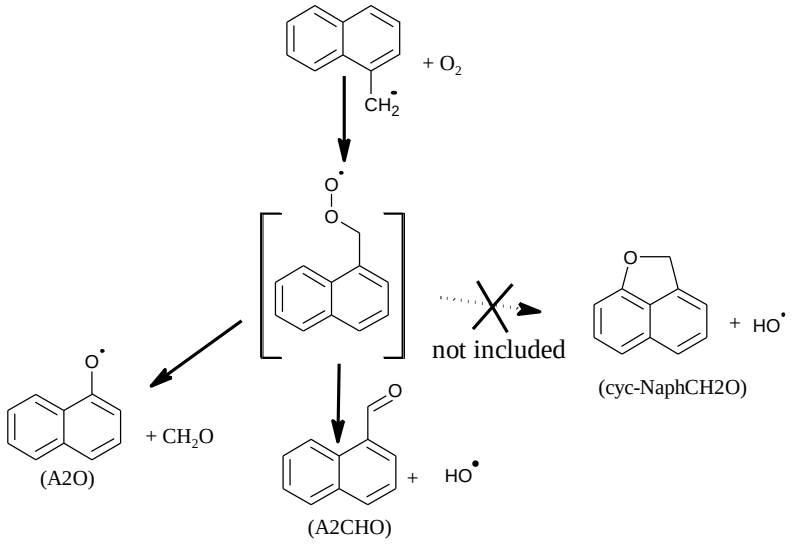

Figure 4.17 Important reactions of 1-naphthylmethyl (A2CH2) + O_2 system taken from Oguchi and Murakami [52]. Reactions with broken arrows indicate the pathways which are missing in the model of Narayanaswamy et al. [50].

4.5. Conclusions

Autoignition of 1-MN has been studied at low-to-intermediate temperatures and elevated pressures using an RCM. The RCM experiments were conducted to demonstrate the effects of temperature, equivalence ratio, and pressure on ignition delays. The ignition delays measured in the current study were observed to complement well with the literature shock tube data at higher temperatures. For the conditions investigated here, the experimental pressure traces showed that 1-MN behaves like a single-stage ignition fuel and no strong pre-ignition heat release was observed. In addition, the experimental ignition delays were used to assess the performance of two latest chemical kinetic models of 1-MN. Of the two models, the model of Narayanaswamy et al. [50] appears to do a

better job in estimating the measured ignition delays and pressure histories. Since the pressure history predicted by the model of Wang et al. [48] exhibited a two-stage ignition like behavior which was not observed in the RCM experiments, an analysis was conducted to show that the thermodynamics properties of some of the intermediate species in the model need to be corrected. The ignition delays predicted by the model of Narayanaswamy et al. [50] exhibited significant differences at lower end of the compressed temperatures investigated in the current study, with discrepancies being about a factor of 1.5–2 lower than experimental values. Moreover, the model of Narayanaswamy et al. [50] did show a strong pre-ignition heat release at fuel lean conditions, which was not observed from the experimental pressure traces. Further chemical kinetic analyses were conducted to show that some of the important reaction channels are missing in the model of Narayanaswamy et al. [50]. The inclusion of these missing channels identified here could potentially improve the predictability of the 1-MN model.

Chapter 5 : Binary Blends

5.1. Introduction

Since the chemical kinetic models of surrogate fuels are typically assembled by merging the individual models of the constituent hydrocarbons, the ability of the surrogate models to capture the combustion characteristics of the target real fuels is reliant on the fidelity of the chemical kinetic models of the surrogate constituents. Besides accurately describing the combustion kinetics of the neat surrogate constituents, it is also necessary to capture the chemical kinetic interactions when the surrogate constituents are blended together. The objective of the current study is to investigate the ignition behaviors of various binary blends of the surrogate constituents relevant to diesel fuels.

The binary blends of present interest are the fuel mixtures of 1-methylnaphthalene and *iso*-cetane (2,2,4,4,6,8,8 heptamethylnonane), as well as 1-methylnaphthalene and *n*-dodecane, at varying blending ratios. The skeletal structures of the *n*-dodecane, *iso*-cetane, and 1-methylnaphthalene is shown in Fig. 5.1 . *n*-Dodecane, *iso*-cetane, and 1-methylnaphthalene have been chosen in this investigation as the respective representatives of *n*-alkanes, *iso*-alkanes, and aromatics, respectively, which constitute to the major compound classes in diesel fuels [42]. In addition, 1-methylnaphthalene and *iso*-cetane were chosen because they have been widely used in surrogate formulations [e.g., 9,10,23,42,60] and they are the reference fuels used for determining the cetane rating of a fuel. The choice of *n*-dodecane as the representative of *n*-alkanes, instead of *n*-cetane, is due to its relatively lower boiling point so that it is comparatively easier to handle in experiments. It is further noted that *n*-cetane and *n*-dodecane are homologous hydrocarbons, and hence they are expected to exhibit analogous oxidation chemistry and similar ignition characteristics.

A survey of the literature showed that while the chemical kinetics for the neat components of 1-methylnaphthalene [44-49], *iso*-cetane [61-64], and *n*-dodecane [65-74] have been studied experimentally to some detail, there are only very few studies on the binary blends involving these fuel components [48,75,76]. Wang et al. [48] studied the ignition of stoichiometric binary blends of *n*-decane/1-methylnaphthalene in air behind reflected shock waves at nominal pressures of 10 bar and 40 bar over a temperature range of 848−1349 K. Won et al. [75] measured the ignition delays of a stoichiometric *iso*-cetane/*n*-cetane blend (54.1/45.9 in molar %) at a nominal pressure of 20 atm over a temperature range of 685−1250 K. Agosta et al. [76] studied the oxidation of the blends of *iso*-cetane/*n*-dodecane (60/40 in molar %) and 1-methylnaphthalene/*n*-dodecane (49/51 in molar %) in a flow reactor at a pressure of 8 atm and a residence time of 120 ms over a temperature range of 600−900 K.

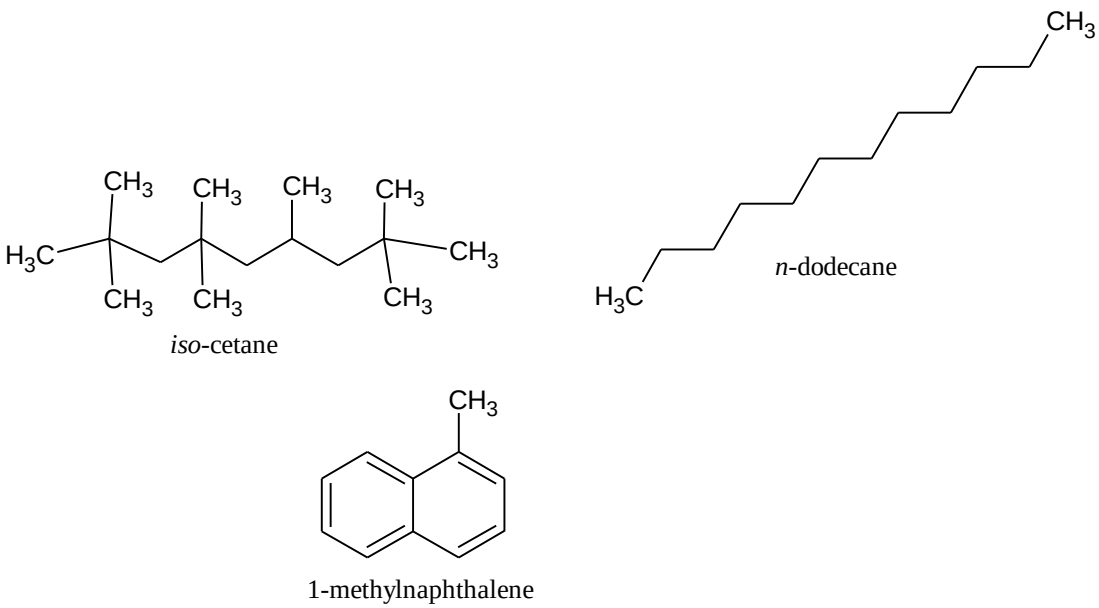

Figure 5.1 Skeletal structure of constituents of the binary blends.

Recognizing the need for more experimental studies on fuel blends, we have conducted elevated-pressure experiments using a rapid compression machine to investigate the autoignition characteristics of the binary blends of *n*-dodecane/1-methylnaphthalene and *iso*-cetane/1-

methylnaphthalene with varying blending ratios. Further details of the blend compositions, the experimental procedure, and the test conditions shall be specified and described in the next section. Later sections shall discuss the experimental data followed by the comparison with the simulated results using the chemical kinetic models available in the literature. Finally, the deficiencies of the literature models and the potential areas to refine them shall be identified and discussed.

5.2. Experimental Specifications

5.2.1 Test Mixtures

Tables 5.1 and 5.2 summarize the compositions of different fuel blend/O_2/N_2 mixtures and the molar % (X) of the components in the test mixtures investigated in the current study. From here on, *n*-dodecane, *iso*-cetane, and 1-methylnaphthalene shall be referred as *n*-C12, *i*-C16, and 1-MN, respectively. The oxidizer used here was the mixture of O_2 and N_2 in the molar proportion of O_2:N_2=1:3.76, while the stoichiometric condition was maintained for all test mixtures. Moreover, the values of "% *n*-C12 in the blend" and "% *i*-C16 in the blend" listed in Tables 5.1 and 5.2, respectively, correspond to the molar percentages of *n*-C12 and *i*-C16 in the respective binary fuel blends. Here, a wide range of varying proportions of the constituent hydrocarbons in the fuel blend was covered in order to investigate the response of the blend reactivity to the blending ratio. It is also noted from Tables 5.1 and 5.2 that the molar percentages of O_2 and N_2 in the test mixtures, X_{O2} and X_{N2}, remain largely unchanged as the equivalence ratio and the oxidizer composition were held fixed.

In addition, the derived cetane number (DCN) of each binary fuel blend is listed in Tables 5.1 and 5.2. The DCN values of the three pure components were taken from [77], while those of the fuel blends were calculated simply using a linear relationship on a liquid volume basis. It is seen from Tables 5.1 and 5.2 that a wide range of DCNs was also covered in this study.

Table 5.1: Compositions of test mixtures and DCN values of *n*-C12/1-MN blends.

$X_{n\text{-C12}}$ (%)	$X_{1\text{-MN}}$ (%)	X_{O2} (%)	X_{N2} (%)	% *n*-C12 in the blend	DCN
1.12	0.00	20.77	78.11	100	87.0
0.85	0.37	20.75	78.03	70	68.6
0.57	0.76	20.73	77.94	43	47.0
0.41	0.97	20.72	77.90	30	35.3
0.22	1.23	20.70	77.85	15	20.0
0.15	1.33	20.70	77.82	10	13.1
0.08	1.43	20.69	77.80	5	6.7
0.00	1.53	20.69	77.78	0	0

Table 5.2: Compositions of test mixtures and DCN values of *i*-C16/1-MN blends.

$X_{i\text{-C16}}$ (%)	$X_{1\text{-MN}}$ (%)	X_{O2} (%)	X_{N2} (%)	% *i*-C16 in the blend	DCN
0.85	0.00	20.83	78.32	100	15.1
0.72	0.24	20.81	78.23	75	12.9
0.55	0.55	20.78	78.12	50	10.0
0.32	0.96	20.74	77.98	25	2.7
0.00	1.53	20.69	77.78	0	0

5.2.2 Test Conditions

In the current RCM experiments, the test conditions covered the compressed pressures of P_C=15 bar and 30 bar, as well as the compressed temperatures of T_C=626−944 K. Furthermore, because of the relatively high-boiling-point fuel components investigated here, the mixing chamber, intake manifolds, and RCM were heated to a sufficiently high initial temperature to ensure that the partial pressures of the test fuel components were always less than their corresponding saturated vapor pressures at least by a factor of 1.5. In particular, an initial temperature of T_0=122 ^{o}C was used for experiments with the stoichiometric *n*-dodecane/air mixtures, while a preheat temperature of T_0=147 ^{o}C was used for all the other binary blends shown in Tables 5.1 and 5.2.

5.2.3 Mixture Preparation

The homogenous test mixtures are prepared according to the procedure described in Section 2.2.1. The *n*-dodecane (>99% purity), *iso*-cetane (98% purity), and 1-MN (95% purity) used in the current study were obtained from Sigma-Aldrich®.

5.3. Experimental Results

5.3.1 Experiments with Pure Components

Experiments were first conducted with the three neat hydrocarbon components investigated in the current study. The experiments with 1-MN were conducted at nominal compressed pressures of P_C=15 bar and 30 bar, while the experiments with *i*-C16 and *n*-C12 were limited to a compressed pressure of P_C=15 bar. At P_C=30 bar, the *i*-C16/air and *n*-C12/air mixtures resulted in ignition during the compression stroke for the temperature range tested. Figure 5.2 shows the total ignition delays of the three neat hydrocarbons from the current RCM experiments along with the literature data from shock tubes [47,48,61,65,78].The total ignition delay data from shock tubes were scaled to the current compressed pressure values using the pressure scaling factors suggested by the cited studies. From Figs. 5.2(a) and 5.2(b), it is seen that the current RCM measurements of 1-MN and *i*-C16 line up well with the ignition delays from shock tube experiments, indicating that the current lower temperature RCM data complement well with the higher temperature shock tube data. Figure 5.2(c) compares the measured ignition delays of *n*-C12 from the current RCM experiments and the shock tube experiments of Vasu et al. [65] conducted at pressures in the range of 18–27 atm and at temperatures higher than 722 K. Since the current ignition delay measurements of *n*-C12 were conducted at compressed temperatures in the range of 625–651 K, the shock tube ignition delay data of *n*-octane (*n*-C8) [78] are also included in Fig. 5.2(c) for comparison. At the overlapped temperatures, the current ignition delays of *n*-C12 are seen to be shorter than those of

n-C8. This could be due to the difference in chain length as an increase in chain length can shorten the ignition delays, in addition to some facility effects on ignition delay. In general, comparison of the ignition delays of *n*-C8 and *n*-C12 in Fig. 5.2(c) shows that the current RCM data compare well against the shock tube ignition delays. Nonetheless, further experiments with *n*-alkanes might be needed to understand the effects of chain length on autoignition characteristics, especially at low-to-intermediate temperatures.

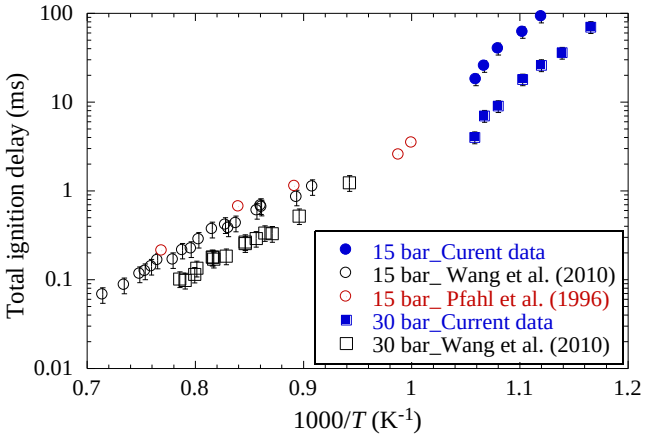

(a) 1-MN

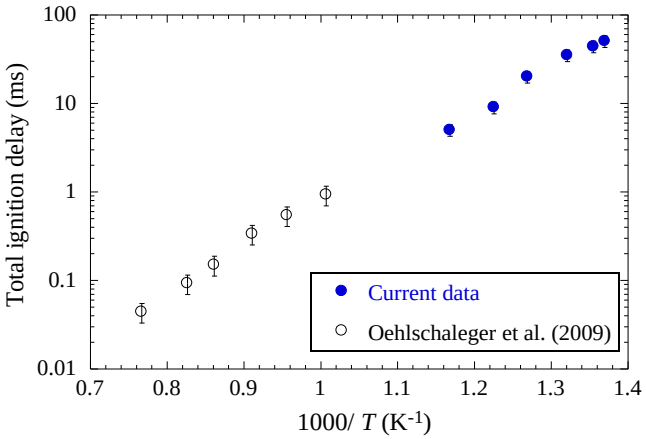

(b) *i*-C16, 15 bar

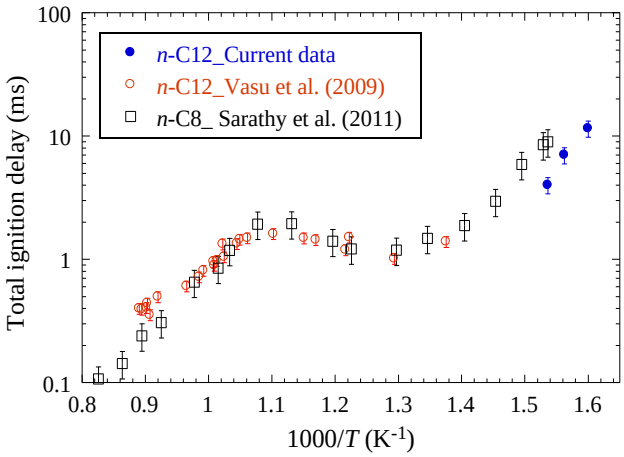

(c) *n*-C8 and *n*-C12, 15 bar

Figure 5.2 Comparison of ignition delays of (a) 1-MN, (b) *i*-C16, and (c) *n*-C8 and *n*-C12 from the current RCM experiments and the literature shock tube experiments [47,48,61,65,78].

5.3.2 Experiments with *n*-C12/1-MN Binary Blends

The ignition delay measurements of binary blends of *n*-C12/1-MN were conducted at a compressed pressure of P_C=15 bar over a wide compressed temperature range of T_C=655–936 K. At a nominal compressed temperature of T_C=669 K, Fig. 5.3(a) plots the experimental pressure traces at varying % *n*-C12 in the binary fuel blend. It can be seen from Fig. 5.3(a) that the pressure history shows a single stage like ignition behavior when the % *n*-C12 in the blend is 30% and higher. These blends exhibit single stage ignition as the radical pool developed is large enough to trigger hot ignition. For the blends containing 10% and 15% *n*-C12, two-stage ignition behaviors are observed in Fig. 5.3(a), with the pressure rise associated with the first stage of ignition being higher in the case of 15% *n*-C12 blend. A lower pressure rise from the first stage ignition, as in the case of the blend containing 10% *n*-C12, stretches the second stage of ignition, resulting in a pressure history with two distinct stages of ignition.

Figures 5.3(b) and 5.3(c) respectively summarize the total and first stage ignition delays of the different *n*-C12/1-MN blends deduced from the pressure traces using the definitions shown in Fig. 2.5. The ignition delay measurements shown in Figs. 5.3(b) and 5.3(c) exclude those data points exhibiting exothermicity during the compression stroke. The pressure histories taken from the nonreactive counterparts, by replacing O_2 with N_2 in the test mixtures, were used as references to identify the extent of exothermicity for each case. The ignition delays of the blends containing more than 10% *n*-C12 were limited to low temperatures, as further increase in compressed temperature resulted in exothermicity during the compression stroke. Figures 5.3(b) and 5.3(c) show that both the total ignition delays and the first stage ignition delays decrease with increasing amount of *n*-C12 in the blend.

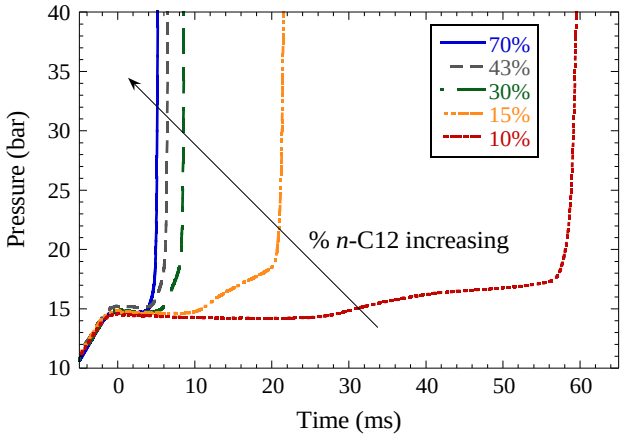

(a)

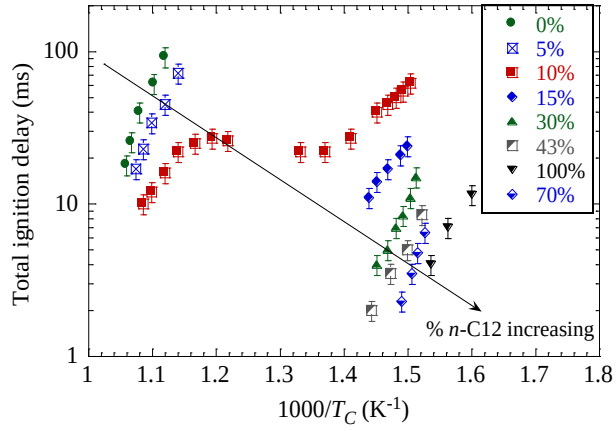

(b)

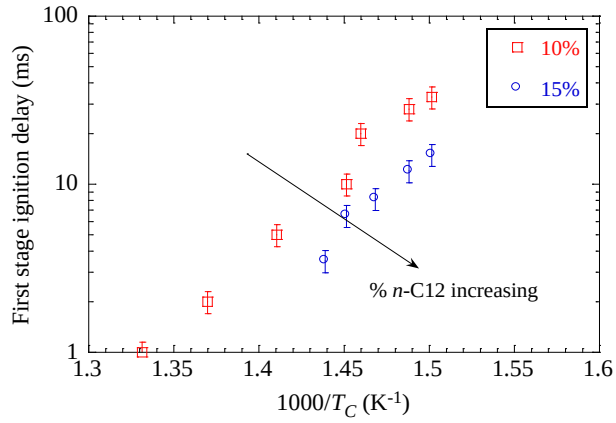

(c)

Figure 5.3 Plots showing (a) experimental pressure traces at compressed temperature of T_C=669±3 K, (b) total ignition delays, and (c) first stage ignition delays for *n*-C12/1-MN blends at varying blending ratios.

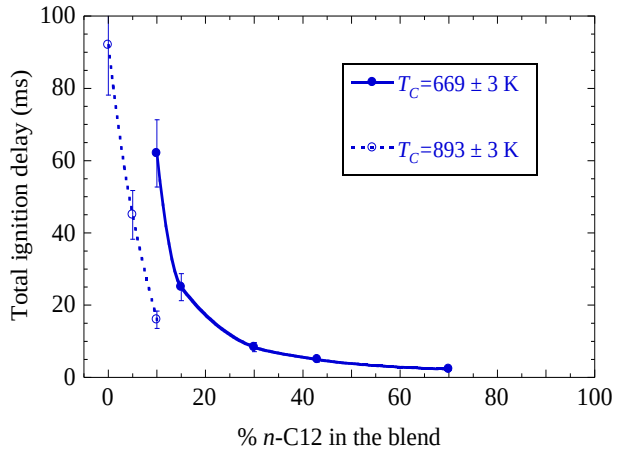

Figure 5.4 Plot showing the effect of % *n*-C12 in the *n*-C12/1-MN blends on total ignition delays at P_C=15 bar for two compressed temperatures of T_C~669 K and ~893 K.

To better understand the sensitivity of the total ignition delay variation with % *n*-C12 in the blend, the total ignition delays of the *n*-C12/1-MN blends at two different compressed temperatures are plotted and compared in Fig. 5.4. Figure 5.4 shows that the total ignition delay decreases nonlinearly with increasing % *n*-C12 in the blend. At T_C~893 K, the total ignition delays shown in Fig. 5.4 drop steeply upon small addition of *n*-C12 to the pure 1-MN case. Specifically, the total ignition delay decreases by a factor of about two when the % *n*-C12 in the blend increases from 0% to 5%. Further increase in % *n*-C12 from 5% to 10% shortens the total ignition delay by a factor of three. Figure 5.4 also illustrates the effect of % *n*-C12 in the blend on total ignition delay at a lower compressed temperature of T_C~669 K. It is seen that increasing % *n*-C12 in the blend continues to cause a steep drop in total ignition delays till the amount of *n*-C12 increases to 30%. Beyond that, namely increasing % *n*-C12 in the blends from 43% to 70%, there is no significant change in total ignition delay observed in Fig. 5.4. Similar nonlinear dependence of total ignition delay on the constituent amount of binary blends was also noticed by Wang et al. [48] in their shock tube experiments with binary blends of *n*-decane/1-MN. The total ignition delay results shown in Fig. 5.4 demonstrates that when two fuel components with distinct reactivities are

blended, small addition of the more reactive fuel (like *n*-C12 in the current case) to the less reactive fuel (like 1-MN) in excess amount could result in a strong change in the global reactivity of the blend. On the other hand, small addition of the less reactive fuel to the more reactive fuel of abundant presence may have weak or indistinguishable effect on the global reactivity of the blend.

5.3.3 Experiments with *i*-C16/1-MN Binary Blends

Figure 5.5 shows the ignition delay measurements of binary blends of *i*-C16/1-MN conducted at two compressed pressures of P_C=15 bar and 30 bar. Experiments at P_C=15 bar showed no two-stage like behavior. At P_C=30 bar, two-stage ignition behavior was observed with the equimolar (50/50) *i*-C16/1-MN blend in the compressed temperature range of T_C=704–740 K. The corresponding total and first stage ignition delays are shown in Figs. 5.5(b) and 5.5(c), respectively. Figures 5.5(a) and 5.5(b) also illustrates that an increase in % *i*-C16 in the blend generally increases the reactivity of the system.

At two sets of P_C and T_C, namely 15 bar/893 K and 30 bar/858 K, Fig. 5.6 examines the response of total ignition delay to the amount of *i*-C16 in the *i*-C16/1-MN blends. The total ignition delays at both the compressed conditions decrease monotonically with increasing % *i*-C16. However, in the regime of small *i*-C16 addition (< 20%), the total ignition delay decreases more gradually with an increase in % *i*-C16, unlike the steep drop observed in Fig. 5.4 for the *n*-C12/1-MN blends. Figure 5.7 further shows the comparison of changes in total ignition delays due to the additions of *n*-C12 and *i*-C16 to 1-MN at P_C=15 bar and T_C ~893 K, demonstrating that the addition of *n*-C12 has a stronger effect on reactivity. Since *n*-C12 is known to be more reactive than *i*-C16, the observed difference in the ignition promoting effect can be attributed to the relative reactivities of the addendums.

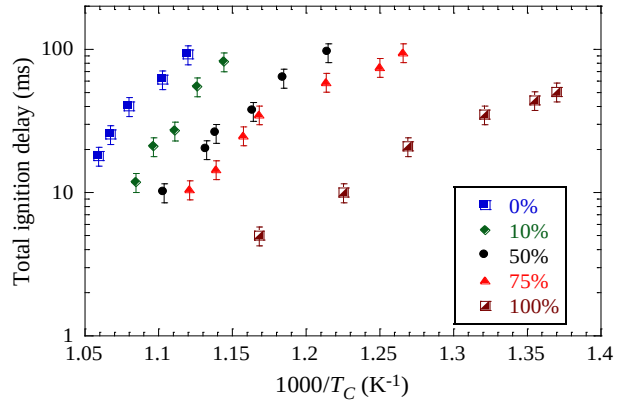

(a) P_C=15 bar

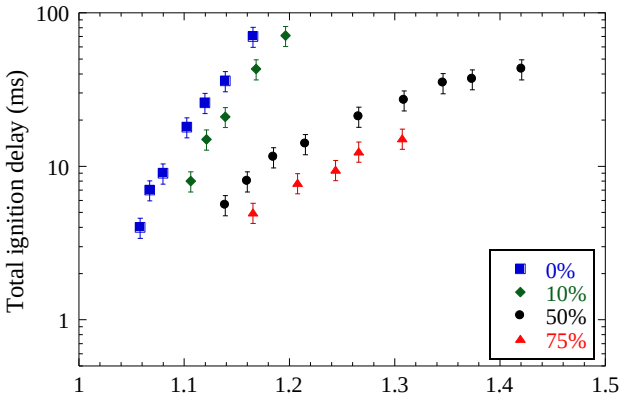

(b) P_C=30 bar

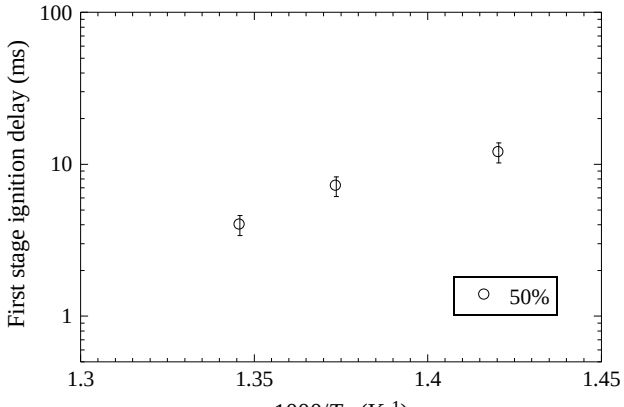

(c) P_C=30 bar

Figure 5.5 Arrhenius plots of ignition delays of binary blends of *i*-C16/1-MN. The legends in the figure represent the amount of *i*-C16 in the binary blend.

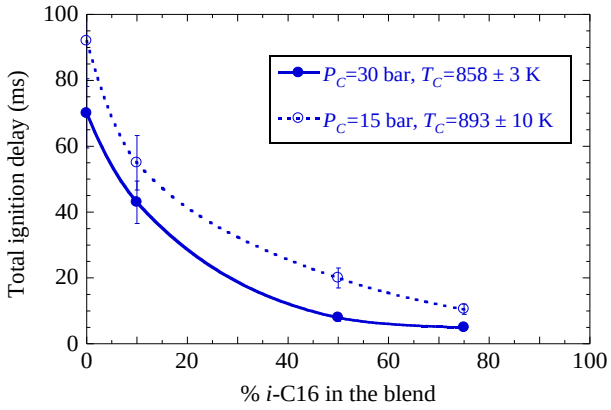

Figure 5.6 Plot showing total ignition delay variation with % *i*-C16 in the *i*-C16/1-MN blend.

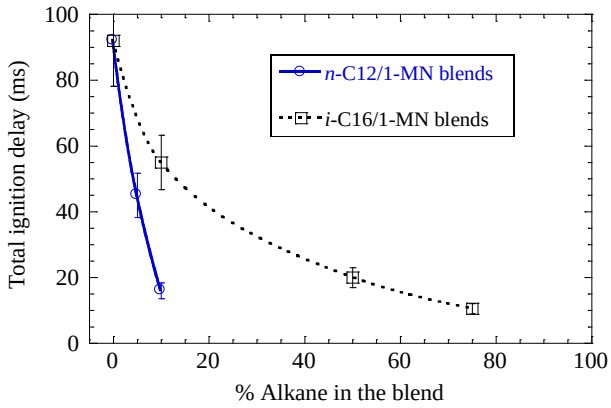

Figure 5.7 Plot showing total ignition delay variations with % *n*-C12 and % *i*-C16 in the blends, conducted at P_C=15 bar and T_C=893±10 K.

From the different binary blends listed in Tables 5.1 and 5.2, the two binary blends with closely-matched DCN values of ~13 are the 10/90 blend of *n*-C12/1-MN and the 75/25 blend of *i*-C16/1-MN. Comparison of their total ignition delays over a range of compressed temperatures, as shown in Fig. 5.8, provides information of whether surrogate mixtures with very similar cetane rating but distinct blend compositions exhibit similar ignition response. This would in turn demonstrate whether matching the cetane rating is a sufficient criterion for a surrogate mixture to emulate the ignition resposne of the target real fuel. Figure 5.8 shows that despite a similar DCN, the two blends of interest exhibit significant differences in both ignition propensities and

characteristics. This observation is consistent with our recent study on fully blended diesel fuels [79]. In addiiton, the 10/90 blend of *n*-C12/1-MN shows a strong low temperature reactivity and an associated negative temperature coefficient (NTC) response, while neither of these features were not observed in the 75/25 *i*-C16/1-MN blend. It is well established that linear paraffins (*n*-alkanes) exhibit a stronger low temperature reactivity than highly branched paraffins (*iso*-alkanes). Thus, the differences in low temperature reactivities of the two blends under considertation here can be attributed to the differences in molecular structures. Furthermore, the comparison shown in Fig. 5.8 illustrates that matching the cetane rating alone is not a sufficient criterion in surrogate formulation to capture the ignition characteristics of the target real fuel.

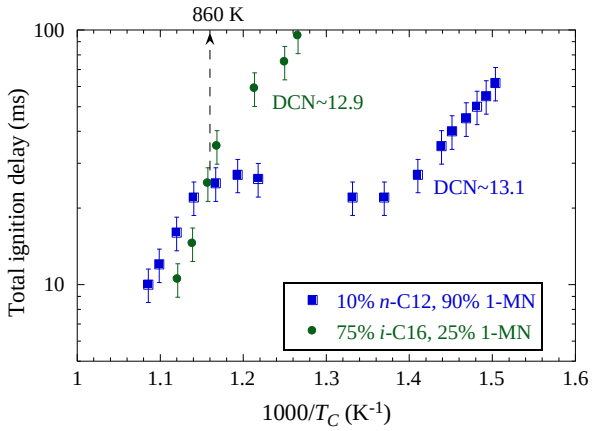

Figure 5.8 Comparison of total ignition delays of two blends with a similar DCN value but different blend compositions.

5.4. Ignition Delay Simulations

From a survey of the literature, we have identified several chemical kinetic models that describe the combustion chemistry of the three neat components [e.g., 48,61,78,50,80]. While the model of Narayanaswamy et al. [80] includes the kinetics of *n*-C12 and 1-MN, we could not identify a chemical kinetic model that describes the ignition chemistry of all the three hydrocarbons of interest in the current study. Hence, the simulated ignition delay results discussed in the following

shall mainly focus on the *n*-C12/1-MN blends using the model of Narayanaswamy et al. [80]. Further reasons for not conducting ignition delay simulations for the *i*-C16/1-MN blends shall be discussed in due course.

Figures 5.9(a) and 5.9(b) compare the experimental and simulated pressure traces for the 10/90 *n*-C12/1-MN blend and the neat 1-MN, respectively. The former case exhibits a two-stage ignition behavior, while a single-stage ignition response is observed for the latter. As a reference, the corresponding nonreactive pressure trace is also plotted in Fig. 5.9, clearly showing the instant when significant reactivity commences and the extent of pre-ignition heat release. Using the chemical kinetic model of Narayanaswamy et al. [80], it is seen from Fig. 5.9 that the simulated results qualitatively capture the autoignition characteristics in general, but under-predict the experimental ignition delays and over-predict the first-stage pressure rise and the extent of pre-ignition heat release.

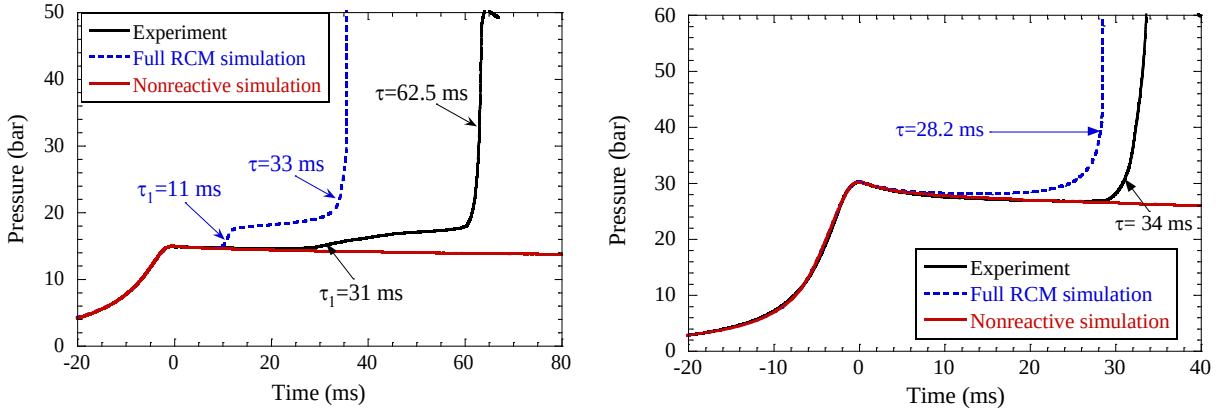

(a) P_C=15 bar, T_C=669 K, 10% *n*-C12, 90% 1-MN

(b) P_C=30 bar, T_C=878 K, 100%1-MN

Figure 5.9 Plot showing the comparison of pressure traces from experiments and simulations for (a) 10/90 *n*-C12/1-MN blend and (b) neat 1-MN.

Figure 5.10 shows the comparisons of the ignition delays of the pure components of *n*-C12 and 1-MN, as well as the different *n*-C12/1-MN blends, obtained from experiments and simulations. At P_C=15 bar, Fig. 5.10(a) displays that the simulated results using the sub-

mechanism of *n*-C12 in the model of [80] are significantly less reactive than the current RCM data at low temperatures (T_C<700 K). Therefore, the discrepancies noticed at low temperatures illustrate that further improvements are necessary to the *n*-C12 sub-mechanism of [80]. Figure 5.10(b) compares the experimental and simulated total ignition delays of neat 1-MN at P_C=15 bar and 30 bar. The simulated results obtained using the 1-MN sub-mechanism of [80] appear to be more reactive than the RCM data at lower end of the compressed temperatures. It is further noted from Fig. 5.10(b) that the difference between experimental and simulated results decreases gradually with increasing T_C up to a compressed temperature where a crossover in reactivity is observed. Beyond the crossover point, the 1-MN sub-mechanism of [80] becomes less reactive than the current RCM experiments.

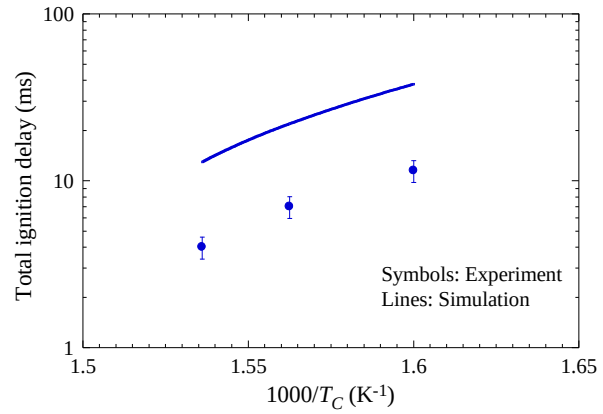

(a) 100% *n*-C12, P_C=15 bar

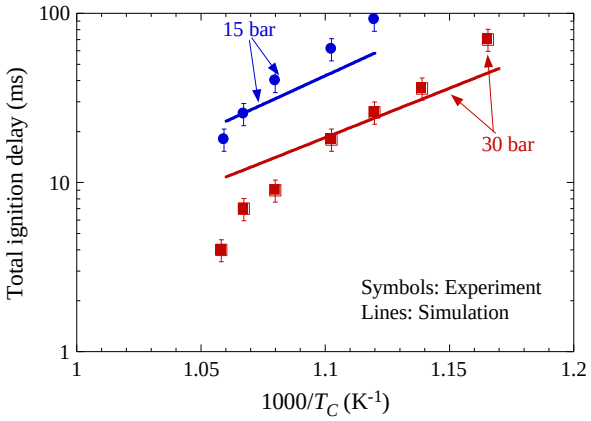

(b) 100% 1-MN

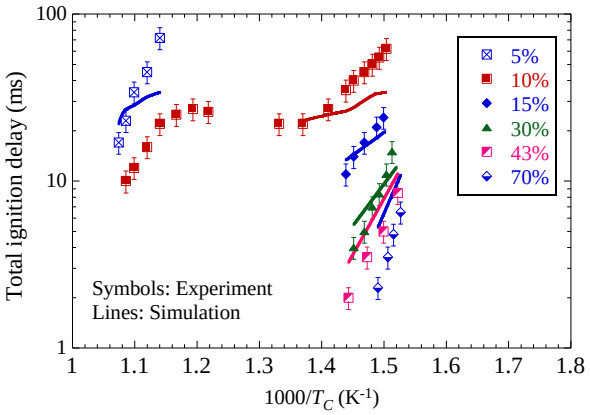

(c) *n*-C12/1-MN blends, P_C=15 bar

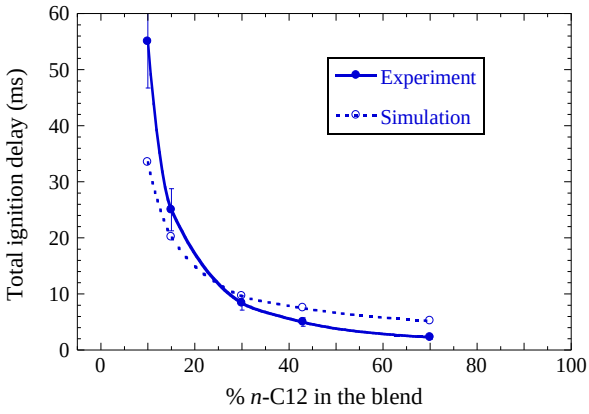

(d) P_C=15 bar, T_C=669±3 K

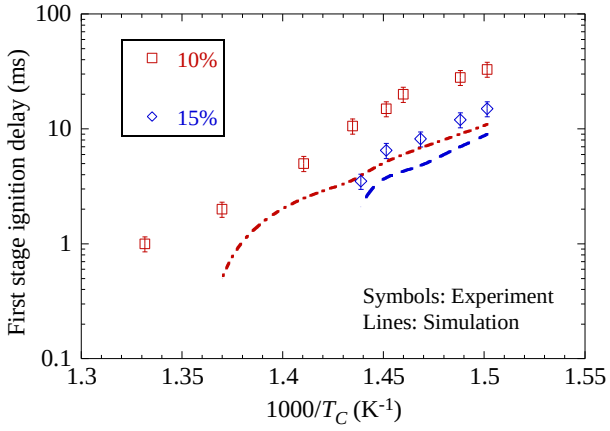

(e) *n*-C12/1-MN blends, P_C=15 bar

Figure 5.10 Comparisons of total ignition delays of (a) neat *n*-C12, (b) neat 1-MN, and (c) *n*-C12/1-MN blends over a range of T_C, (d) total ignition delays of *n*-C12/1-MN blends at T_C~669 K, and (e) first stage ignition delays of *n*-C12/1-MN blends from experiments and simulations using the model of Narayanaswamy et al. [80].

The total ignition delays of the *n*-C12/1-MN blends obtained from experiments and simulations are compared in Fig. 5.10(c) for P_C=15 bar. The performance of the model of [80] in estimating the total ignition delays of the binary blends does not show a consistent trend and is found to be dependent on the % *n*-C12 in the blend, which can be better understood from the total ignition delay comparison shown in Fig. 5.10(d) for T_C~669 K. Specifically, the simulated total ignition delay of the blend containing 70% *n*-C12 is seen to be about a factor of two greater than the experimental value, while the simulated results of the blends containing 15% and 30% *n*-C12 compare well against the experimental data with the differences being close to the experimental uncertainty. On the other hand, the simulated total ignition delay of the 10% *n*-C12 blend is a factor of 1.7 lower than the experimental value. For compressed temperatures greater than 730 K, since the RCM simulations for the blend containing 10% *n*-C12 exhibit ignition during the compression stoke, those simulated results are not shown in Fig. 5.10(c). Further, the comparison of the total ignition delays of the blend containing 5% *n*-C12 over a range of compressed temperatures from experiments and simulations shows trends similar to those observed in the pure 1-MN case of Fig. 5.10(b).

Figure 5.10(e) shows the comparison of the first stage ignition delays observed from simulations and experiments for the blends containing 10% and 15% *n*-C12. The first stage ignition delays predicted by the model are consistently shorter, with the simulated values being generally about a factor of two shorter than the experimental results. It is to be noted that the simulated total ignition delays of the 15% *n*-C12 blend are seen in Fig. 5.10(c) to match closely with the experimental data while the first stage ignition delays differ by a factor of two. To summarize, the model of Narayanaswamy et al. [80] qualitatively captures the ignition delay variations with % *n*-C12 in the blend, despite showing significant differences in the quantitative values. The

discrepancies observed in the simulated and experimental ignition delays of binary blends can be primarily attributed to the efficacy of the model performance against the ignition delays of pure components of 1-MN and *n*-C12.

Using the model of Oehlschlaeger et al. [61], Fig. 5.11 compares the experimental and simulated total ignition delays of stoichiometric *i*-C16/air mixtures at P_C=15 bar. As seen from Fig. 5.11, the model of [61] is more reactive than experiments for T_C<815 K and the discrepancy increases with decreasing T_C. Besides the differences in total ignition delays, the pressure traces from simulations show a two-stage like ignition in the compressed temperature range investigated, which, however, was not observed in the RCM experiments. It has to be pointed out that the model of [61] was developed based on the *iso*-octane model of Curran et al. [36] and to our knowledge it has never been validated against the experimental data of *i*-C16 at low temperatures. Modifications to the chemical kinetic models of various *n*- and *iso*-alkanes developed on the basis of the models of Curran et al. [36,37] have recently been proposed to improve their predictive nature [81-83], and hence similar modifications might be necessary to improve the fidelity of the *i*-C16 model of [61]. Considering the poor performance of the *i*-C16 model available in the literature, further ignition delay simulations of the current binary blends of *i*-C16/1-MN were not conducted.

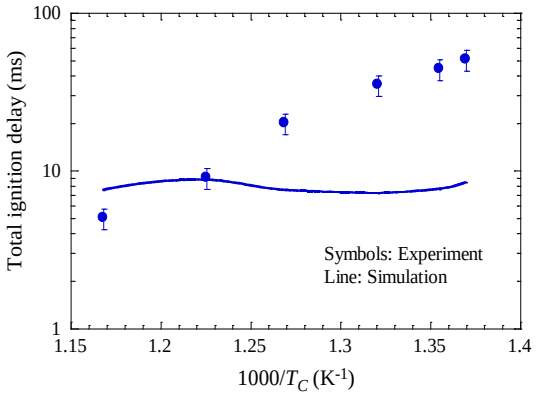

Figure 5.11 Comparison of ignition delays from experiments and simulations for neat *i*-C16 at P_C=15 bar. Simulations were conducted using the model of Oehlschlaeger et al. [61].

Comparisons shown in Figs. 5.10 and 5.11 illustrate the several differences observed in experiments and simulations and highlight the needs for refining the chemical kinetic models of *i*-C16, *n*-C12, 1-MN, and their blends. The changes suggested in the section 4.4.4 could improve the fidelity of the 1-MN sub-mechanism of [80]. In addition, the possible modifications needed to improve the fidelity of the models of *i*-C16 and *n*-C12 include reevaluating the thermodynamic properties of the important species, addition of missing reaction pathways, and updating the reaction rate rules of various reaction classes as done by the studies of [81-83]. Modifying the models of *i*-C16, *n*-C12, and 1-MN would require comprehensive chemical kinetic studies which are beyond the scope of the current study, and for the same reason further chemical kinetic analyses were not conducted here.

5.5. Conclusions

Ignition delay measurements of the binary blends of *n*-C12/1-MN and *i*-C16/1-MN were conducted using a rapid compression machine. Experiments were conducted with stoichiometric blend/air mixtures at elevated pressures of P_C=15 bar and 30 bar and at compressed temperatures of T_C=626–944 K. For a given set of P_C and T_C, the experimental results showed that an increase in % *n*-C12 in the *n*-C12/1-MN blend resulted in a nonlinear decrease in the total ignition delay with a steep drop when small amounts of *n*-C12 were added. An increase of % *i*-C16 in the *i*-C16/1-MN blend was also found to cause a nonlinear decrease in total ignition delays, but the drop in the small *i*-C16 addition regime was not as steep. In addition, the total ignition delay data of the binary blends, with a similar DCN value but with different blend compositions, demonstrated that

they can exhibit significant differences in reactivity and autoignition characteristics over a range of compressed temperatures.

Ignition delay simulations were further conducted to assess the performances of the chemical kinetic models available in the literature. Significant discrepancies were noted between the experimental and simulated ignition delays of the binary blends of *n*-C12/1-MN when using the model of Narayanaswamy et al. [80], while this model was seen to capture the qualitative trends observed in experiments. Even for the neat components of *n*-C12 and 1-MN, the comparison of the present RCM data and the simulated results using the model of [80] showed significant differences at low temperatures. For the simulations of the neat *i*-C16 experiments, the model of Oehlschlaeger et al. [61] was found to be significantly more reactive than RCM experiments, with the discrepancy increases with decreasing compressed temperature. The results from the current study show that the *n*-C12/1-MN model of [80] and the *i*-C16 model of [61] need further improvement at low temperatures.

Chapter 6 : ULSD#2 and FD9A diesel blends

6.1 Introduction

Cetane ratings determined using the American Society for Testing and Materials (ASTM) standard test procedures, such as cetane number (CN) [84] and derived cetane number (DCN) [85], are widely used to quantify the ignition quality of a fuel. In the ASTM standard test procedures, liquid fuel is injected into hot oxidizer gases and the induction time for the mixture to ignite is measured. The induction time or the ignition delay time is then used to determine the cetane rating of a fuel. It is noted that this measured ignition delay time includes both physical and chemical induction times. The physical induction time is related to spray processes during which the liquid fuel breaks down into droplets, vaporizes, and mixes with hot oxidizer to form a combustible mixture. On the other hand, the chemical induction time relates to the time taken by the combustible mixture to ignite. The processes prevalent in the ASTM test procedures that are used to determine the cetane ratings are similar to those encountered in conventional compression ignition (CI) engines. Thus, the cetane rating of a fuel is a good metric to understand how a fuel would perform in a conventional CI engine. A recent computational study [86] has shown that for the induction times relevant to diesel fuels in the ASTM test vessels, the physical induction times dominate the ignition delays. Since the cetane rating is heavily influenced by physical processes, it may not be a good indicator of fuel ignition propensity in homogeneous ignition conditions.

The engines operating on LTC modes, such as partially premixed compression ignition (PPCI), are designed to operate at lower in-cylinder charge temperatures, greater degree of premixing, and higher dilution levels, which slow down the overall reactions leading to ignition. Delaying the ignition timing results in increasing dominance of fuel chemistry and leads to flame structure, heat release rate (HRR) profile, and temperature stratification that are different from

those observed in conventional CI engines [2]. This increase in influence of ignition chemistry on the performance of LTC engines underscores the importance of understanding the autoignition characteristics of diesel fuels under LTC-relevant conditions, namely high pressures and low-to-intermediate temperatures.

Table 6.1: List of literature studies on autoignition of diesel blends.

Study	Facility	Pressure (atm)	Temperature (K)	ϕ	Oxidizer
Spadaccini and Tevelde [87]	Flow	10−30	625−1000	0.3−1	Air
Penyazkov et al. [88]	Shock Tube	4.7−10.4	1065−1838	0.5−2	Air
Haylett et al. [90]	Shock Tube	1.7−8.6	947−1261	0.2−1	O_2 (4, 21%), rest Ar
Gowdagiri et al. [91]	Shock Tube	10, 20	671−1266	0.5, 1	Air

Very few studies in the literature have focused on autoignition characteristics of diesel fuels. The literature studies that focused on ignition delay times of diesel fuels are listed in Table 6.1, including the facilities and the conditions of pressure, temperature, equivalence ratio, and dilution used in the experiments. Spadacinni and Tevelde [87] conducted ignition delay time measurements of diesel type fuels in a continuous flow reactor. The fuels studied in [87] included Jet-A, JP-4, n-cetane, No. 2 diesel, and a research grade diesel. The ignition delay time correlations deduced from their measurements showed that Jet-A was more reactive than No. 2 diesel [88]. Penyazkov et al. [88] measured ignition delay times of American commercial diesel (DF-2) using a pre-heated shock tube and compared the ignition delay times of DF-2 with those of Jet-A taken from Dean et al. [89]. The comparison of [88] showed that the ignition delay times of DF-2 were higher than those of Jet-A, with a factor of 2–6 difference depending on the conditions. Haylett et al. [90] conducted ignition delay time measurements of four different diesel blends, including a European grade diesel with CN~55 and three American grade diesels with DCN~42–46, in an aerosol shock tube to understand the effects of cetane rating and aromatic content percentage on ignition propensities. Haylett et al. [90] found that the differences in ignition delay were small and that the

ignition delay times generally decreased with increasing cetane rating. In addition, the measured ignition delay times of the American grade diesel fuel of CN~43 by Penyazkov et al. [88] and by Haylett et al. [90] were seen to show a good agreement. Gowdagiri et al. [91] recently reported the ignition delay times of petroleum (F-76) and algae (HRJ-76) derived diesel blends. The two diesel blends used in [91] exhibited big differences in DCN values and compositions. Specifically, the DCN of F-76 was reported to be 48.8, while that of HRJ-76 was reported to be 76 [91]. Despite of the differences in DCN values and fuel compositions, Gowdagiri et al. [91] noticed that the ignition delay times of the two diesel blends were indistinguishable for temperatures greater than 1000 K. Gowdagiri et al. [91] also observed that the petroleum derived diesel (F-76) and Jet-A exhibited identical ignition delay times across a wide range of temperatures they investigated.

Clearly, more ignition delay datasets of diesel reference fuels are needed in order to fully understand the effects of cetane rating and fuel composition on ignition propensities. Therefore, the objectives of the current study are two-fold. First, using a heated rapid compression machine, two fully-characterized diesel reference fuels with similar cetane rating but different compositional characteristics have been studied to explore the effect of fuel composition on ignition propensities by measuring and comparing their ignition delay times over a wide range of pressures and temperatures. The two diesel reference fuels used herein were a commercial grade ultra-low-sulfur diesel (ULSD) #2 reference fuel, ULSD#2, and a Fuels for Advanced Combustion Engines (FACE) research diesel, FD9A. These two diesel blends have been chosen as their cetane ratings are similar to those of the diesel fuels used in the conventional diesel engines and they have received special attention from the engine community, especially the Coordinating Research Council (CRC). In addition, there are ongoing, concerted efforts in developing surrogates for these well-characterized diesel reference fuels and the associated chemical kinetic models. Hence, the

second objective of this investigation is to provide benchmark ignition delay database of the two diesel fuels at varying pressures, oxygen concentrations, and temperatures needed for development and validation of surrogate models.

In the following, a detailed comparison of the properties and compositions of the two diesel blends used in the current study and those studied in the literature shall be first discussed. The experimental facility, its characterization, and the test matrix will be introduced and specified next, followed by the presentation and discussion of the present experimental results.

6.2 Properties and Compositions of Diesel Blends

ULSD#2 was obtained from Chevron Phillips, while FD9A was acquired from the CRC. Table 6.2 shows and compares the properties and compositions of the two diesels used in the current study and F-76 used in [91]. It is noted that different types of analyses were conducted by the CRC to determine the compositions of the diesel blends, and the compositional characteristics of ULSD#2 and FD9A from these different types of analyses documented in the CRC reports [21,43,93,94] show noticeable differences in fuel composition for the given blend. Considering the differences in the reported compositions, the average values of the compositional characteristics from the latest report, determined using 2D GCMS [43], are listed in Table 6.2. The interested reader is referred to the original reports [23,42,92,93] for further details.

As seen from Table 6.2, while both ULSD#2 and FD9A exhibit similar CN and DCN values, H/C ratio, density, and heats of combustion, their compositions are different. In particular, FD9A contains higher amounts of aromatics accompanied by lower amounts of saturates when compared to ULSD#2. However, in terms of weight percentage of paraffins (*n*-alkanes + *iso*-alkanes), both the blends constitute similar amounts – 34.82% in ULSD#2 and 33.50% in FD9A. Comparison of the weight percentages of the aromatic components shows that FD9A contains higher amounts of

alkylbenzenes – more than double of that in ULSD#2. In addition, 2D GCMS analysis of [42] showed that FD9A has high amounts of C_8–C_{10} alkylbenzenes which constitute to about 75% of the total alkylbenzenes. It is also observed that ULSD#2 consists of higher amounts of aromatics with more than two aromatic rings when compared to FD9A.

Table 6.2: Comparison of properties and compositions of the diesel blends used in the current study and in Gowdagiri et al.[91].

Property/Composition	ULSD#2	FD9A	F-76
H/C ratio[23,91]	1.80	1.80	1.80
DCN[23,91]	43.7	44.2	48.8
CN[23]	43.3	43.9	-
Density (kg/m^3)[23]	848	846.2	-
Heat of combustion (MJ/kg)[23]	42.90	42.86	-
Saturates (% weight)[42,91]	69.85	65.20	82
iso-Alkanes	18.44	22.37	20
n-Alkanes	16.38	11.13	56
Cycloalkanes	35.03	29.05	6
Aromatics (% weight)[42,91]	30.05	34.67	16
Alkylbenzenes	9.83	21.55	-
Indanes/Tetralins	8.13	10.77	-
> 2 aromatic rings	12.09	5.04	2
Others[42,91]	0.10	0.13	2

Further comparison of the properties and compositions of the diesel fuels used in the current study and in the literature studies has been conducted to understand their differences and similarities. When comparing the current experimental results with the literature data later on, this comparison can also provide insight into the effects of fuel composition on autoignition in different temperature regimes. Although Penzyazkov et al. [88] did not provide fuel property characterization for the commercial diesel No. 2 used in their study, their blend might be similar to the present ULSD#2. In Haylett et al. [90], the DF-2 diesel blend used in their study was reported to be similar to the blend used by Penzyazkov et al. [88]. Since Gowdagiri et al. [91] reported the properties and compositions of the petroleum derived diesel F-76 used in their study, those values

are shown and compared in Table 6.2. It is seen that while the H/C ratios of ULSD#2, FD9A, and F-76 are similar, F-76 contains very high amounts of n-alkanes – a factor of 3.42–5.03 higher in terms of weight percentage. In regard to cetane rating comparison, only the DCN value of F-76 was reported in [91] and it is seen to be close to those of ULSD#2 and FD9A, but with a higher value by about 5 units.

6.3 Experimental Specifications

6.3.1 Estimation of Compressed Temperature (T_C)

The compressed temperature (T_C) was not measured directly and was deduced using the adiabatic core hypothesis:

$$\int_{T_0}^{T_c} \frac{\gamma}{\gamma - 1} \frac{dT}{T} = \ln\left(\frac{P_c}{P_0}\right), \qquad (1)$$

where P_C, P_0, and T_0 are measured values and γ is the ratio of specific heats. As such, estimation of compressed temperature requires prior knowledge of the thermodynamic properties of the test fuel. As the thermodynamic properties of transportation fuels are typically not available, the thermodynamic properties of their surrogates are often used for calculating reference temperatures in RCM and shock tube experiments. Gowdagiri et al. [91] used *n*-cetane as the thermodynamic surrogate for estimating the temperatures behind the reflected shock waves in their study. In the current study we used a three-component blend of 37% *n*-cetane, 40% *iso*-cetane, and 23% 1-methyl naphthalene (by liquid volume) as the thermodynamic surrogate. This three-component blend was chosen as its H/C ratio of 1.78, molecular weight of 194.2 gm/mol, and DCN (based on linear correlation by liquid volume) of 43 match closely with those of ULSD#2 and FD9A (cf. Table 6.2). Gowdagiri et al. [91] pointed out in their study that the uncertainty in the estimated temperature due to the use of different thermodynamic properties of surrogates is very small (~1

K). If *n*-cetane is used as the thermodynamic surrogate following [91], the typical difference in the estimated T_C as compared to that using the three-component blend is ~1 K. Based on an error propagation analysis [32], the total uncertainty in the estimated compressed temperature is about ±5 K, with the majority arising due to the uncertainty of ±1.5 K in the initial temperature measurement.

6.3.2 Test Conditions

Table 6.3 outlines the test conditions investigated in the current study. All the RCM experiments were conducted with mixtures of diesel/O_2/N_2 at a fixed fuel mole percentage of X_{diesel}=0.514%. The mole percentages of the fuel and O_2 at a given equivalence ratio was calculated using the composition of diesel to be represented by $C_{14}H_{25.30}$, based on the molecular weight of ~193.30 calculated from the molecular composition of the constituents reported in [91] and the H/C ratio of ~1.80. This estimated molecular weight of the diesel was found to match closely with that of the surrogate formulated by Mueller et al. [23]. For the current experiments, equivalence ratio was varied by varying the oxygen concentration while maintaining a fixed fuel loading. The oxygen concentrations investigated herein cover the range typical for engines operating with EGR [2]. The ignition delay time measurements conducted with varying concentrations of oxygen help in understanding the effect of dilution on autoignition. In addition, the compressed pressures and temperatures investigated were chosen to obtain ignition delay data complementary to the shock tube data in the literature, thereby facilitating comparison of ignition delay results over a wide range of conditions to understand the effect of fuel composition on ignition propensity.

Table 6.3: Test conditions investigated in the study on diesel fuels.

ϕ	$X_{diesel\ \%}$	$X_{O2\ \%}$	P_C (bar)	T_C (K)
0.5	0.514	20.9	10, 20	678−938
0.69	0.514	15.12	10, 15	678−938
1.02	0.514	10.24	15, 20	678−938

6.3.3 Vaporization Checks

When constructing the present test conditions, theoretical and experimental exercises were conducted to ensure that the diesel fuel injected to the mixing chamber vaporized completely. Our earlier studies have experimentally shown the present mixture preparation method to be adequate without fuel condensation [12,14,15]. In a theoretical effort to examine the potential condensation issue when handling a diesel fuel, the partial pressures of the constituents of the diesel blend were calculated and compared to the corresponding saturated vapor pressures at a given preheat temperature. These partial pressure calculations used the ideal gas law and the mole percentages of the constituents deduced from the weight percentage information available in [93]. In addition, the saturated vapor pressure of each constituent considered was obtained from [94]. Calculations showed that for the molar composition of the diesel tested, the preheat temperature of 420 K was sufficiently high to ensure complete vaporization of all the components for the diesel injected into the mixing chamber when the total pressure of the fuel was less than 14 Torr.

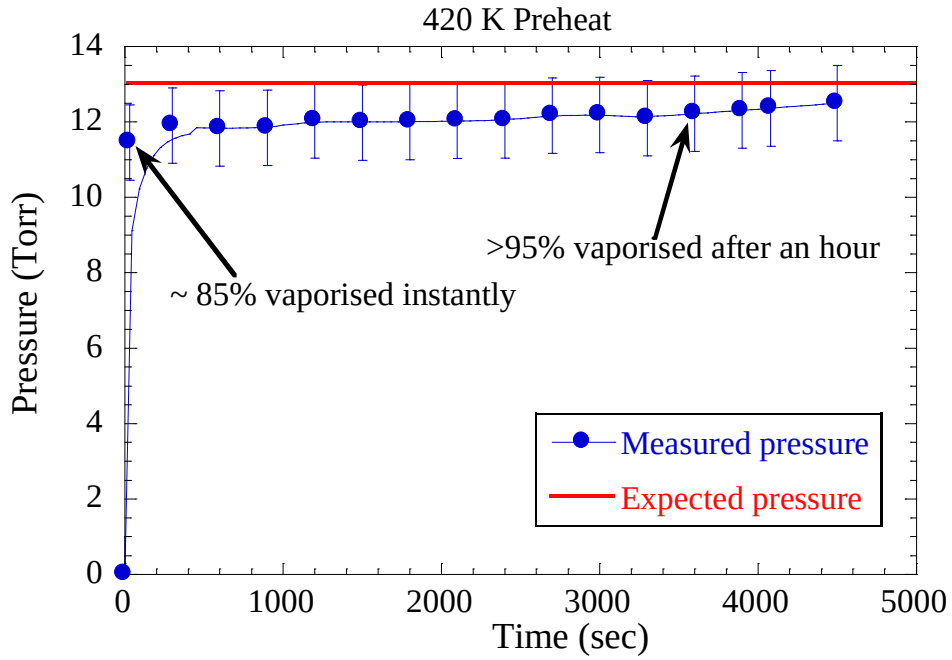

Figure 6.1 Plot showing the measured pressures in the mixing chamber after liquid fuel injection. The pressure expected from complete fuel vaporization calculated using the ideal gas law is also shown as a reference.

With a chamber preheat temperature of 420 K, Fig. 6.1 shows the time variation of chamber pressure measured using a pressure transducer after a known mass of diesel fuel was injected into the heated mixing chamber. The pressure computed from the ideal gas law assuming that the diesel fuel injected into the heated mixing chamber has completely vaporized, which is about 13 Torr, is also indicated in Fig. 6.1 as a reference. Moreover, the error bars shown in Fig. 6.1 correspond to the uncertainty in pressure measurements which is about 0.05% of the full scale reading of the transducer (0–5200 Torr), namely ±2.6 Torr. It is seen from Fig. 3 that the majority of the diesel fuel, more than 85%, vaporizes instantly in the mixing chamber and subsequently the pressure in the mixing chamber rises gradually to more than 95% of the expected value in an hour. The gradual increase in pressure could be due to either the fuel vaporization or pyrolysis of fuel components.

The rate of decomposition of fuel at the current pre-heat temperatures calculated using the rates estimated from the recent experimental study [95] are in the order of 10^{-18}-10^{-11} s^{-1}, such a low rate of decomposition in addition with the low pressures would imply a negligible change in fuel concentration due to fuel pyrolysis. Thus, we can safely assume the decomposition of the fuel molecules to be negligible and the gradual increase in chamber pressure could be caused by preferential/slow vaporization of the heavier components. From the monitoring of the mixing chamber pressure, it is clear that more than 95% of the injected fuel has vaporized, indicating that the uncertainty in the nominal equivalence ratio is about 5% for the current experiments, which has been shown to be a typical uncertainty in equivalence ratio for preparation of homogenous liquid fuel/oxidizer mixtures in our previous study [16]. The loss (5%) in pressure recovered could be due to surface adsorption or loss.

Further experimental checks were conducted to ensure that the diesel fuel did not condense in the heated RCM. In this series of experimental checks, RCM experiments were conducted using diesel/air and gasoline/air mixtures with similar operating parameters, P_C, and T_C. FD9A diesel and FACE A gasoline were used, and their measured pressure traces in RCM reactive experiments were compared. Since both FD9A and FACE A exhibit similar heat of combustion values and stoichiometric fuel/air mass ratios, it is expected that when diesel/air and gasoline/air mixtures with an identical equivalence ratio are ignited in the RCM, their post hot-ignition pressures should be comparable if each fuel has vaporized completely. The fuel/air mixtures prepared in the mixing chamber and heated to desired pre-heat temperatures to about 4 hours were compressed to desired P_C and T_C. GCMS tests on reactive mixtures of *n*-decane (DCN ~65), a fuel with higher cetane ratings than diesel, earlier conducted at our lab [16] showed no evidence of oxidation of fuel in the mixing chamber, hence, we expect the oxidation of fuel to be negligible in the current study too.

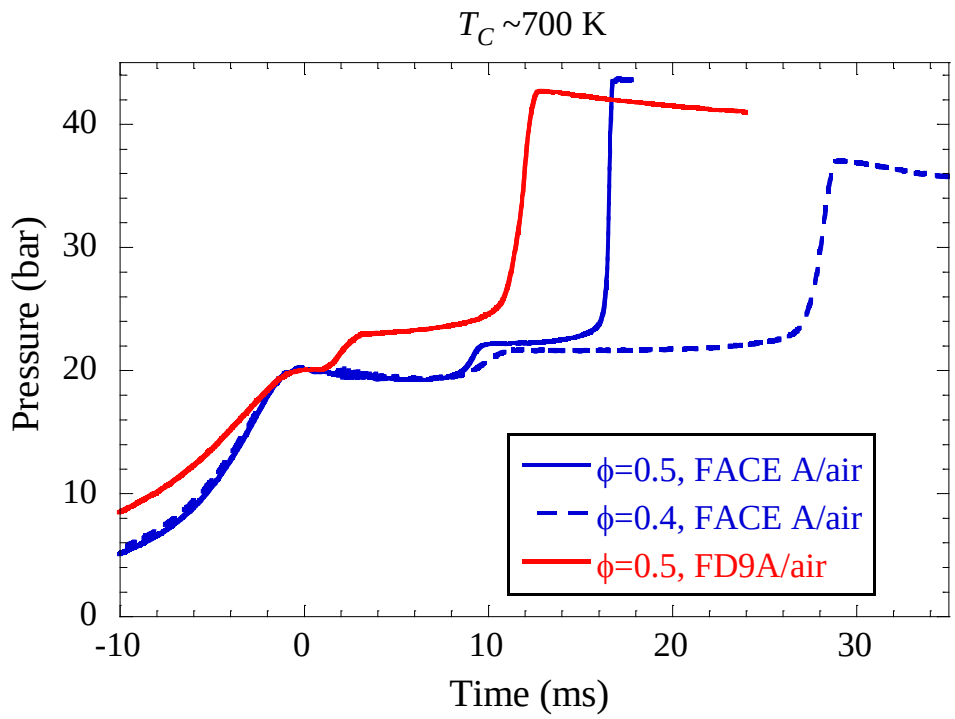

Figure 6.2 Comparison of measured pressure traces of ignition of FACE A gasoline and FD9A diesel at similar compressed conditions of P_C = 20 bar and T_C ~ 700 K.

Comparison of pressure traces of FD9A/air and FACE A/air mixtures at ϕ=0.5 and FACE A/air mixture at ϕ=0.4 is shown in Fig. 6.2, at almost identical compressed pressure and compressed temperature. It can be seen from Fig. 6.2 that at ϕ=0.5 in air the post-hot ignition peak pressures of FD9A diesel and more volatile FACE A gasoline are nearly identical. In addition, the post-hot ignition peak pressure of ϕ=0.4 FACE A/air mixture is significantly lower than those of ϕ=0.5 mixtures, thereby indicating that the equivalence ratio of the FD9A/air mixture is much closer to ϕ=0.5 than ϕ=0.4. Based on these theoretical and experimental exercises, we are confident that the condensation of diesel fuel is not an issue in the current experimental facility.

6.4 Experimental Results and Discussion

6.4.1 Ignition Characteristics of ULSD#2 and FD9A

Figures 6.3(a) and 6.3(b) show the raw pressure records of ULSD#2 and FD9A, respectively, at ϕ=0.5 in air, P_C=10 bar, and various compressed temperatures. Both diesel fuels are seen to exhibit two-stage ignition characteristics in the temperature range investigated. Moreover, the ignition delays of both diesel blends appear to decrease monotonically with increasing temperature for T_C<720 K – this temperature window is therefore referred as the low temperature regime (LTR). A negative temperature coefficient (NTC) behavior is observed for T_C in the range of 720–833 K, as in this temperature range the ignition delays increase with increasing temperature. For T_C>833 K, the ignition delays start to decrease monotonically with increasing temperature, and hence this temperature window is referred as the intermediate temperature regime (ITR). The RCM pressure traces with ϕ=0.5 diesel/air mixtures at P_C=20 bar are shown in Figs. 6.3(c) and 6.3(d), while the experimental results are limited to T_C<707 K as further increase in compressed temperature led to the initiation of ignition during the compression stroke. At this higher compressed pressure, two-stage ignition characteristics are also observed in the LTR for both ULSD#2 and FD9A. It is noted that the ignition delays and pressure records for the compressed conditions at which ignition events were initiated during the compression stroke have been discarded and not reported in the current study.

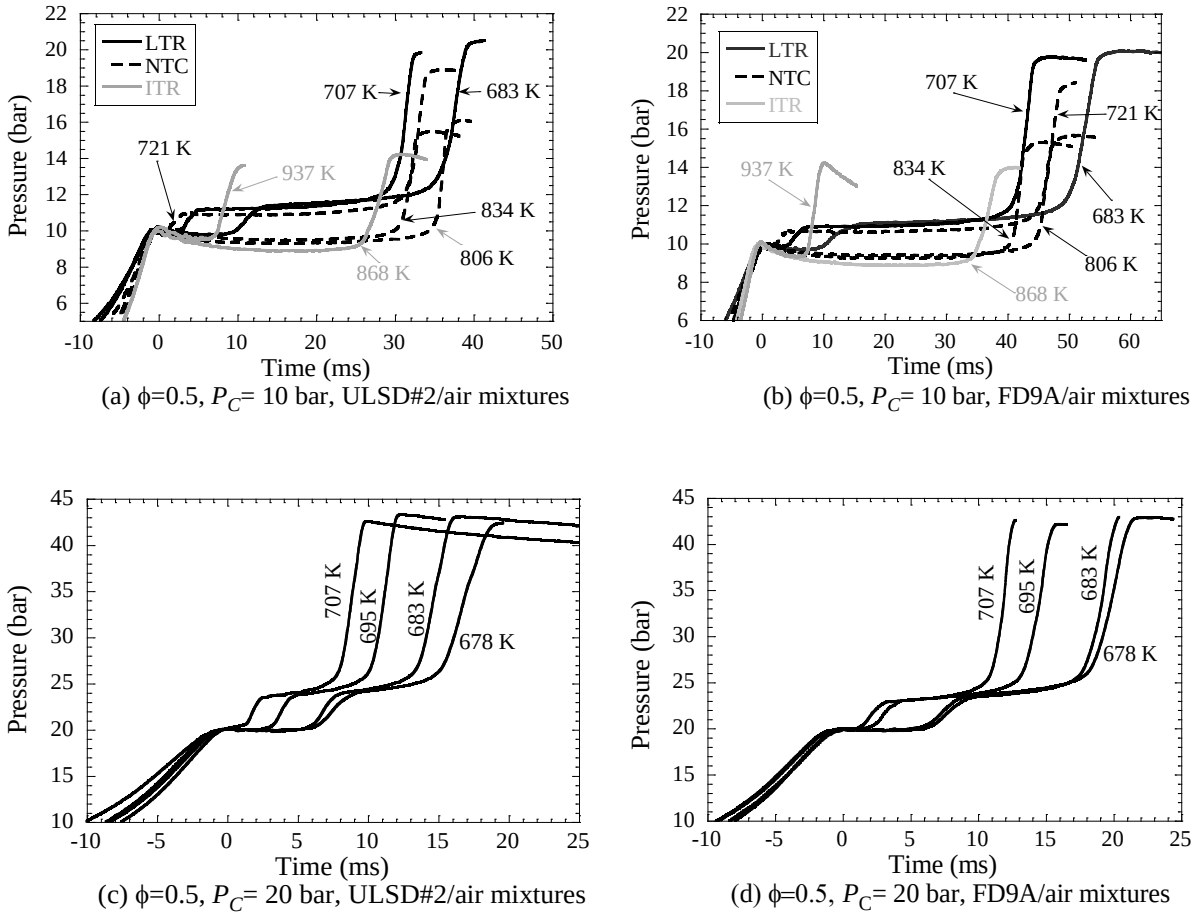

(a) ϕ=0.5, P_C= 10 bar, ULSD#2/air mixtures

(b) ϕ=0.5, P_C= 10 bar, FD9A/air mixtures

(c) ϕ=0.5, P_C= 20 bar, ULSD#2/air mixtures

(d) ϕ=0.5, P_C= 20 bar, FD9A/air mixtures

Figure 6.3 Plots showing the pressures traces of ULSD#2 and FD9A for ϕ = 0.5 in air at varying compressed temperatures and pressures

Figure 6.4 shows the ignition delays of ϕ=0.5 diesel/air mixtures of both ULSD#2 and FD9A at varying compressed pressures and compressed temperatures. Again, the ignition delays shown in Fig. 6.4 were deduced from the measured pressure traces according to the definitions demonstrated in Fig. 2.5. The error bars displayed in Fig. 6.4 represent the uncertainty of ±15% in the deduced ignition delays, as discussed earlier. The ignition delays, both first-stage and total ignition delays, were observed to decrease with increasing pressure. Additionally, the first-stage ignition delays were seen to decrease monotonically with increasing temperature, while the total

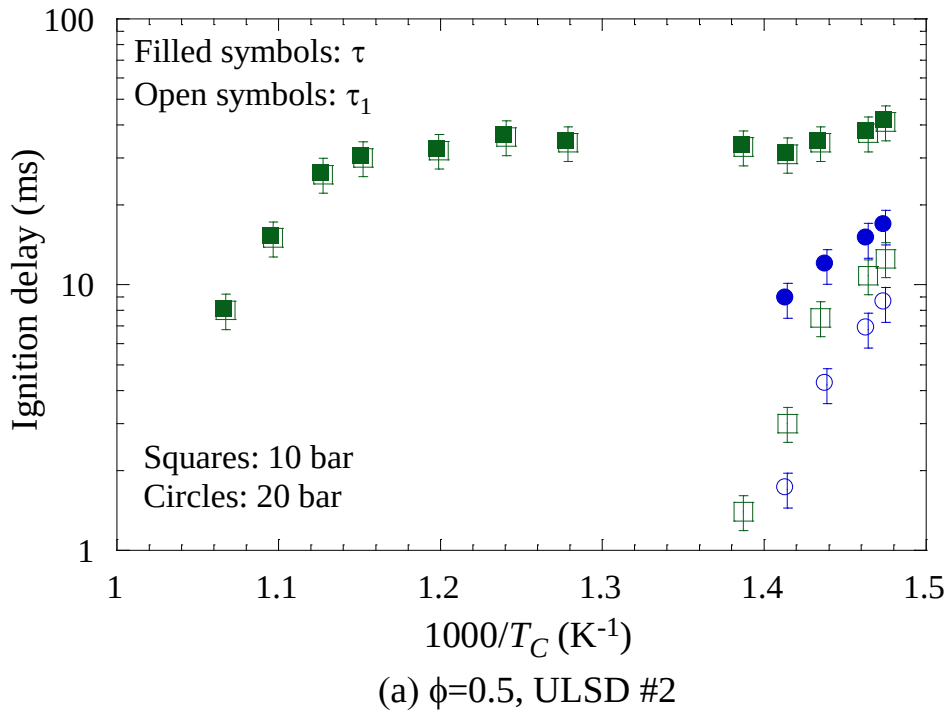

(a) ϕ=0.5, ULSD #2

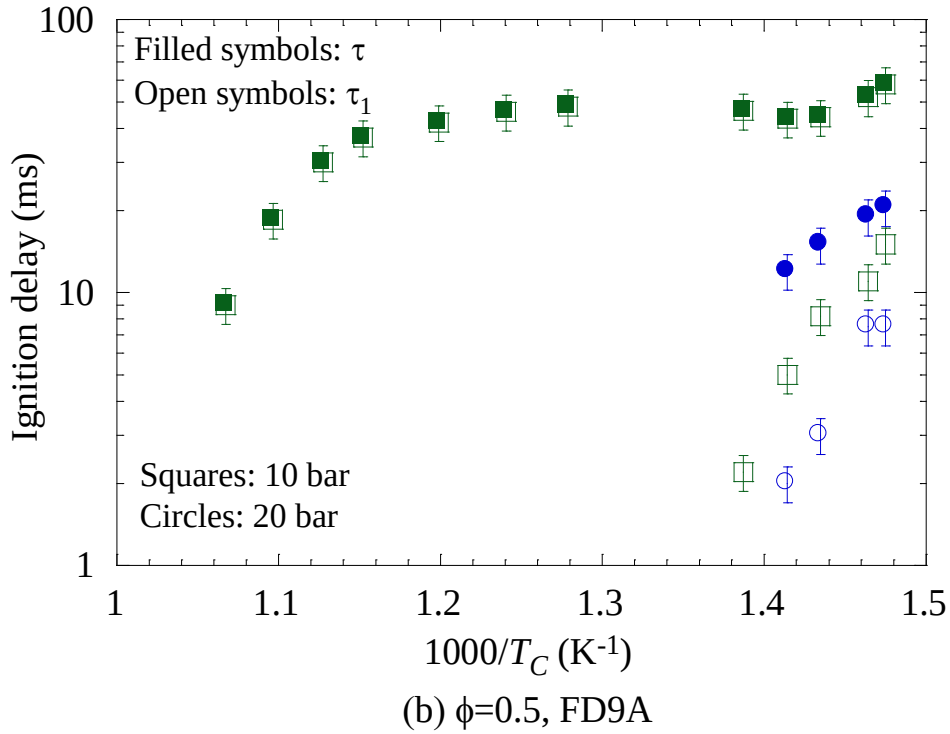

(b) ϕ=0.5, FD9A

Figure 6.4 Arrhenius plots of ignition delays (τ_1 and τ) of ϕ = 0.5 diesel/air mixtures at P_C = 10 and 20 bar: (a) ULSD#2 and (b) FD9A.

ignition delays exhibited an NTC response for compressed temperatures in the range of T_C=720–833 K at P_C=10 bar.

Figure 6.5 shows the effect of oxygen concentration on the reactivity of ULSD#2 and FD9A at different test conditions by keeping the fuel loading constant. It is seen from Fig. 6.5 that total and first-stage ignition delays increase with an increase (a decrease) in equivalence ratio (oxygen concentration). Comparison of the ignition delays at the conditions shown in Fig. 6.5 illustrates that the total ignition delays are more sensitive to change in oxygen concentration for compressed temperatures in the LTR and within the NTC regime. It is well known that for compressed temperatures in the NTC regime and LTR, reactivity is controlled by the addition of oxygen molecules (O_2) to fuel radicals (R) which leads to the formation of peroxy adducts (RO_2). A decrease in oxygen concentration is expected to reduce the effectiveness of these reactions, thus reducing the fuel reactivity. Such an effect of oxygen concentration on autoignition is clearly understood by the comparison of pressure traces shown in Fig. 6.6 for both diesel blends at P_C=20 bar and T_C=678 K. It can be observed that for this LTR compressed temperature, the decrease (increase) in oxygen concentration (equivalence ratio) results in an increase in τ_1 and a reduction in pressure rise due to the first-stage ignition. A higher first-stage pressure rise would imply a higher resulting temperature due to the first-stage ignition and a larger radical pool, both of which are known to accelerate the second-stage ignition (or hot ignition).

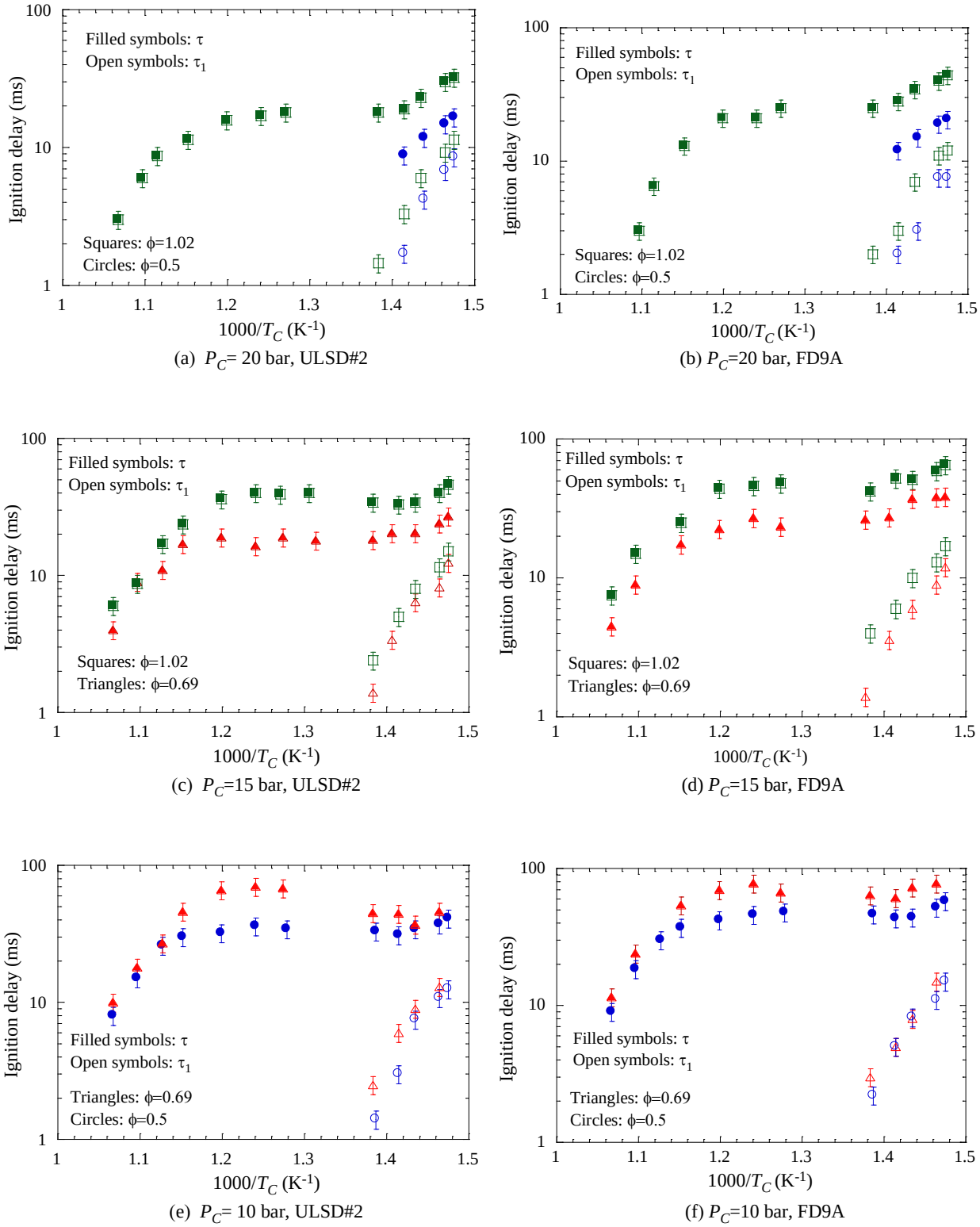

(a) P_C= 20 bar, ULSD#2

(b) P_C=20 bar, FD9A

(c) P_C=15 bar, ULSD#2

(d) P_C=15 bar, FD9A

(e) P_C= 10 bar, ULSD#2

(f) P_C=10 bar, FD9A

Figure 6.5 Arrhenius plots of ignition delays (τ_1 and τ) of ULSD#2 and FD9A at varying compressed pressures and equivalence ratios (i.e. oxygen mole percentages). The fuel mole percentage is kept constant at 0.514%.

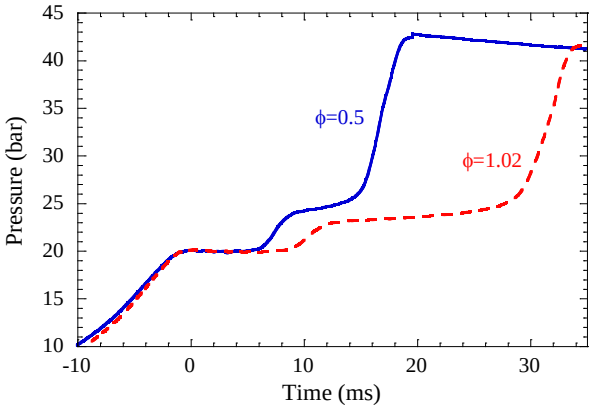

(a) T_C = 678 K, ULSD#2/O_2/N_2 mixtures

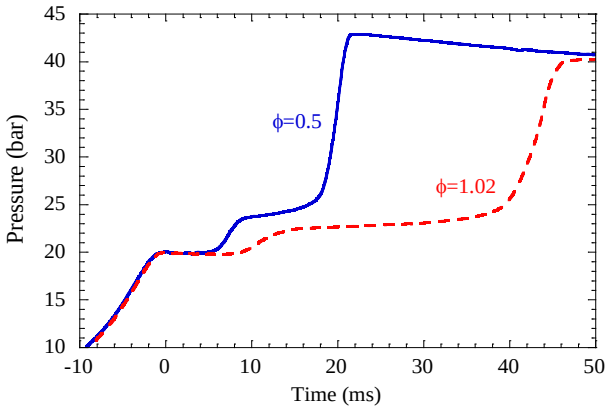

(b) T_C =678 K, FD9A/O_2/N_2 mixtures

Figure 6.6 Compression of pressure traces at P_C = 20 bar and T_C = 678 K with ϕ = 0.5 and 1.02 by varying oxygen mole percentage: (a) ULSD#2 and (b) FD9A. The fuel mole percentage is kept constant at 0.514%.

For compressed temperatures in the ITR, the β-decomposition reactions of fuel radicals start to compete with the reactions leading to the formation of peroxy adducts, resulting in a reduction of the sensitivity of the total ignition delay to change in concentration of oxygen, as shown in Fig. 6.6. The dependence of total ignition delays of diesel fuels on oxygen concentration observed in the current study are consistent with those observed in gasoline fuels [96-99] and jet fuels [33,100].

6.4.2 Comparison of Ignition Delays of ULSD#2 and FD9A

Figure 6.7 compares the ignition delays of the two research grade diesel fuels used in the current study. The first-stage ignition delays of the two blends were observed to be very similar at conditions tested. However, the total ignition delay comparison shows an interesting trend that is dependent on the temperature range of interest. In particular, the total ignition delays of FD9A were found to be higher than those of ULSD#2 for temperatures in the LTR, with the differences being less than 25%. The higher total ignition delays of FD9A and its relatively lower reactivity at low temperatures could be because it contains large amounts of aromatics, particularly the higher amounts of C_8–C_{10} alkyl benzenes (about 17% by weight). The differences in the total ignition delays of ULSD#2 and FD9A appear to reduce with increasing temperature, and the total ignition delays of the two blends become indistinguishable for temperatures in the ITR. It is also of interest to note that at temperatures around 820 K, the temperature range at which the ASTM procedure [86] is conducted to determine the DCN rating, the total ignition delays of the two blends are very similar. This ignition delay similarity inturn indicates that DCN ratings are good metrics of fuel reactivity at temperatures other than in the LTR.

The current experimental results show that the effect of fuel composition on ignition propensity is more pronounced at low temperatures than at intermediate-to-high temperatures. The observed trends can be attributed to the fact that the chain branching reactions which control ignition at low temperatures are more sensitive to the compositional characteristics. Won et al. [75] have recently shown that the binary blends of *n*-cetane/*iso*-cetane and *n*-dodecane/*iso*-octane with similar DCN ratings exhibited differences in total ignition delays in the LTR and NTC while their total ignition delays were identical for temperatures in the ITR. Their observed trends in reactivity were attributed to the fuel structure effects [75]. At high temperatures, ignition is controlled by the

smaller radical species formed from the breaking down of the fuel molecules, and hence the dependence of ignition propensity on the parent fuel structure is weakened, as noted by Dooley et al. [8].

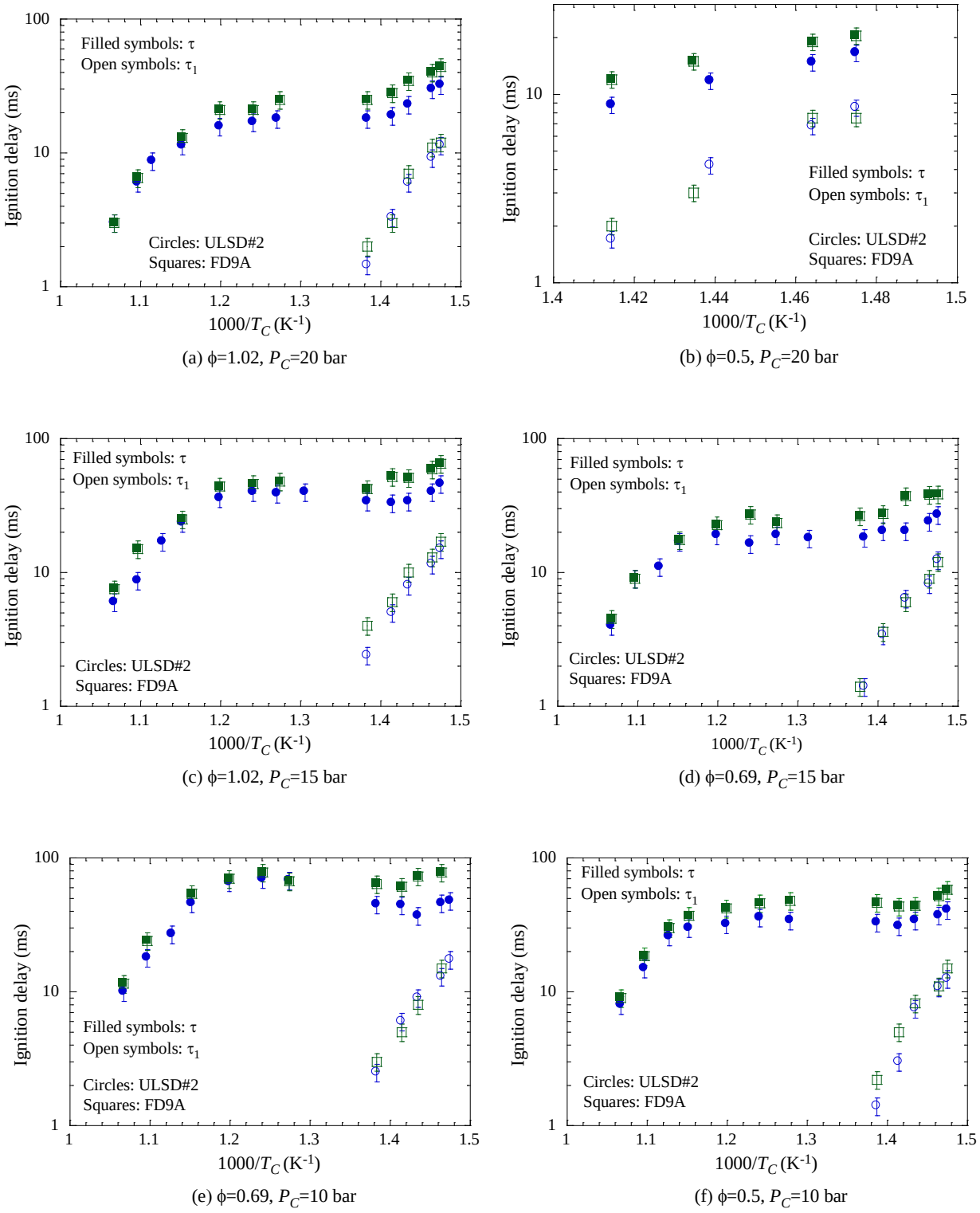

(a) ϕ=1.02, P_C=20 bar

(b) ϕ=0.5, P_C=20 bar

(c) ϕ=1.02, P_C=15 bar

(d) ϕ=0.69, P_C=15 bar

(e) ϕ=0.69, P_C=10 bar

(f) ϕ=0.5, P_C=10 bar

Figure 6.7 Comparison of ignition delays (τ_1 and τ) of ULSD#2 and FD9A at varying compressed pressures and equivalence ratios (i.e., oxygen mole percentages). The fuel mole percentage is kept constant at 0.514%.

6.4.3 Comparison of Current Total Ignition Delay Data and Literature Results

Figure 6.8 shows the comparison of the total ignition delay measurements from the current study and those reported in the literature. In Fig. 6.8 (a), the current RCM data are compared with the shock tube results of Haylett et al. [90]. Haylett et al. [90] conducted experiments at a nominal pressure of 6 atm, while the current set of experiments were conducted at a compressed pressure of P_C=10 bar. For the purpose of comparison, the shock tube ignition delays were scaled to 10 bar using the scaling factor suggested by Haylett et al. [90]. It can be observed from Fig. 6.8(a) that the current RCM measurements of the two blends at lower temperatures complement well with the shock tube measurements from Haylett et al. [90] at higher temperatures. In addition, since Haylett et al. [90] conducted their experiments at conditions in the ITR and higher temperatures, the ignition delay measurements of diesel blends with similar cetane ratings should be similar. This explains the complementary nature of ignition delays from the current study and those from Haylett et al. [90], as the diesel fuels compared have similar cetane ratings despite different compositional characteristics.

Figure 6.8 (b) compares the total ignition delays of ULSD#2, FD9A, and F-76. At compressed temperature of T_C~707 K, the total ignition delays of F-76 measured by Gowdagiri et al. [91] appear to be about a factor of 2 lower than the current results of ULSD#2 and FD9A. This total ignition delay discrepancy could be primarily due to the differences in fuel composition. As discussed earlier and shown in Table 6.2, F-76 has about 56% (by weight) of *n*-alkanes, while ULSD#2 and FD9A contain less than 17% (by weight). The high amounts of *n*-alkanes in F-76 are expected to promote chain-branching, low-temperature reactivity [91], thereby resulting in shorter ignition delays.

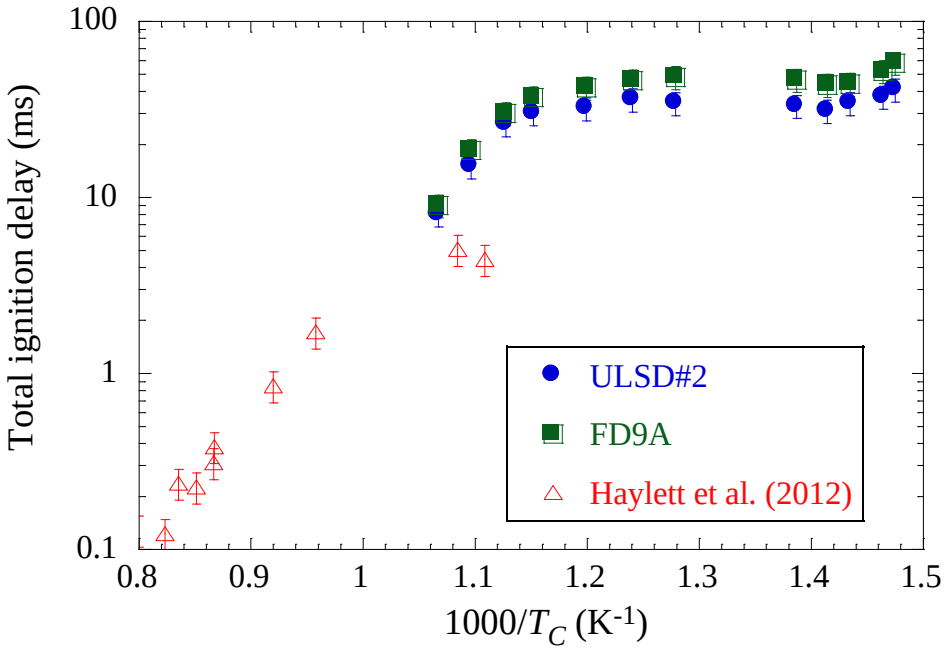

(a) P_C=10 bar, ϕ=0.5

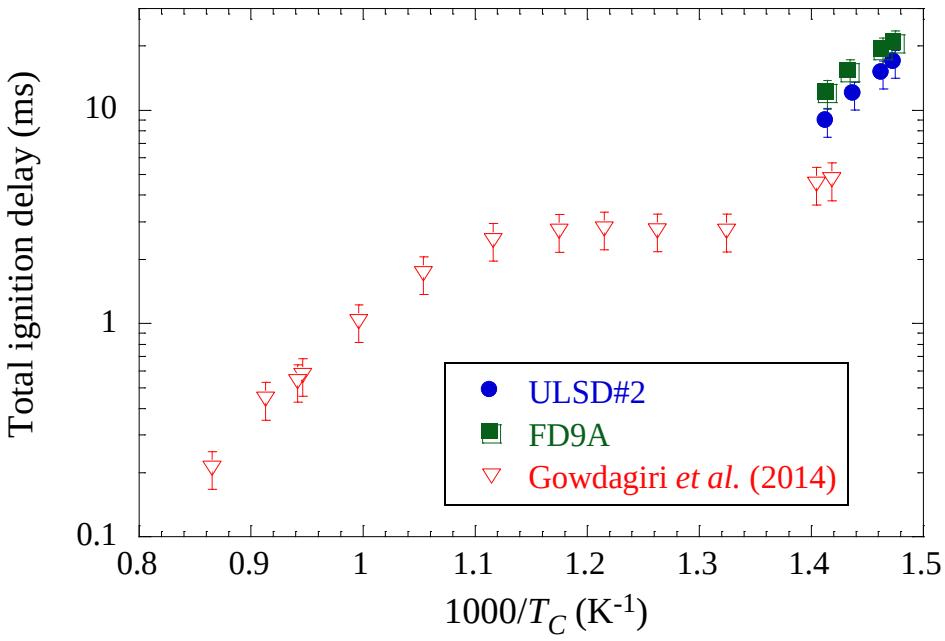

(b) P_C=20 bar, ϕ=0.5

Figure 6.8 Comparison of total ignition delays of ULSD#2, FD9A, and literature diesel blends at (a) P_C = 10 bar and ϕ = 0.5 and (b) P_C = 20 bar and ϕ = 0.5.

6.5 Conclusions

Using a heated RCM, autoignition experiments with two research grade diesel fuels, namely ULSD#2 and FD9A, have been conducted in the current study to investigate the effect of fuel composition on ignition propensity. The experimental results show that the differences in fuel composition could affect ignition propensities at temperatures where low temperature reactions are dominant. The current experiments also help in understanding the autoignition characteristics of diesel fuels, as well as proving validation database covering low-to-intermediate temperatures and elevated pressures for the formulation of diesel surrogates and the development of surrogate kinetic models. Experiments with changes in oxygen concentration, while keeping the fuel loading constant, show that both the first-stage and total ignition delays increase with decreasing oxygen concentration, with the total ignition delays being more sensitive to oxygen concentration variation than the first-stage ignition delays. To our knowledge, this work is the first time that the first-stage ignition delays of diesel fuels have been reported. Furthermore, the ignition delay measurements from the current RCM study were found to complement well with the existing shock tube data in the literature.

Chapter 7 : Summary and Future Directions

7.1 Summary

Ignition characteristics of tetralin was studied at varying pressures, temperatures, equivalence ratios and dilution. The experiments showed evidence of pre-ignition heat release at the low end of the temperature range investigated; however, no evidence of NTC behavior of the ignition delays was found. In addition, comparison of experimental and simulated ignition delays showed the available chemical kinetic model to be significantly less reactive than experiments. The kinetic analysis conducted suggests that comprehensive model describing the low temperature reactions is needed to generate a high fidelity chemical kinetic model to predict the ignition delays and pre-ignition heat release observed in the present experiments.

Autoignition of 1-MN has been studied at low-to-intermediate temperatures and elevated pressures. The experiments were conducted to demonstrate the effects of temperature, equivalence ratio, and pressure on ignition delays. The experiments showed that 1-MN behaves like a single-stage ignition fuel and no strong pre-ignition heat release was observed. In addition, the experimental ignition delays were used to assess the performance of two latest chemical kinetic models of 1-MN. The kinetic analysis conducted showed that the thermodynamic properties of the some of the intermediate species in one of the archived kinetic model of 1-MN need to be corrected. The other available model was found to predict ignition delays adequately and that the performance of the model could be improved further by inclusion of missing reaction pathways.

Auto-ignition of binary blends of *n*-dodecane/1-methylnaphthalene and *iso*-cetane/1-methylnaphthalene has been studied. The study illustrates the nonlinear response of the blend reactivity with respect to the relative amount of the constituent. For the blends with similar cetane ratings but different compositions, comparison of the measured ignition delays over a range of

compressed temperatures showed significant differences, thereby illustrating the inadequacy of using the cetane rating alone to capture the global blend reactivity. Since a comprehensive chemical kinetic model for the blends investigated here is under development, the current ignition delay datasets serve as the needed targets for model validation. For selected conditions, ignition delay simulations were conducted to highlight and discuss the deficiencies of the literature models and the potential areas for model improvements, especially at low temperatures.

Autoignition study of two well-characterized reference diesel fuels with similar cetane ratings but different compositional characteristics has been conducted. The two diesel blends used in the current study were a commercial grade ultra-low-sulfur diesel (ULSD) #2 reference fuel, ULSD#2, and a Fuels for Advanced Combustion Engines (FACE) research diesel, FD9A. The experimental results also showed that diesel blends with similar cetane ratings and different chemical compositional makeups exhibited varying ignition propensities in different temperature regimes, thereby demonstrating the effect of molecular composition on autoignition. In particular, the difference in ignition propensities was observed at temperatures at which the low temperature branching reactions are active. The ignition delay measurements from the current study provides additional experimental database of diesel blends needed for validation of diesel surrogate models.

7.2 Future Work

The work presented in the dissertation presents a systematic “bottom–up” approach with focus on the ignition of neat and binary mixtures of some of the components of diesel surrogates proposed by [9,10,23,43,60]. The future work could focus on ignition of diesel surrogate constituents which have not been studied widely in literature. Fundamental studies on ignition of such compounds which could provide ignition delay measurements along with the intermediate species profiles obtained from highly challenging gas sampling experiments are much desired. Some of the

candidate compounds of interest are *trans*-decalin, *n*-butylcyclohexane, large *n*-alkanes, etc., the constituents of diesel surrogates proposed by [9,10,23,43,60]. The study of [43] has also proposed four surrogate mixtures for diesel. Considering the lead time associated with development of chemical kinetic models of new molecules, it might be advised to test the surrogate mixtures proposed by [43] to see which surrogate of the four faithfully reproduces the ignition characteristics of the target diesel and then proceed accordingly.

References

1. J. E. Dec, Advanced compression-ignition engines—understanding the in-cylinder processes, Proc. Combust. Inst., 32 (2009), pp. 2727–2742
2. M. P. B. Musculus, P. C. Miles, and L. M. Pickett, Conceptual models for partially premixed low-temperature diesel combustion, Prog. Energy Combust. Sci., 39 (2013), pp. 246–283.
3. C. K. Westbrook, Chemical kinetics of hydrocarbon ignition in practical combustion systems, Proc. Combust. Inst., 28 (2000), pp. 1563–1577.
4. C. K. Westbrook, Y. Mizobuchi, T. J. Poinsot, P. J. Smith, and J. Warnatz, Computational combustion, Proc. Combust. Inst., 30 (2005), pp. 125–157.
5. M. Yao, Z. Zheng, and H. Liu, Progress and recent trends in homogeneous charge compression ignition (HCCI) engines, Prog. Energy Combust. Sci., 35 (2009), pp. 398–437.
6. FY 2012 Progress Report for advanced combustion engine research and development, DOE/EE-0872, Dec. 2012.
7. M. Mehl, J. Y. Chen, W. J. Pitz, S. M. Sarathy, and C. K. Westbrook, an approach for formulating surrogates for gasoline with application toward a reduced surrogate mechanism for cfd engine modeling, Energy & Fuels, 25 (2011), pp. 5215–5223.
8. S. Dooley, S. H. Won, J. Heyne, T. I. Farouk, Y. Ju, F. L. Dryer, K. Kumar, X. Hui, C.-J. Sung, H. Wang, M. A. Oehlschlaeger, V. Iyer, S. Iyer, T. a. Litzinger, R. J. Santoro, T. Malewicki, and K. Brezinsky, The experimental evaluation of a methodology for surrogate fuel formulation to emulate gas phase combustion kinetic phenomena, Combust. Flame, 159 (2012), pp. 1444–1466.

9. A. Krishnasamy, R. D. Reitz, W. Willems, and E. Kurtz, Surrogate diesel fuel models for low temperature combustion, SAE 2013-01-1092.
10. J. T. Farrell, N. P. Cernansky, F. L. Dryer, D. G. Friend, C. A. Hergart, C. K. Law, R. M. McDavid, C. J. Mueller, A. K. Patel, and H. Pitsch, development of an experimental database and kinetic models for surrogate diesel fuels, SAE International, 2007-01-0201, 2007.
11. C. J. Sung, H. J. Curran, Using rapid compression machines for chemical kinetics, Prog. Energy Combust. Sci., 44 (2014), pp. 1–18.
12. A. K. Das, Combustion characteristics of Moist H_2 and H_2/CO mixtures and in-situ temperature and species measurements using mid-IR absorption sprectoscopy in a new RCM, PHD Dissertation, 2012, Case Western Reserve Univeristy, Ohio
13. J. Würmel, J.M. Simmie, CFD studies of a twin-piston rapid compression machine, Combust. Flame, 141 (2005), pp. 417–430
14. G. Mittal, C. J. Sung, A rapid compression machine for chemical kinetics studies at elevated pressures and temperatures, Combust. Sci. Tech., 179 (2007), pp. 497–530.
15. B. W. Weber, K. Kumar, Y. Zhang, C. J. Sung, Autoignition of *n*-butanol at elevated pressure and low-to-intermediate temperature. Combust. Flame 158 (2011), pp. 809–819.
16. K. Kumar, G. Mittal, C. J. Sung, Autoignition of *n*-decane under elevated pressure and low-to-intermediate temperature conditions, Combust. Flame 156 (2009), pp. 1278–1288.
17. H. Hu, J. Keck, Autoignition of adiabatically compressed combustible gas mixtures, (1987) SAE Technical paper 872110.

18. M. Uddi, A.K. Das, C.J. Sung, Temperature measurements in a rapid compression machine using Mid-IR H_2O absorption spectroscopy near 7.6 μm, Appl. Opt., 51 (2012), pp. 5464–5476.
19. A.K. Das, M. Uddi, C.J. Sung, Two-line thermometry and H_2O measurement for reactive mixtures in rapid compression machine near 7.6 μm, Combust. Flame, 159 ((2012), pp. 3493–350.
20. G. Mittal, M. Chaos, C.J. Sung, F.L. Dryer, Dimethyl ether autoignition in a rapid compression machine: experiments and chemical kinetic modeling, Fuel Process Technol., 89 (2008), pp. 1244–1254.
21. CHEMKIN-PRO. San Diego: Reaction Design; 2013.
22. https://github.com/bryanwweber/pysens.
23. C. J. Mueller, W. J. Cannella, T. J. Bruno, B. Bunting, H. D. Dettman, J. A. Franz, M. L. Huber, M. Natarajan, W. J. Pitz, M. A. Ratcliff, K, Methodology for formulating diesel surrogate fuels with accurate compositional, ignition-quality, and volatility characteristics, Energy & Fuels, 26 (2012), pp. 3284–303.
24. Y .Yang, A. L. Boehman, Oxidation chemistry of cyclic hydrocarbons in a motored engine: Methylcyclopentane, tetralin, and decalin. Combust. Flame 157 (2010), pp. 495–505.
25. H. Wang, W. J. Gerken, W. Wang, M. A. Oehlschlaeger, Experimental study of the high-temperature autoignition of tetralin. Energy & Fuels, 27(2013), pp.5483–5487.
26. P. Dagaut P, A.Ristori, A. Frassoldati, T. Faravelli,G. Dayma, E. Ranzi. Experimental study of tetralin oxidation and kinetic modeling of its pyrolysis and oxidation, Energy & Fuels, 27 (2013), pp.1576–1585.

27. W. Tsang, J. P. Cui. Homogeneous gas-phase decyclization of tetralin and benzocyclobutene, J. Am. Chem. Soc., 112 (1990), pp.1665–1671.
28. J .Yu, S. Eser, thermal decomposition of jet fuel model compounds under near-critical and supercritical conditions. 2. decalin and tetralin, Ind. Eng. Chem. Res, 37 (1998), pp. 4601–4608.
29. J. Stewart, K. Brezinsky, I. Glassman, supercritical pyrolysis of decalin, tetralin,and *n*-decane at 700—800K product distribution and reaction mechanism, Combust. Sci. Technol., 136 (1998), pp. 373–390.
30. Y. Li, L. Zhang, Z. Wang, L. Ye, J. Cai, Z. Cheng, F. Qei, Experimental and kinetic modeling study of tetralin pyrolysis at low pressure, Proc. Combust. Inst., 34 (2013), pp. 1739–1748.
31. P. Zámostný, Z. Bělohlav, L. Starkbaumová, J. Patera, Experimental study of hydrocarbon structure effects on the composition of its pyrolysis products. J. Anal. Appl. Pyrolysis, 87 (2010), pp. 207–216.
32. B. W. Weber, C .J. Sung, M. W. Renfro. On the uncertainty of temperature estimation in a rapid compression machine, Combust. Flame, 162 (2015), pp. 2518–2528.
33. K. Kumar, C. J Sung, An experimental study of the autoignition characteristics of conventional jet fuel/oxidizer mixtures: Jet-A and JP-8, Combust. Flame, 157 (2010), pp. 676–685.
34. A. Roubaud, O. Lemaire, R. Minetti, L. R. Sochet. High pressure auto-ignition and oxidation mechanisms of *o*-xylene, *o*-ethyltoluene, and *n*-butylbenzene between 600 and 900 K, Combust. Flame, 123 (2000), pp. 561–571.

35. B. Husson, R. Bounaceur, K. Tanaka, M. Ferrari, O. Herbinet, P.A. Glaude, R. Fournet, F. Battin-Leclerc, M. Crochet, G. Vanhove, R. Minetti, C.J. Tobin, K. Yasunaga, J.M. Simmie, H.J. Curran, T. Niass, O. Mathieu, S.S. Ahmed . Experimental and modeling study of the oxidation of *n*-butylbenzene, Combust. Flame, 159 (2012), pp 1399–1416.

36. H. J. Curran, P. Gaffuri, W. J. Pitz, C. K. Westbrook, A comprehensive modeling study of *iso*-octane oxidation, Combust. Flame, 129 (2002), pp. 253-280.

37. H. J. Curran, P. Gaffuri, W. J. Pitz, C. K. Westbrook, A comprehensive modeling study of *n*-heptane oxidation, Combust. Flame, 114 (1998), pp. 149-177.

38. W. J. Pitz, C. V. Naik, T .N. Mhaoldúin, C. K. Westbrook, H. J. Curran,J. P. Orme, J. M. Simmie, Modeling and experimental investigation of methylcyclohexane ignition in a rapid compression machine. Proc. Combust. Inst., 31 (2007), pp.267–75.

39. E. J. Silke, W. J. Pitz, C. K. Westbrook, M. Ribaucour M. Detailed chemical kinetic modeling of cyclohexane oxidation. J. Phys. Chem. A., 111(2007), pp.3761–75.

40. M. Mehl, G. Vanhove, W. J. Pitz, E. Ranzi, Oxidation and combustion of the *n*-hexene isomers: a wide range kinetic modeling study, Combust. Flame, 155 (2008), pp.756-772

41. S. M. Sarathy, S. Vranckx, K. Yasunaga, M. Mehl, P. Oßwald, W. K. Metcalfe, C. K. Westbrook, W.J. Pitz, K. Kohse-Höinghaus, R. X. Fernandes, H. J. Curran, A comprehensive chemical kinetic combustion model for the four butanol isomers, Combust. Flame, 159 (2012), pp. 2028–55.

42. R. Gieleciak, C. Fairbridge, Detailed hydrocarbon analysis of FACE diesels using comprehensive two-dimensional gas chromatography. http://www.crcao.org/publications/advancedVehiclesFuelsLubricants/FACE/GCxGC%20analysis%20of%20FACE%20fuels%20-RG%20v4%200%20Nov2013.pdf.

43. C. J. Mueller, W. J. Cannella, T. Bays, T. J. Bruno, K. DeFabio, H. Dettman, R. Gieleciak, M. L. Huber, C-B Kweon, S. M. McConnell, W. J. Pitz, M. A. Ratcliff, Diesel surrogate fuels for engine testing and chemical-kinetic modeling: compositions and properties, Energy & Fuels, 30(2016), pp. 1445–1461.
44. C. B. Shaddix, K. Brezinsky, I. Glassman, Oxidation of 1-methylnaphthalene, Proc. Combust. Inst., 24 (1992), pp. 683–690.
45. C. B. Shaddix, K. Brezinsky, I. Glassman, Analysis of fuel decay routes in the high-temperature oxidation of 1-methylnaphthalene, Combust. Flame, 108 (1997), pp. 139–157.
46. K. Mati, A. Ristori, G. Pengloan, P. Dagaut, Oxidation of 1-methylnaphthalene at 1–13 atm: experimental study in a JSR and detailed chemical kinetic modeling, Combust. Sci. Tech., 179 (2007), pp. 1261-1285
47. U. Pfahl, K. Fieweger, G. Adomeit, Self-ignition of diesel-relevant hydrocarbon-air mixtures under engine conditions, Proc. Combust. Inst., 26(1996), pp. 781-789.
48. H. Wang, S. J. Warner, M. A. Oehlschlaeger, R. Bounaceur, J. Biet, P. A. Glaude, F. Battin-Leclerrc, An experimental and kinetic modeling study of the autoignition of α-methylnaphthalene/air and α-methylnaphthalene/n-decane/air mixtures at elevated pressures, Combust. Flame, 157 (2010), pp. 1976-1988.
49. R. Bounaceur, P. A. Glaude, R. Fournet, F. Battin-Leclerc, Kinetic modeling of a surrogate diesel fuel applied to 3D auotignition in HCCI engines, Int. J. Vehicle Des. 44 (2007), pp.124–142.
50. K. Narayanaswamy, G. Blanquart, H. Pitsch, A consistent chemical mechanism for the oxidation of substituted aromatic species, Combust. Flame, 157 (2010), pp. 1879-1898.

51. C. W. Zhou, V. V. Kislov, A. M. Mebel, Reaction mechanism of naphthyl radicals with molecular oxygen. 1. Theoretical study of the potential energy surface, J. Phys. Chem., 116 (2012), 1571-1585

52. T. Oguchi, Y. Murakami, Theoretical study on the kinetics and the mechanism for the gas-phase reaction of 1-naphtylmethyl radical with molecular oxygen, Chem. Phys. Letters, 585 (2013), pp. 27-32

53. http://rmg.mit.edu/

54. G. Blanquart, P. Pepiot-Desjardins, H. Pitsch, Chemical mechanism for high temperature combustion of engine relevant fuels with emphasis on soot precursors, Combust. Flame, 156 (2009), pp. 588-607.

55. C. A. Taatjes, D. L. Osborn, T. M. Selby, G. meloni, A. J. Trevitt, E. Epifanovsky, A. I. Krylov, B. Sirjean, E.Dames, H .Wang, Products of the benzene + O (^{3}P) reactions, J. Phys. Chem, 114 (2010), pp. 3355-3370

56. T. L. Nguyen, J. Peeters, L. J. Vereecken, Theoretical Reinvestigation of the O(3P) + C6H6 Reaction: Quantum Chemical and Statistical Rate Calculations, J. Phys. Chem, 111(2007), pp.3836-3849

57. T. Seta, M. Nakajima, A. Miyoshi, High temperature reactions of OH with benzene and toluene, J. Phys. Chem. A, 110 (2006), pp. 5081–5090

58. Y. Murakami, T. Oguchi, K. Hashimoto, Y. J. Nosaka, Theoretical study of the benzyl+o2 reaction: kinetics, mechanism and product branching ratios, J. Phys. Chem, 111 (2007), pp. 13201-13208.

59. G. da Silva, J. W. Bozzelli, Kinetic modeling of the benzyl +HO2 reaction, Proc. Combust. Inst., 32 (2009), pp. 287-294.

60. C. V. Naik, K. Puduppakkam, E. Meeks, Simulation and analysis of in-cylinder soot formation in a low temperature combustion diesel engine using a detailed reaction mechanism, 2013-01-1565, Apr. 2013., SAE Int. J. Engines, 6 (2013), pp. 1190–1201.
61. M. A. Oehlschlaeger, J. Steinberg, C. K. Westbrook, W. J. Pitz, The autoignition of iso-cetane at high to moderate temperatures and elevated pressures: shock tube experiments and kinetic modeling, Combust. Flame, 156 (2009), pp. 2165-2172.
62. S. H. Won, F. M. Haas, A. Tekawade, G. Kosiba, M. A. Oehlschaleger, S. Dooley, F. L. Dryer, Combustion characteristics of C_4 iso-alkane oligomers: experimental characterization of iso-dodecane as a jet fuel surrogate component, Combust. Flame, 165 (2016), pp. 137-143.
63. P. Dagaut., K. Hadj-Ali, Chemical kinetic study of the oxidation of *iso*-cetane in a jet stirred reactor: experimental and modeling, Energy Fuels, 23 (2009), pp. 2389-2395.
64. B. Li, H. Zhang, F. N. Egolfopoulos, Laminar flame propagation of atmospheric *iso*-cetane/air and decalin/air mixtures, Combust. Flame, 161 (2014), pp. 154-161.
65. S. S. Vasu, D. F. Davidson, Z. Hong, V. Vasudevan, R. K. Hanson, *n*-Dodecane oxidation at high-pressures, Measurement of ignition delay times and OH concentration time-histories, Proci. Combust. Inst., 32 (2009), pp. 173-180.
66. M. S. Kurman, R. H. Natelson, N. P. Cernansky, D. L. Miller, Speciation of the reaction intermediates from *n*-dodecane oxidation in the low temperature regime, Proci. Combust. Inst., 33 (2011), pp. 159-166.
67. A. Mze- Ahmed, K. Hadj-Ali, P. Dagaut, G. Dayma, Experimental and modeling study of the oxidation kinetics of *n*-undecane and *n*-dodecane in a jet-stirred reactor, Energy Fuels, 26 (2012), pp. 4253-4268.

68. H. S. Shen, J. Steinberg, J. Vanderover, M. A. Oehlschaleger, A shock tube study of the ignition of n-heptane, n-decane, n-dodecane, and n-tetradecane at elevated pressures, Energy & Fuels, 23 (2009), pp. 2482-2489.

69. X. Hui, C.J. Sung, Laminar flames speeds of transportation-relevant hydrocarbons and jet fuels at elevated temperatures and pressures, Fuel, 109 (2013), pp. 191–200.

70. C. Ji, E. Dames, Y. L. Wang, H. Wang, F. N. Egolfopoulos, Propagation and extinction of premixed C_5 to C_{12} *n*-alkane flames, Combust. Flame, 157 (2010), pp. 277–287.

71. K. Kumar, C. J. Sung, Laminar flame speeds and extinction limits of preheated *n*-decane/O_2/N_2 and *n*-dodecane/O_2/N_2 mixtures, Combust. Flame, 151 (2007), pp. 209–224.

72. T. Malewicki, K. Brezinsky, Experimental and modeling study on the pyrolysis and oxidation of *n*-decane and *n*-dodecane, Proc. Combust. Inst., 34 (2013), pp. 361–368.

73. D.F. Davidson, D.R. Haylett, R. K. Hanson, Development of an aerosol shock tube for kinetic studies of low-vapor-pressure fuels, Combust. Flame, 155 (2008), pp. 108–117.

74. D. F. Davidson, Z. Hong, G. L. Pilla, A. Farooq, R. D. Cook, R. K. Hanson, Multi-species time history measurements during *n*-dodecane oxidation behind reflected shock waves, Proc. Combust. Inst., 33 (2011), pp. 151–157.

75. S. H. Won, S. Dooley, P. S. Veloo, H. Wang, M. A. Oehlschlaeger, F. L. Dryer, Y. Ju, The combustion properties of 2,6,10 trimethyldodecane, a chemical function group analysis, Combust. Flame, 161 (2014), pp. 826-834.

76. A. Agosta, N. P. Cernansky, D. L. Miller, T. Faravelli, E. Ranzi, Reference components of jet fuels: kinetic modeling and experimental results, Exp. Therm. Fluid Sci., 28 (2004), pp. 701–708.

77. J. Yanowitz, M. A. Ratcliff, R. L. McCormick, J. D. Taylor, Compendium of experimental cetane numbers, http://www.nrel.gov/docs/fy14osti/61693.pdf.

78. S. M. Sarathy, C. K. Westbrook, M. Mehl, W. J. Pitz, C. Togbe, P. Dagaut, H. Wang, M. A. Oehlschlaeger, U. Niemann, K. Seshadri, P. S. Veloo, C. Ji, F. N. Egolfopoulos, T. Lu, Comprehensive chemical kinetic modeling of the oxidation of 2-methylalkanes from C_7 to C_{20}, Combust. Flame, 158 (2011), pp. 2338-2357.

79. G. Kukkadapu, C. J. Sung, Autoignition study of ULSD#2 and FD9A diesel blends, Combust. Flame, 166 (2016), pp. 45-54.

80. K. Narayanaswamy, P. Pepiot, H. Pitsch, A chemical mechanism for low to high temperature oxidation of *n*-dodecane as a component of transportation fuel surrogates, Combust. Flame, 161 (2014), pp. 866-884.

81. J. Bugler, B. Marks, O. Mathieu, R. Archuleta, A. Camou, C. Grégoire, K. A. Heufer, E. L. Petersen, H. J. Curran, An ignition delay time and chemical kinetic modeling study of the pentane isomers, Combust. Flame, 163 (2016), pp. 138-156.

82. K. Zhang, C. Banyon, C. Togb, P. Dagaut, J. Bugler, H. J. Curran, An experimental and kinetic modeling study of *n*-hexane oxidation, Combust. Flame, 162 (2015), pp. 4194-4207.

83. S. Y. Mohamed, L. Cai, F. Khaled, C. Banyon, Z. Wang, M. J. Al Rashidi, H. Pitsch, H. J. Curran, A. Farooq, S. M. Sarathy, Modeling ignition of a heptane isomer: improved thermodynamics, reaction pathways, kinetics, and rate rule optimizations for 2-methylhexane, J. Phys. Chem. A, 120 (2016), pp. 2201–2217.

84. ASTM D613-15, Standard test method for cetane number of diesel fuel oil, ASTM International, West Conshohocken, PA, 2015.

85. ASTM D6890-15, Standard test method for determination of ignition delay and derived cetane number (DCN) of diesel fuel oils by combustion in a constant volume chamber, ASTM International, West Conshohocken, PA, 2015.
86. G. E. Bogin Jr., E. Osecky, M. A. Ratcliff, J. Luecke, X. He, B. T. Zigler, A. M. Dean, Ignition quality tester (IQT) investigation of the negative temperature coefficient region of alkane autoignition, Energy &Fuels 27 (2013), pp. 1632-1642.
87. L. J. Spadaccini, J. A. Tevelde, Autoignition characteristics of aircraft-type fuels, Combust. Flame, 46 (1982), pp. 283–300.
88. O. G. Penyazkov, K. L. Sevruk, V. Tangirala, N. Joshi, Autoignitions of diesel fuel/air mixtures behind reflected shock waves, Proceedings of the 4th European combustion meeting, Vienna, Austria; 2009.
89. A. J. Dean, O. G. Penyazkov, K. L. Sevruk, B. Varatharajan, Autoginition of surrogate fuels at elevated temperatures and pressures, Proc. Combust. Inst., 31 (2007), pp. 2481-2488.
90. D. R. Haylett, D. F. Davidson, R. K. Hanson, Ignition delay times of low-vapor pressure fuels measured using an aerosol shock tube, Combust. Flame, 159 (2012), pp. 552–61.
91. S. Gowdagiri, W. Wang, M. A. Oehlschlaeger, A shock tube ignition delays study of conventional diesel fuel and hydroprocessed renewable diesel fuel from algal oil, Fuel 128 (2014), pp. 21-29.
92. M. Alnajjar, W. Cannella, H. Dettman, C. Fairbridge, J. Franz, T. Gallant, R. Gieleciak, D. Hager, C. Lay, S. Lewis, M. Ratcliff, S. Sluder, J. Storey, H. Yin, B. Zigler, Chemical and physical properties of the Fuels for Advanced Combustion Engines (FACE) research diesel fuels, FACE-1; Coordinating Research Council: Alpharetta, GA, 2010.

93. W. Cannella, C. Fairbridge, R. Gieleciak, P. Arboleda, T. Bays, H. Dettman, M. Foster, G. Gunter, D. Hager, D. King, C. Lay, S. Lewis, J. Luecke, S. Sluder, B. Zigler, B. Natarajan, Advanced alternative and renewable diesel fuels: detailed characterization of physical and chemical properties, Coordinating Research Council: Alpharetta, GA, 2013.
94. C. L. Yaws, Yaw's Handbook of Thermodynamic and Physical Properties of Chemical Compounds, 2003, Knovel.
95. M. E. MacDonald, W. Ren, Y. Zhu, D. F. Davidson, R. K. Hanson, Fuel and ethylene measurements during n-dodecane, methylcyclohexane, and *iso*-cetane pyrolysis in shock tubes, Fuel 103 (2013), pp.1060-1068.
96. G. Kukkadapu, K. Kumar, C. J. Sung, M. Mehl, W. J. Pitz, Experimental and surrogate modeling study of gasoline ignition in a rapid compression machine, Combust. Flame, 159 (2012), pp. 3066-3078.
97. G. Kukkadapu, K. Kumar, C. J. Sung, M. Mehl, W. J. Pitz, Autoignition of gasoline and its surrogates in a rapid compression machine, Proci. Combust. Inst., 34 (2013), pp.345-352.
98. S. M. Sarathy, G. Kukkadapu, M. Mehl, W. Wang, T. Javed, S. Park, M. A. Oehlschlaeger, A. Farooq, W. J. Pitz, C. J. Sung, Ignition of alkane–rich FACE gasoline fuels and their surrogate mixtures, Proci. Combust. Inst., 35 (2015), pp. 249–257.
99. G. Kukkadapu, K. Kumar, C. J. Sung, M. Mehl, W. J. Pitz, Autoignition of gasoline surrogates at low temperature combustion conditions, Combust Flame, 162 (2015), pp. 2272-2285
100. K. Kumar, C. J. Sung, A comparative experimental study of the autoignition characteristics of alternative and conventional jet fuel/oxidizer mixtures, Fuel 89 (2010), pp. 2853-2863.